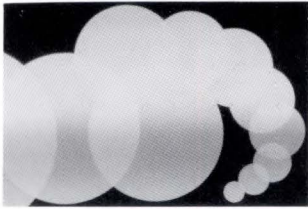


FUJITSU SCIENTIFIC & TECHNICAL JOURNAL

Autumn 1988 VOL.24, NO.3





This Issue's Cover

Various elements are being researched to develop faster and higher density integrated circuits. Among these elements are the super lattice elements obtained by repeatedly stacking extremely thin films of various semiconductor compounds. These elements have a shorter electron driving time than existing transistors. Because of this, it is expected that the future ultrahigh speed elements will be manufactured using super lattice element technology.

FUJITSU Scientific & Technical Journal is published quarterly by FUJITSU LIMITED of Japan to report the results of research conducted by FUJITSU LIMITED, FUJITSU LABORATORIES LTD., and their associated companies in communications, electronics and related fields. It is the publisher's intent that FSTJ serve to promote the international exchange of such information, and we encourage the distribution of FSTJ on an exchange basis. All correspondence concerning the exchange of periodicals should be addressed to the editor.

FSTJ can be purchased through KINOKUNIYA COMPANY LTD., 3-17-7 Shinjuku, Shinjuku-ku, Tokyo 160-91, (Telex No. 2424344, answerback KINOKUNI J).

The price is US \$5.00 per copy, excluding postage.

FUJITSU LIMITED reserves all rights concerning the republication and publication after translation into other languages of articles appearing herein.

Permission to publish these articles may be obtained by contacting the editor.

FUJITSU LIMITED

Takuma Yamamoto, *President*

FUJITSU LABORATORIES LTD.

Masaka Ogi, *President*

Editorial Board

Editor Hiroshi Yamada

Associate Editor Takahiko Misugi

Editorial Representatives

Koichi Dazai	Toshito Hara	Masao Hiyane
Noriaki Fujimura	Kazuhiisa Kobayashi	Yoshihiro Kosaka
Ken-ichi Murata	Seiya Ogawa	Shinji Ohkawa
Eisaku Ohshima	Shigeru Sato	Tohru Sato
Shozo Taguchi	Hideo Takahashi	Hirobumi Takanashi
Mitsuhiko Toda	Ryoiku Toge	Toru Tsuda
Akira Yoshida		

Editorial Coordinator

Kazuo Yono

FUJITSU LIMITED 1015 Kamikodanaka, Nakahara-ku,
Kawasaki 211, Japan

Cable Address: FUJITSULIMITED KAWASAKI

Telephone: +81-44-777-1111

Telex: 3842122, 3842221, 3842802, 3842803,

Answerback FTWKAW J

Printed by MIZUNO PRITECH Co., Ltd. in Japan

© 1988 FUJITSU LIMITED (September 14, 1988)

FUJITSU SCIENTIFIC & TECHNICAL JOURNAL

Autumn 1988 VOL.24, NO.3

CONTENTS

- 177 **Analysis of Kanji Structures and a Method for Recognizing On-Line Handwritten Kanji Characters by Means of Stroke Representative Points**
● Yasuo Ishii
- 203 **Cooperative Expert System Applied to Simulation of Human Group Behavior**
● Nobuo Watanabe ● Takashi Kimoto
- 212 **ISDN Subscriber Loop Transmission LSI Using Echo Cancelling Method**
● Toshitaka Tsuda ● Misao Fukuda ● Yutaka Awata
- 225 **Interference from Digital QAM System to Analog FM System**
● Yoshimasa Daido ● Hiroshi Nakamura
- 235 **High Quality Toner Image Transfer in Electrophotographic Printing**
● Masashi Ogasawara ● Masatoshi Kimura
- 242 **Liquid Phase Epitaxial Growth of Fe-Doped Semi-Insulating InP, GaInAsP, and AlGaInAs**
● Toshiyuki Tanahashi ● Makoto Kondo ● Mitsuru Sugawara
- 254 **Fe-50%Co Sintered Alloy for Magnetic Circuit Yoke**
● Wataru Yamagishi ● Tsutomu Iikawa

UDC 003.324.25:681.327.12

FUJITSU Sci. Tech. J., **24**, 3, pp. 177-202(1988)

Analysis of Kanji Structures and a Method for Recognizing On-Line Handwritten Kanji Characters by Means of Stroke Representative Points

• Yasuo Ishii

This paper shows how structural information with a 99.99 percent stability rate can be extracted from handwritten kanji characters.

It also shows how kanji patterns can be resolved stably. A new on-line kanji character recognition method achieved a success ratio of 99.5 percent in recognizing kanji characters written in an unspecified style.

UDC 678.84:77.021.6

FUJITSU Sci. Tech. J., **24**, 3, pp. 235-241(1988)

High Quality Toner Image Transfer in Electrophotographic Printing

• Masashi Ogasawara • Masatoshi Kimura

This paper presents a newly developed transfer method for electrophotographic printers. This method uses a medium such as silicone rubber to which a toner image is first transferred by pressure and from which the image is then retransferred and fixed onto paper by pressure and heat. The resulting image resolution of 1 000 dots per inch is due to less toner scatter. This method is suitable for in-house printing and desktop publishing applications.

UDC 001.81:681.32

FUJITSU Sci. Tech. J., **24**, 3, pp. 203-211(1988)

Cooperative Expert System Applied to Simulation of Human Group Behavior

• Nobuo Watanabe • Takashi Kimoto

This paper describes a model for a cooperative expert system which simulates human group behavior. When social phenomena are observed, Fujitsu has realized that experts usually act autonomously. But there are also many cases when experts must work in close cooperation. The major design goal of this study is to construct a framework to naturally represent cooperation among expert systems. Since expert systems interact only via conversation, an expert system cannot access or change another expert's knowledge base without the owner's permission. This system can also process non-deterministic tasks by parallel inference.

UDC 548.524:621.315.592

FUJITSU Sci. Tech. J., **24**, 3, pp. 242-253(1988)

Liquid Phase Epitaxial Growth of Fe-Doped Semi-Insulating InP, GaInAsP, and AlGaInAs

• Toshiyuki Tanahashi • Makoto Kondo • Mitsuru Sugawara

Fe-doped InP, $Ga_xIn_{1-x}As_yP_{1-y}$, and $Al_uGa_vIn_{1-u-v}As$ grown by liquid phase epitaxy have been extensively studied. The temperature, composition, and material dependences of Fe doping characteristics of these materials are well explained by three factors: the Fe solubility in the growth solution, the background electron concentration, and the Fe distribution coefficient. The high resistivities of 8×10^7 ohm-cm, 2×10^5 ohm-cm, and 1×10^9 ohm-cm have been obtained for InP grown at 900 °C, $Ga_{0.26}In_{0.74}As_{0.57}P_{0.43}$ and $Al_{0.48}In_{0.52}As$ grown at 750 °C, respectively.

The activation energies of the Fe acceptor levels in $Ga_xIn_{1-x}As_yP_{1-y}$ and $Al_uGa_vIn_{1-u-v}As$ systems have been also studied. It is found that the Fe acceptor level is aligned at a constant energy relative to the vacuum level.

UDC 621.3.049.771.14:621.395.721.1

FUJITSU Sci. Tech. J., **24**, 3, pp. 212-224(1988)

ISDN Subscriber Loop Transmission LSI Using Echo Cancelling Method

• Toshitaka Tsuda • Misao Fukuda • Yutaka Awata

This paper describes a 144 kbit/s digital subscriber loop (DSL) transmission system based on hybrid-mode transmission with an echo cancelling method. It uses advanced LSI technology to obtain compactness, low cost, and high reliability. An echo canceller (EC) LSI has been developed using CMOS technology. Combined with the multiplexing processor (MXP) LSI, the EC LSI provides basic DSL equipment functions. The system consists of a specially arranged frame format with a newly developed DPLL circuit for stable timing extraction, and automatic balancing next-work, and a two-stage echo canceller.

Using this line termination circuit, the DSL equipment showed a reach of over 6 km when used with 0.5 mm diameter cable for 160 kbit/s bidirectional digital transmission.

UDC 621.318.13:621.762.5

FUJITSU Sci. Tech. J., **24**, 3, pp. 254-261(1988)

Fe-50%Co Sintered Alloy for Magnetic Circuit Yoke

• Wataru Yamagishi • Tsutomu Iikawa

To produce a soft magnetic Fe-50%Co alloy using powder metallurgy, a study was made on the effects of various starting powders on the sintered density and magnetic properties of this alloy. An Fe-50%Co sintered alloy with a relative density of 95 percent and a magnetization of 2.15 T in a magnetic field of 4 kA/m was obtained using pre-alloyed Fe-20%Co and -400 mesh pure Co powders as the starting powders. This sintered alloy was used in a 24-wire-dot matrix printer. This printer operated at a printing speed of 110 cps (for Japanese character "kanji" printing) due to the higher magnetization afforded by the Fe-50%Co sintered alloy.

UDC 621.391.822:621.396.61.037.3

FUJITSU Sci. Tech. J., **24**, 3, pp. 225-234(1988)

Interference from Digital QAM System to Analog FM System

• Yoshimasa Daido • Hiroshi Nakamura

Considering high-power transmission of high-capacity digital radio system such as a 256 QAM, this paper describes a method for determining the conditions under which a new digital system can be installed without disturbing the already existing analog FM systems.

The ratio of the FM signal to interference level is calculated as a function of the channel separation between the FM and the digital systems, using various parameters such as bit rate, rolloff factor, and modulation level of the digital system. This paper also shows that spectrum shaping of the QAM system by cosine rolloff filter results in a more rapid decrease in the interference level for increase of the channel separation than that of the conventional PSK system using a 5-section Butterworth filter with BT of 1.2 as a transmit filter.

Analysis of Kanji Structures and a Method for Recognizing On-Line Handwritten Kanji Characters by Means of Stroke Representative Points

• Yasuo Ishii

(Manuscript received February 27, 1987)

This paper shows how structural information with a 99.99 percent stability rate can be extracted from handwritten kanji characters.

It also shows how kanji patterns can be resolved stably. A new on-line kanji character recognition method achieved a success ratio of 99.5 percent in recognizing kanji characters written in an unspecified style.

1. Introduction

The recognition of handwritten kanji characters is the focus of character recognition research in Japan.

The number of kanji categories to be recognized is very much larger than the number of alphabetic categories.

For example, the Japanese Industrial Standards (JIS) Committee has created a standard set of kanji characters¹⁾. This set contains 6349 categories which are divided into two levels. The 2965 JIS level-1 characters form the basic set. The remaining 3384 kanji characters are termed JIS level-2 characters.

The great number of kanji categories in wide use is one of the difficulties of kanji character recognition. Generally speaking, the structure of kanji is quite complex. A complex kanji character is a combination of several basic patterns. Replacing one of the several basic patterns with another makes another kanji character. For example, replacing a part of the kanji character 漢 turns it into the kanji character 嘆.

The above example shows that not only are the structures of kanji characters complex, but also some kanji characters closely resemble

each other. This is the second reason why kanji character recognition is difficult. In the case of handwritten kanji character recognition, individual handwriting styles show significant differences in the patterns. This is the third reason why recognition is difficult.

Character recognition methods are classified as on-line character recognition and off-line character recognition. The former is usually easier to implement. For kanji character recognition, better results have been reported for on-line recognition than for off-line recognition.

For example, in on-line handwritten kanji character recognition in which both the stroke order and the number of strokes are correct, results with a recognition ratio of 99.7 percent were achieved by Odaka et al., in 1980, using mixed texts of kana and kanji characters^{2),3)}.

Results were also reported for the case of unrestricted stroke order by Odaka et al.⁴⁾ in 1982; for the case of unrestricted stroke order and number of strokes by Wakahara and Odaka⁵⁾ in 1983; and for the case of cursive characters by Sato and Ichihara⁶⁾ in 1983, and by Wakahara and Umeda⁷⁾ in 1984.

As shown by these achievements, restrictions on the stroke order and number of strokes for

on-line handwritten kanji character recognition have been lifted. However, this was only achieved by registering in a dictionary as many different patterns as required for different writers, and by using a dynamic programming matching method to match the dictionary to the input pattern. As a result, both the dictionary size and matching time are increased.

We chose to examine what would happen if kanji character patterns contained stable information that is only dependent on the pattern shape, regardless of differences among writers.

If stable information can be extracted, then the use of it could free kanji character recognition from stroke order restrictions. In addition, the dictionary size would decrease and the time taken to match the dictionary and input pattern could also be cut down.

This paper describes the analysis of kanji structures using this approach and the results obtained from recognition experiments.

Chapter 2 of this paper describes the matrix representation of kanji structures and the experimental way in which information was obtained about stable kanji characters. Chapter 3 describes the methods used to resolve kanji structures. Chapter 4 describes kanji recognition experiments based on the methods used to resolve kanji structures.

2. Structure of kanji characters and matrix representation of characters

2.1 Structure of kanji characters

The basic element of a kanji character is the stroke.

The two simplest kanji characters ("ichi", meaning "one", and "otsu", meaning "the second or the latter") and the most complex kanji character ("noh", meaning "a stopped nose") were selected from a medium-sized Chinese-Japanese dictionary⁸⁾ and are shown in Fig. 1.

If a kanji character contains more than two strokes, its structure can be represented by all the positional relations of all its pairs of strokes.

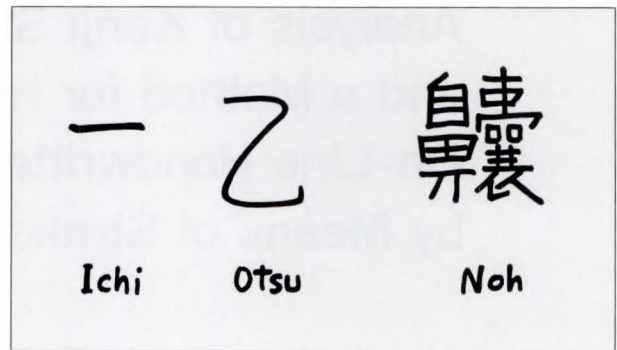


Fig. 1—Simplest kanji characters and a complex kanji character.

The strokes of a kanji character are numbered to correspond to their correct stroke order. Assume that the positional relation of the i -th stroke (S_i) and the j -th stroke (S_j) is G_{ij} (the exact definition of G_{ij} will be given later). We call the matrix representation of the structure of this kanji character, $\{G_{ij}\}$, its structure matrix.

Now, let us define G_{ij} , that is, the positional relation between strokes S_i and S_j . Kato et al.⁹⁾ defined one point for each stroke, and called it the representative point of the stroke. It is not easy to precisely define the positional relations of strokes. However, the positional relations between representative points can be easily defined. For this reason, Kato et al. devised and used the latter instead of the former. Although representation varies somewhat in this paper, the essential theory of definitions follows that of Kato et al.

Assume that the representative points of the two strokes S_i and S_j are D_i and D_j , respectively, and their coordinates are (X_i, Y_i) and (X_j, Y_j) .

In this paper, four representative points were considered for strokes; namely, the Beginning Point (B), Ending Point (E), Midpoint (M), and the Center of Gravity (G). However, the discussion presented below is independent of the type of representative point used.

The relative positional relations G_{ij} between the representative points D_i and D_j is represented as a two-digit value. The first digit

represents the left-to-right relation, while the second digit represents the top-to-bottom relation.

Assume the value of the first digit of G_{ij} to be L if D_i is not located to the right of D_j , that is, if $X_i \leq X_j$; and assume the value of the first digit of G_{ij} to be R if D_i is located to the right of D_j , that is, if $X_i > X_j$.

Assume the value of the second digit of G_{ij} to be U if D_i is not located below D_j , that is, if $Y_i \geq Y_j$; and assume the value of the second digit of G_{ij} to be D if D_i is located below D_j , that is, if $Y_i < Y_j$.

Summarizing the foregoing, if $i \neq j$

$$G_{ij} = LU | LD | RU | RD, \quad \dots \dots (1)$$

where, if $i = j$

$$G_{ij} = **.$$

The difference between kanji categories is not considered in the above notation. To distinguish between categories, the symbol representing the category is added to the right shoulder. For example, the i -th stroke of category k is S_i^k , and its representative point is D_i^k .

2.2 Stability of structure matrix

Kato et al.⁹⁾ stated that the relative positional relation between the representative points of the strokes is stable. Therefore, we will make structure matrices $\{G_{ij}\}$ for many handwritten patterns to check their stability.

2.2.1 Definition of stability

Select a pattern from an arbitrary category k , and observe the relative positional relation G_{ij} between its two strokes S_i and S_j , and the value of its first digit is either L or R based on the definition.

For m patterns selected from category k , assume the number of patterns for which the value of the first digit of G_{ij} was L to be l , and the number of patterns for which the value of the first digit of G_{ij} was R , to be r . Then, of course, $l + r = m$.

We define the horizontal stability of S_i and S_j as follows:

$$X(k, i, j) = |l - r| / m, \quad \dots \dots (2)$$

it is obvious that

$$0 \leq X \leq 1.$$

If $X = 1$, then $l = m$ or $r = m$, which means that the value of the first digit of G_{ij} are L or

Table 1. A 200 kanji categories in common use, taken from the beginning of the JIS level-1 code

垂	哀	愛	惡	握	庄	扱	綾	安	暗	案	以	伊	位	依	偉	圉	委	威	尉
意	慰	易	為	異	移	維	緯	胃	違	遺	医	井	交	域	育	郁	磯	一	壹
逸	稻	芋	印	員	因	姻	引	飲	胤	院	陰	隱	韻	右	宇	羽	雨	卯	丑
渦	浦	運	雲	營	影	映	榮	永	泳	英	衛	詠	銳	液	疫	益	馱	悅	謁
越	閱	円	園	宴	延	援	沿	演	炎	煙	猿	緣	艷	遠	鉛	塩	汚	凹	央
奧	往	応	押	横	欧	殴	王	黄	冲	億	屋	億	乙	卸	恩	温	隱	音	下
化	仮	何	価	佳	加	可	嘉	夏	嫁	家	寡	科	暇	果	架	歌	河	火	禍
稼	箇	花	荷	華	菓	課	貨	過	蚊	我	画	芽	賀	雅	餓	介	会	解	回
塊	壞	快	怪	悔	懷	戒	拐	改	械	海	灰	界	皆	繪	開	階	貝	効	外
害	慨	概	涯	街	該	馨	垣	各	括	格	核	殼	獲	確	穫	覺	角	較	郭

Table 2. All the ten-stroke kanji categories in common use (203 categories)

案	員	院	浦	益	悦	宴	恩	夏	家	荷	華	蚊	皆	害	格	核	株	陷	既
婦	記	起	飢	鬼	宮	拳	恐	恭	胸	脅	桐	桑	訓	郡	惠	桂	儉	兼	劍
軒	原	個	庫	娛	悟	候	晃	校	浩	耕	航	貢	降	高	剛	骨	根	唆	差
座	宰	裁	劑	財	索	桜	殺	棧	蚕	殘	師	紙	脂	時	疾	射	借	酌	弱
殊	珠	酒	修	從	准	殉	純	書	徐	除	宵	將	消	症	祥	稱	笑	辱	唇
娠	振	晉	浸	真	針	陣	粹	衰	逝	隻	席	扇	栓	租	素	倉	搜	插	造
息	速	孫	帶	泰	託	值	恥	致	畜	逐	秩	通	庭	悌	遜	哲	展	徒	途
倒	党	凍	唐	島	桃	討	透	胴	匿	特	惱	納	能	破	馬	俳	配	倍	梅
班	畔	般	疲	秘	被	姬	倭	病	浜	敏	瓶	浮	粉	紛	勉	捕	倣	俸	峰
砲	剖	紡	埋	脈	眠	娘	耗	紋	容	浴	流	留	竜	旅	料	倫	淚	烈	恋
連	朗	浪																	

R , respectively. Further, if $X = 0$, then $l = r$, which means that half of the values of the first digit of G_{ij} are L and the remainder are R .

Similarly, let us define the vertical stability direction of S_i and S_j as follows:

$$Y(k, i, j) = |u - d| / m, \dots \dots \dots (3)$$

where u is the number of patterns for which the value of the second digit of G_{ij} is U , and d is the number of patterns for which the value of the second digit of G_{ij} is D .

Then, obviously,

$$u + d = m, \dots \dots \dots (4)$$

and

$$0 \leq Y \leq 1. \dots \dots \dots (5)$$

2.2.2 Pattern collections for stability experiments

On-line handwritten printed-style kanji patterns are collected. It must be possible to compare kanji patterns which belong to the same category easily and positively. To ensure this, only patterns with the correct number of strokes and the correct stroke order were adopted. To maintain consistency in

the experimental data, all categories were written by a specific group of writers. Forty writers in their twenties and early thirties were selected, including four women.

Experimental patterns must be in a small set which is representative of all kanji characters. For this purpose, two unique sets were used. The categories contained in each of these sets are shown in Tables 1 and 2.

Each of these sets contains kanji categories that contain kanji characters for personal names and common kanji characters. Table 1 shows the first 200 categories as arranged in the order of the JIS level-1 codes, while Table 2 shows 203 categories of kanji characters with ten strokes.

Table 1 features kanji characters with different numbers of strokes. Table 2 features a maximum of kanji characters having the same number of strokes.

A data collector as shown in Fig. 2 was used to obtain the required stroke patterns. This device consists of a tablet for recording on-line handwritten patterns, connected to a FACOM FM-8 personal computer.

- 1) Data was collected as follows: "A guide to writing kanji patterns (with their stroke order)" was shown to all persons taking part in the experiment (see Fig. 3).
- 2) The following request was made: "Please

write the kanji patterns with the correct number of strokes and using the correct stroke order. Please rewrite if you make a mistake."

- 3) When data collection was complete, all patterns were reproduced using a data check system, and the data collected from the

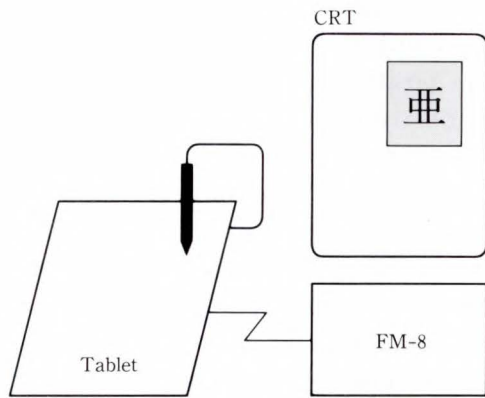


Fig. 2—Kanji pattern collector.

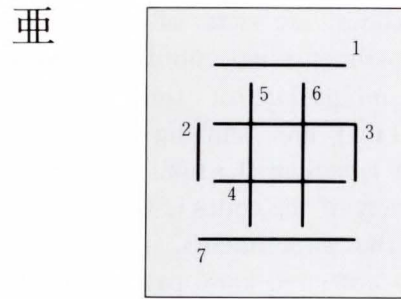


Fig. 3—Sample of a guide to write kanji patterns.



Fig. 4—Sample of collected kanji patterns.

forty writers were checked visually.

- 4) Whenever an incorrect character was detected, it was rewritten by its original writer.

The shapes of some of the collected patterns are shown in Fig. 4.

The individual pattern data consists of the kanji character code, writer number (0 through 39), and stroke codes arranged in stroke order. Stroke codes are sets of point coordinates on a two-dimensional coordinate system based on a combination of time sampling (once every 20 ms) and shifting distance sampling (shifts of less than 0.3 mm were ignored), and the accuracy of the codes is 16 bits.

For the experiments, the strokes of the originally collected kanji patterns were reedited into sets of several points of equal intervals.

Forty patterns were collected for each category, all of which were printed-style kanji

characters, handwritten on-line patterns with the correct number of strokes and in the correct writing order for use as experimental data.

A total of 403 categories (200 categories in the first set and 203 in the second set) were collected, or 16 120 patterns in all.

2.2.3 Stability experiment

Experiments were made on the stability of the positional relations of representative points of strokes, using the patterns written by 40 writers on the 200 categories of kanji characters shown in Table 1 (200 × 40 = 8 000 patterns).

Two of the 200 categories were excluded because they contain only kanji characters of one stroke, and the remaining 198 categories were considered. If two arbitrary strokes are considered as a pair of strokes within the character group, then a total of 10 412 pairs can be made.

Table 3. Frequency distribution table showing positional stabilities of each representative point

Stability (A)	Beginning point (B)		Ending point (E)		Midpoint (M)		Center of gravity (G)	
	x	y	x	y	x	y	x	y
0	61	30	42	43	62	29	43	31
0.05	117	60	94	124	123	78	104	49
0.10	112	66	102	105	109	79	97	68
0.15	108	61	83	110	107	54	88	52
0.20	118	82	98	122	119	73	108	64
0.25	126	79	88	117	106	68	96	62
0.30	128	82	94	93	114	61	116	68
0.35	123	84	106	128	139	74	97	75
0.40	124	91	97	107	127	72	122	63
0.45	145	92	113	129	108	75	127	67
0.50	152	101	102	129	107	97	121	93
0.55	150	85	108	130	97	92	102	90
0.60	158	121	116	121	116	103	127	87
0.65	173	93	114	127	119	117	139	112
0.70	173	116	120	136	110	97	147	124
0.75	180	148	172	130	138	124	160	127
0.80	190	180	196	164	153	162	201	157
0.85	255	192	215	172	223	169	233	171
0.90	320	252	350	281	280	237	313	246
0.95	481	374	553	426	487	380	494	400
1.00	7 018	8 023	7 449	7 518	7 468	8 171	7 377	8 206
Total	10 412	10 412	10 412	10 412	10 412	10 412	10 412	10 412
Mean	0.868 1	0.914 5	0.895 1	0.883 3	0.883 1	0.919 6	0.887 6	0.924 8

Since 40 patterns are prepared for every category, 40 relative positional relations can be observed for each pair and stability can be calculated for the pair.

The Beginning point (**B**), Ending point (**E**), Midpoint (**M**), and the center of Gravity (**G**) were selected as representative points for the strokes. For each type of point the following experiment was carried out: The horizontal stability (X) and vertical stability (Y) were calculated for 10 412 sets of strokes, and the frequency distribution for every 0.05 was obtained for the stability range from 0 to 1. Results are shown in Table 3.

Table 3 shows the overall stability of the relative positional relations between representative points. The mean stability is between 0.87 and 0.92 and, therefore, can be said to be stable as a whole. However, the relative positional relations with stability of 1.00 (that is, those virtually without individual differences) were only 67.4 percent to 78.8 percent. Therefore, the positional relations are significantly affected by individual differences, which seems to prevent their use as stable structural information.

Kato et al. avoided this problem by registering individual information, but this is not a desirable solution. Therefore, we will examine possible causes of instability of the positional relations between strokes to determine whether

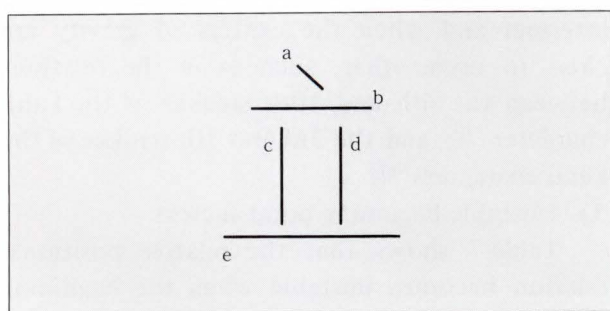


Fig. 5—Kanji pattern 立.

note: Henceforth, we will refer to the representative points by capital letters, as follows. (**B**): beginning point, (**E**): ending point, (**M**): midpoint, and (**G**): the center of gravity.

instability is caused by differences among writers or is due to the method used for observing the structural information.

2.2.3 Review of the experiment

Table 3 shows that neither the horizontal stability nor the vertical stability is stable enough.

However, let us examine Fig. 5. The top-to-bottom relations between strokes a and b, b and c, b and d, c and e, and d and e are all stable.

In addition, the left-to-right relation between c and d is stable. This means that these types of relations are not apt to be affected by individual differences. However, the left-to-right relation between a and b and the top-to-bottom relation between c and d may be significantly affected by individual differences.

Therefore, we simply select either the

Table 4. Frequency distribution table showing positional stability A of each representative point

A	B	E	M	G
0	0	0	1	0
0.05	0	0	3	0
0.10	0	3	1	0
0.15	0	1	1	0
0.20	0	2	0	0
0.25	0	9	4	0
0.30	0	5	1	4
0.35	2	13	2	4
0.40	3	14	4	1
0.45	6	11	7	3
0.50	9	14	3	9
0.55	12	15	5	8
0.60	17	27	7	6
0.65	26	11	4	11
0.70	21	16	7	8
0.75	33	19	6	13
0.80	42	28	8	7
0.85	55	23	20	12
0.90	70	78	27	22
0.95	116	155	55	61
1.00	10 000	9 968	10 246	10 243
Total	10 412	10 412	10 412	10 412
Mean	0.992 7	0.990 3	0.996 3	0.996 5

horizontal stability (X) or vertical stability (Y) – whichever is better – and define this to be the stability of the two strokes.

That is, assuming the stability of the two strokes S_i^k and S_j^k to be $A(k, i, j)$,

$$A(k, i, j) = \max \{ X(k, i, j), Y(k, i, j) \} . \dots\dots\dots (6)$$

Using this new definition, the frequency distribution of positional stability (A) for the same data shown in Table 3 is calculated as shown in Table 4.

The average of stabilities of the A distribution is more than 0.99, and the percentage of those with a stability of 1.00 is 98.41 percent for **M**, 98.38 percent for **G**, 96.04 percent for **B**, and 95.74 percent for **E**, respectively.

Although stabilities vary according to the type of representative point, it is apparent that the percentage of those with a stability of 1.00 has been improved significantly and that structural information is more stable than that shown in Table 3.

To be more specific:

Stable observation can be performed by merely observing X if the relative positional relation between the i -th stroke and the j -th stroke of a given kanji structure seems intuitively to be in the left-to-right relation, and by merely observing Y if the relative positional relation between the i -th stroke and the j -th stroke of a given kanji structure seems intuitively to be in the top-to-bottom relation.

In this way, by limiting the direction of observation for each set of kanji strokes to either left-to-right or top-to-bottom, and through more stable observation, the observed stability of G_{ij}^k is increased.

Therefore, the instability of the relative positional relations between the representative points shown in Table 3 is due to the method used to observe the information, rather than due to individual differences.

From Table 4, however, it is obvious that none of the representative points is sufficiently stable and that the stability varies for different

types of representative points.

Next, we will extract cases having lower stability and analyze them for each representative point.

2.2.4 Analysis of cases with low stability

For each of the four types of representative points, ten A 's (k, i, j) were output in ascending order of stability. This was done to determine which stroke pairs in which categories have low stability in the positional relation.

The actual characters contained in category k and the shapes of combinations of S_i^k and S_j^k were checked and shown in Tables 5 through 8.

For example, if we select the characters having low Midpoint stability from Table 4, there are ten characters ranging from $A = 0$ to $A = 0.25$.

The details of these ten low stabilities are shown in Table 5.

In Table 4, similarly, the ten low stabilities of **G** are distributed from $A = 0.30$ to $A = 0.45$, in ascending order, and their details are as shown in Table 6. These are the same for both **B** and **E**.

The following conclusions can be drawn from checking Tables 5 through 8:

- 1) Unstable midpoint factors
Table 5 shows that relative positional relations become unstable when the two strokes intersect and when the midpoints are close to each other.
- 2) Unstable center of gravity factors
From Table 6, the relative positional relations become unstable when the two strokes intersect and when the centers of gravity are close to each other, such as in the relations between the 6th and 10th strokes of the kanji character 馬 and the 3rd and 7th strokes of the kanji characters 雨 .
- 3) Unstable beginning point factors
Table 7 shows that the relative positional relation becomes unstable when the beginning points of the two strokes are close to each other.
- 4) Unstable ending point factors

Table 8 shows that the relative positional relation becomes unstable when the ending points of the two strokes are close to each other.

Therefore, regardless of the type of the

Table 5. Unstable portions in the case of the midpoint

A of M	Unstable character	Unstable pairs of strokes		
		Pattern	Stroke number	
			i	j
0	園	+	3	4
0.05	馨	+	1	2
0.05	殼	+	1	2
0.05	解	+	5	6
0.10	運	+	7	9
0.15	綾	+	7	8
0.20	壞	+	4	5
0.25	塊	+	7	8
0.25	街	+	4	5
0.25	箇	+	9	10

Table 6. Unstable portions in the case of the center of gravity

A of G	Unstable character	Unstable pairs of strokes		
		Pattern	Stroke number	
			i	j
0.30	毆	メ	2	3
0.30	駅	冂	6	10
0.30	悔	+	8	9
0.30	越	+	1	2
0.35	嘉	+	1	2
0.35	奧	+	6	7
0.35	佳	+	3	4
0.35	佳	+	6	7
0.40	涯	十	6	7
0.45	雨	冂	3	7

Table 7. Unstable portions in the case of the beginning point

A of B	Unstable character	Unstable pairs of strokes		
		Pattern	Stroke number	
			i	j
0.35	悔	冂	6	7
0.35	穫	冂	10	12
0.40	映	冂	1	2
0.40	街	冂	2	4
0.40	郁	冂	3	4
0.45	影	冂	1	2
0.45	確	冂	9	11
0.45	磯	冂	11	17
0.45	凹	冂	1	2
0.45	閱	冂	1	2

Table 8. Unstable portions in the case of the ending point

A of E	Unstable character	Unstable pairs of strokes		
		Pattern	Stroke number	
			i	j
0.10	皆	冂	8	10
0.10	回	冂	4	5
0.10	遣	冂	2	3
0.15	貝	冂	2	5
0.20	磯	冂	4	5
0.20	馨	冂	18	20
0.25	垂	冂	3	4
0.25	緯	冂	11	12
0.25	駅	冂	11	12
0.25	箇	冂	12	13

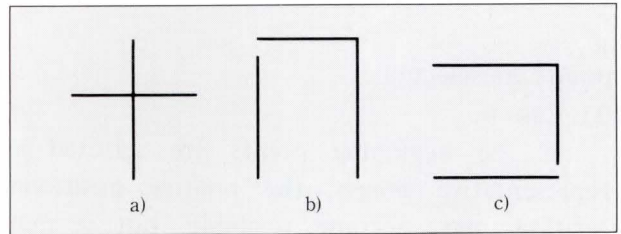


Fig. 6—Sample patterns having representative points which are near to each other.

representative point, the positional relation between the representative points becomes unstable when the specific representative points are close to each other in the kanji structure.

It is reasonable to conclude that when points are essentially close to each other, regardless of the writer of the kanji character, the relative positional relation between those points becomes unstable.

This fact indicates the measures to be taken to obtain structural information that is more stable than that shown in Table 4. This topic will be discussed in the next subsection.

2.2.5 Dynamic selection of representative points

Structures such as those shown in Fig. 6 often appear in kanji characters.

1) Case a:

If the midpoints or the centers of gravity are selected as the representative points, positional relations may become unstable, but they may become stable if the beginning points or ending

Table 9. Frequency distribution of the best stability using two kinds of representative points

A_{max}	B and E	B and M	B and G	E and M	E and G	M and G
0.45	1					1
0.50		1	1	1	1	3
0.55						5
0.60	1					2
0.65						5
0.70						5
0.75						7
0.80						5
0.85						9
0.90	5			5	3	16
0.95	11	6	6	6	13	41
1.00	10 394	10 405	10 405	10 400	10 395	10 313
Total	10 412	10 412	10 412	10 412	10 412	10 412
Mean	0.999 8	0.999 9	0.999 9	0.999 9	0.999 9	0.998 5

points are selected.

2) Case b:

If the beginning points are selected as representative points, the relative positional relation may become unstable, but it may become stable if other representative points are selected.

3) Case c:

If the ending points are selected as representative points, the positional relation may become unstable, but it may become stable if other representative points are selected.

Which representative points should be selected for the two arbitrary strokes S_i and S_j ? If the strokes are as shown in case a) of Fig. 6, neither **M** nor **G** should be selected as the representative point. If the strokes are as shown in case b), **B** should not be selected. If they are as shown in case c), the ending points should not be selected.

To see how much stability can be maintained by making this selection, the stabilities of G_{ij}^k for the two types of representative points P and Q are defined respectively as follows:

$$A_P = \{ A(k, i, j) \text{ for } P \}, \dots (7)$$

$$A_Q = \{ A(k, i, j) \text{ for } Q \}. \dots (8)$$

Then, the following is obtained:

$$A_{max} = \max(A_P, A_Q). \dots (9)$$

The frequency distributions of A_{max} are

Table 10. Frequency distribution of the best stability using three kinds of representative points and the instable cases

A_{max}	Frequency	Unstable cases
0.50	1	磯 (11, 17)
0.55		
0.60		
0.65		
0.70		
0.75		
0.80		
0.85		
0.90		
0.95	2	液 (8, 9) 稼 (12, 13)
1.00	10 409	
Total	10 412	
Mean	0.999 9	

shown in Table 9. Table 9 is equal to the distribution of the stability of G_{ij}^k where the more desirable representative points of the two types were specified for each set of S_i^k and S_j^k . Table 9 shows that **M** and **G** behave similarly.

Now, let us increase to three the types of representative points to be observed, and consider cases where the most desirable representative points are always selected from among the three types. However, since **M** and **G** have similar behavior, only **M** will be used. Therefore, only the types of representative points that give the best stabilities of G_{ij}^k need be

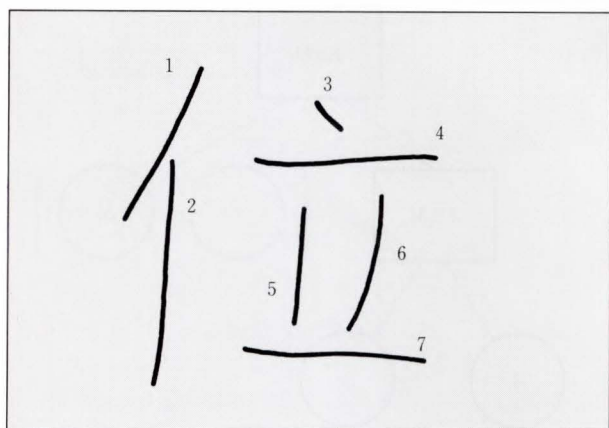


Fig. 7—Kanji pattern 亻.

selected from among the beginning points, midpoints or ending points.

This can be expressed as follows:

$$A_{\max} = \max(A_B, A_M, A_E). \quad \dots \quad (10)$$

This is shown in Table 10.

From this result, if the most desirable representative points are selected from these three types on a case-by-case basis to check the stabilities, it can be verified that the mean stability is 0.999 9.

In this way, it has been shown that if the category of the kanji character and the two strokes contained therein are specified and a dictionary is prepared specifying the type of the representative points and the direction to be observed (that is, the left-to-right or the top-to-bottom direction, whichever is stable) as the positional relation between the representative points, even handwritten kanji characters have very stable structural information, except in special cases. In fact, of the 10 412 sets of kanji patterns used in this paper, 10 409 sets show a stability of 1.00, and two sets (the 8th and 9th strokes of 液 and the 12th and 13th strokes of 稼) show a stability of 0.95. The remaining sets were the 11th and 17th strokes of 磯, which shows that the position of the 17th stroke (a dot) fluctuates significantly, depending on the writer.

2.2.6 Summary

The foregoing is summarized as follows:

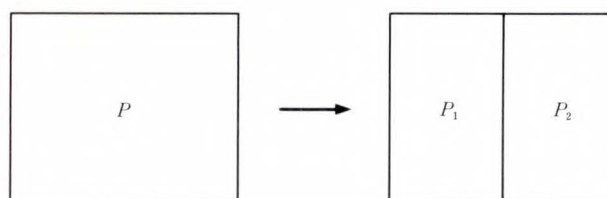


Fig. 8—Pattern divisible into left and right.

When we have determined the kanji category and the two strokes S_i and S_j that are to be observed, a mean stability of 0.999 9 for the values of G_{ij}^k can be observed by specifying the following:

- 1) The type of representative point to be observed, and
- 2) The direction of observation (top-to-bottom or left-to-right).

Since there is a 99.99 percent stability in the values found for G_{ij}^k , by observing information inherent to the kanji characters alone, the structure matrix G_{ij}^k , in which the i -th and j -th elements are selected according to points 1) and 2) above, also contain sufficiently stable information.

3. Resolution of kanji structure

3.1 Examples

Even a complex kanji pattern often consists of divisible sets of simple patterns. For example, the kanji character 亻 shown in Fig. 7 is a composite of pattern 亻 (the left-side radical meaning “man”) and pattern 亻. As shown in Fig. 8, the kanji pattern P can be divided into two patterns P_1 and P_2 for simpler representation.

Another example is the kanji character 花 which is a composite of pattern 艹 (“grass”) and pattern 匕, and can be divided from top to bottom as shown in Fig. 9.

Let us pursue this analysis further. 亻 can be divided from top to bottom, and 亻 can be divided from top to bottom to obtain 亻 and 亻.

Continuing with this process, a kanji structure can be resolved into individual strokes.

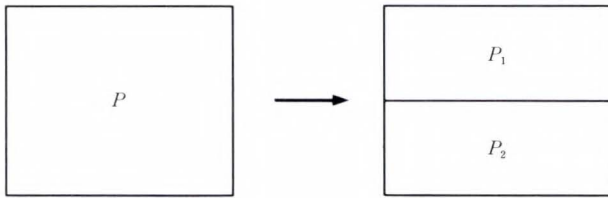


Fig. 9—Pattern divisible into top and bottom.

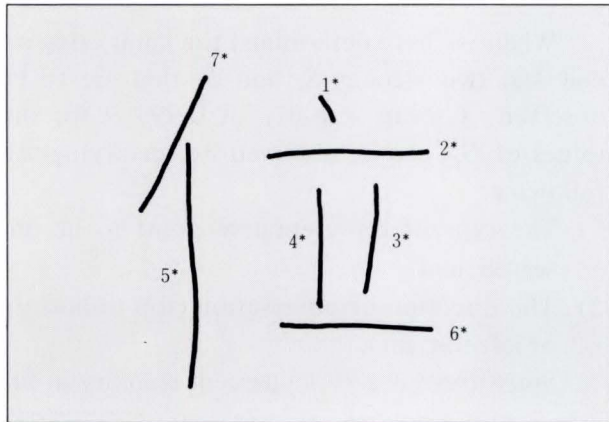


Fig. 10—Kanji pattern 立 writing in irregular order.

For example, the kanji character 立 can be resolved into seven components. These strokes are numbered from 1 to 7 for identification, as shown in Fig. 7. Each of these numbers is called the dictionary stroke order. The stroke i in dictionary stroke order is S_i . The order of actual writing of each stroke (different from the dictionary stroke order) is as shown in Fig. 10.

Assume that only the actual writing order is known. Now let us consider how we can find whether the stroke whose actual writing order is x_7 , for example, is equal to 1 in the dictionary stroke order.

It is known that the midpoints of strokes 1 and 2 in the dictionary stroke order of this kanji pattern are stably located to the left of the midpoints of strokes 3 through 7. Therefore, after the midpoints of each stroke of an actual written pattern are obtained, and the two midpoints on the left are selected, then the stroke corresponding to the two midpoints will be the two strokes whose stroke orders are x_7 and x_5

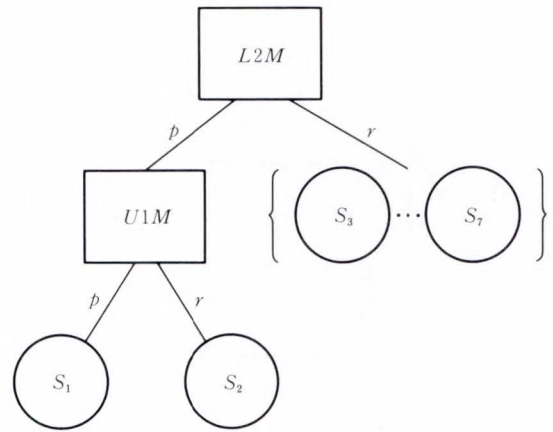


Fig. 11—Partial tree structure representation of the kanji character 立.

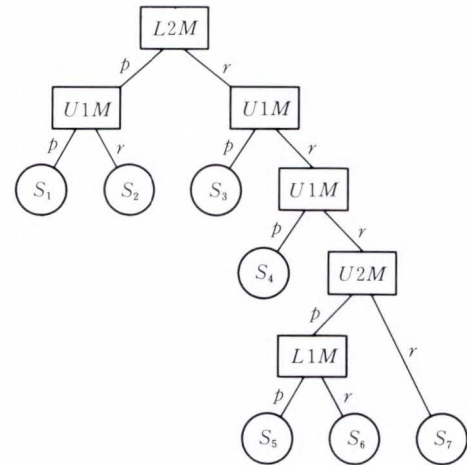


Fig. 12—Tree structure representation of the kanji character 立.

(that is, strokes 1 and 2 in the dictionary stroke order).

Next, if, of the two strokes, the stroke whose M is on top is selected, it should correspond to the stroke whose writing order is x_7 (stroke 1 in the dictionary stroke order). These processes are represented as shown in Fig. 11.

$L2$ means that two midpoints are to be taken from the left side. p indicates the set of the selected strokes, while r indicates the sets of remaining strokes. For the two selected strokes, $U1$ means that one M is to be taken from the top. The selected stroke is S_1 , and the remaining stroke is S_2 .

For S_3 through S_7 , similarly, by repeating

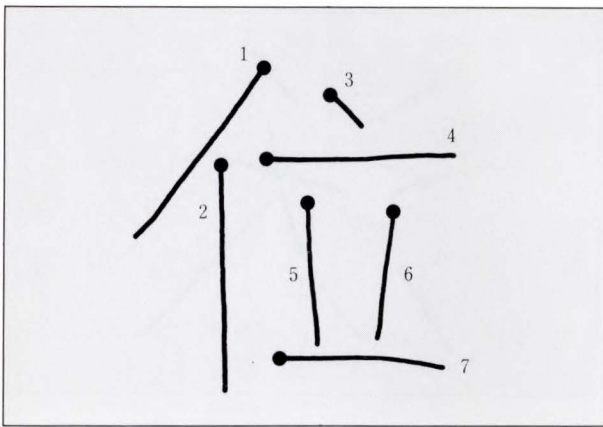


Fig. 13—Kanji pattern 位 representing beginning points of strokes.

access to the patterns from the top or bottom or from the left or right and by observing the midpoints, the dictionary stroke order can be learned, even if the actual writing order is different from the dictionary stroke order.

An example of this method is shown in Fig. 12.

3.2 Possibility of structure resolution

Now, let us examine further whether kanji patterns can be resolved in practice.

The stable positional relation of the two strokes ensures that at least either the top-to-bottom relation or the left-to-right relation of the representative points of the two strokes is stable.

Now, let us consider strokes 1 and 4, shown in Fig. 13. Here, the black dots of the pattern shown in Fig. 13 represent the beginning points of strokes. Since the top-to-bottom relation between the beginning points of strokes 1 and 4 is stable, it can be said that the relative positional relation between strokes 1 and 4 is stable. However, it is obvious that the left-to-right relation between the beginning points of strokes 1 and 4 is not stable. Therefore, if two beginning points are to be taken from the left side, strokes 1 and 2 are not always selected. That is, strokes 2 and 4 could possibly be selected.

In other words, high stability of the relative positional relation between strokes does not always guarantee arbitrary resolution of the

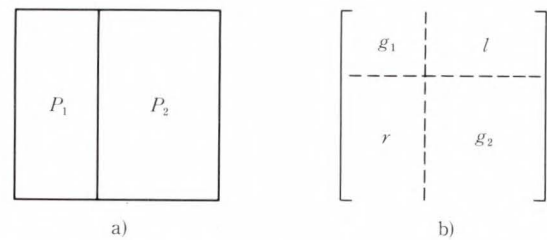


Fig. 14—Vertically divisible pattern and its structure matrix.

kanji pattern.

Therefore, an experiment is necessary to ascertain the possibility of resolving the kanji pattern. For this reason, we describe below the algorithm for determining the possibility of resolution by viewing the structure matrix of a kanji pattern.

In Fig. 14, patterns P_1 and P_2 are patterns that are arranged from left to right. Assume that these two patterns make up a character (calling its pattern P).

As shown in Fig. 14-b), the structure matrix of P consists of four matrices. That is, the two square matrices g_1 and g_2 , which correspond to the structure matrices of patterns P_1 and P_2 , respectively, and the two matrices names l and r .

Matrix l is a matrix such that all its elements contain value L , while matrix r is a matrix such that all its elements contain value R . Matrices l and r indicate that P_1 is located to the left of P_2 .

If it is known that the arbitrary structure matrix g consists of matrices l and r and two square matrices g_1 and g_2 as shown in Fig. 14, it is clear that pattern P , whose structure matrix is g , can be resolved into two patterns, P_1 and P_2 , whose structure matrices are g_1 and g_2 , respectively. It is also apparent that P_1 is located to the left of P_2 .

Similarly, assume u to be a matrix, all elements of which contain value U , and also assume d to be a matrix, all elements of which contain value D . In this case, if it is known that the arbitrary structure matrix consists of matrix u , matrix d , and two square matrices g_1 and g_2 as shown in Fig. 15, it is obvious that pattern P whose structure matrix is g , can

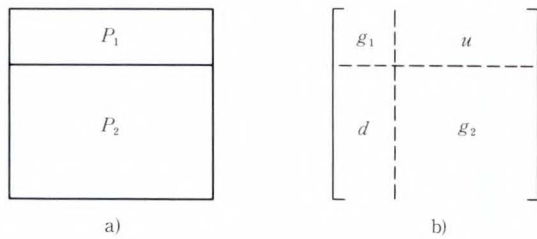


Fig. 15—Horizontally divisible pattern and its structure matrix.

be resolved into two patterns, P_1 and P_2 , that are in top-to-bottom relation.

From the foregoing study, whether an arbitrary pattern can be resolved into patterns in the top-to-bottom relation or left-to-right relation depends on whether the upper right matrix corresponds to either matrix l or matrix u , after the square matrix at the upper left and the square matrix at the lower right of the structure matrix g of the pattern have been determined as shown in Figs. 14 or 15. (If the upper right is matrix l , the lower left is always matrix r , and if the upper right is matrix u , the lower left is always d , and vice versa.)

Whether pattern P can be resolved can be determined by checking the matrix at the upper right while gradually increasing the size of the square matrix at the upper left starting at a value of one.

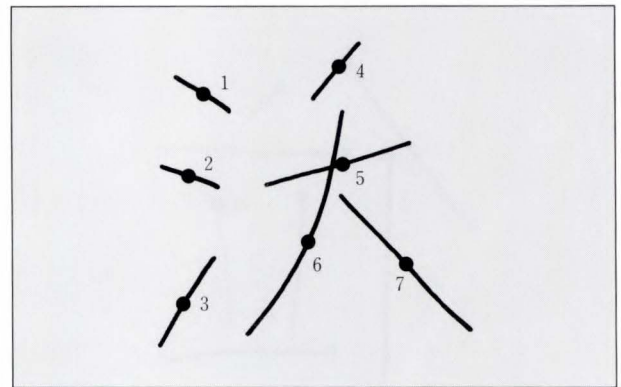
Let us see how this applies to a specific example, using the structure matrix (matrix g) shown in Fig. 16. By examining this matrix we can determine whether the original pattern can be resolved. Taking the size of g_1 as 1 at first, since the matrix at the upper right (matrix h) is

$$h = (RU \ RU \ LD \ LU \ LU \ LU),$$

it is apparent that it is neither the l type nor u type. Then, by increasing the size of g_1 to 2, the matrix at the upper right (h) becomes

$$h = \begin{bmatrix} RU & LD & LU & LU & LU \\ RU & LD & LD & LU & LU \end{bmatrix}. \quad \dots (12)$$

This matrix is neither l type not u type. Next, increasing the size of g_1 to 3, matrix h is



$$\begin{bmatrix} ** & RU & RU & LD & LU & LU & LU \\ LD & ** & RU & LD & LD & LU & LU \\ LD & LD & ** & LD & LD & LD & LD \\ RU & RU & RU & ** & LU & RU & LU \\ RD & RU & RU & RD & ** & RU & LU \\ RD & RD & RU & LD & LD & ** & LU \\ RD & RD & RU & RD & RD & RD & ** \end{bmatrix}$$

Fig. 16—Kanji pattern 沃 and its structure matrix.

$$h = \begin{bmatrix} LD & LU & LU & LU \\ LD & LD & LU & LU \\ LD & LD & LD & LD \end{bmatrix}, \quad \dots (13)$$

this is obviously an l -type matrix because all of its elements contain value L . The matrix at the lower left is of course r type. At this time, g_1 is as follows:

$$g_1 = \begin{bmatrix} ** & RU & RU \\ LD & ** & RU \\ LD & LD & ** \end{bmatrix}. \quad \dots (14)$$

The remaining square matrix g_2 is as follows:

$$g_2 = \begin{bmatrix} ** & LU & RU & LU \\ RD & ** & RU & LU \\ LD & LD & ** & LU \\ RD & RD & RD & ** \end{bmatrix}. \quad \dots (15)$$

Therefore, it is obvious that structure matrix g consists of two square matrices, g_1 and g_2 , and an l type matrix and an r type matrix, as shown in Fig. 14. Hence, the original pattern corresponding to g can be resolved into patterns in the left-to-right relation, in which case the left pattern has three strokes and its structure matrix is equal to g_1 , while the right pattern has four strokes and its structure matrix is equal to g_2 .

This result was induced mechanically, based only on structure matrix information. However, this result is very similar to the result of intuitive human judgement concerning the kanji pattern shown in Fig. 16.

The foregoing describes the algorithm that determines whether the original pattern can be resolved by viewing structure matrices that correspond to individual kanji patterns.

What if one category is found to contain many different hand-written patterns? If there should be, for example, 40 different patterns, we will create a new, integrated structure matrix that can be used to represent all 40.

First of all, taking each element in order, the individual elements of all 40 matrices are compared with each other. If an element in any particular place in the matrix —For the sake of explanation, let us use the 5th element in the series as an example.— is found to have the same value in all 40 matrices, then that value will be used for the (5th) element when creating the integrated structure matrix. If for some of the pattern matrices, this (5th) element is found to have a different value from the value it has in the others, the portion of its value that does not match will be represented in the new integrated structure matrix as “?”. The new integrated structure matrix created in this way is called the structure matrix of the category and represents the structure matrices of all 40 patterns. The probability of resolution of the representative patterns of the category can be determined by applying the above algorithm to the category structure matrix.

3.3 Experimenting with structure resolution

When a structure matrix is given, it can be mechanically determined whether its original pattern can be resolved into patterns in the left-to-right relation or in the top-to-bottom relation. This is also true for the structure matrix representing the category. Therefore, let us carry out experiments on the probability of resolution of many categories. If a pattern has a significant fluctuation and therefore any element of the structure matrix representing the category has the value “?”, the category can

not be perfectly resolved.

3.3.1 Overview of experiments

Experiments were carried out on each representative point, **B**, **E**, **M**, and **G** for 198 categories out of the 200 character categories shown in Table 1 (excluding two categories that have only one stroke). That is, experiments on the probability of resolution of the category structure matrices were carried out in the following sequence, using patterns written by 40 writers:

- 1) Simple resolution of a category structure matrix with only one type of representative point.
- 2) Using two of the category structure matrices, each one with a different type of representative point. An experimental resolution is carried out on one type of representative point, and if the pattern cannot be resolved any further, then resolution is carried out on an other type of representative point, and so on.
- 3) Resolution is carried as far as possible in the same way as item 2) above, with three types of representative points.

Due to the similarity of **M** and **G**, we did not use all four types and representative points in carrying out experiments on the category structure matrices.

3.3.2 Probability of resolution of a structure using a single representative point

A simple analysis was made of a category structure matrix (Let us simply call it a “structure matrix”, when no confusion is expected.) with a single type of representative point. That is, the given structure matrix was resolved into partial structure matrices. Next, an attempt was made to further resolve each partial structure matrix until it became indivisible. Then the number of these indivisible partial structure matrices was counted.

Assume the number of indivisible partial structure matrices of d -dimension to be $Z(d)$. Since the partial structure matrices of l -dimension cannot be resolved any further, $Z(l)$ indicates the number of strokes that can be resolved in the given category.

Table 11. Value distribution of $Z(d)$ in the case of simple resolution of kanji structure

d	$Z(d)$			
	B	E	M	G
1	947	593	1 346	1 537
2	192	51	83	87
3	36	23	37	40
4	24	22	5	6
5	17	8	8	7
6	7	14	4	6
7	8	9	9	3
8	11	11	5	0
9	2	4	3	1
10	2	7	2	0
11	0	7	1	0
12	3	14	2	1
13	2	10	2	2
14	3	8	1	0
15	2	10	3	0
16	2	3	1	1
17	0	1	1	0
18	0	1	0	0
19	0	3	0	0
20	0	0	0	0

Table 11 shows the results of simple resolution of the characters in the 198 categories used in this experiment. The sum of the strokes contained in these characters is 2010. Assuming the maximum value of d , where the value of $Z(d) \neq 0$, to be d_{max} , the following expression holds:

$$\sum_{d=1}^{d_{max}} d \times Z(d) = 2010.$$

As shown in Table 11, the value of d_{max} is 16, if the representative point is a **B**; 17, if the representative point is a **M**; and 19, if the representative point is an **E**.

Also, assuming the percentage of patterns { out of the total numbers of strokes (2010) } that can be resolved into structures consisting of only one stroke to be q , then

$$q = Z(1)/2010.$$

This is regarded as the probability of resolution.

Table 11, shows that considering the probability of resolution for all representative points, the value q obtained in the case of the center of gravity is the largest. Even in this case,

Table 12. Probability of resolution of structure matrix

Number of representative points used for resolution	q
One kind	0.76
Two kinds	0.95
Three kinds	0.987

however, the value, as shown in Table 12, is approximately 0.76, indicating that the use of a single representative point is not sufficient to determine the reconfiguration of the stroke order.

3.3.3 Probability of resolution of a structure using two types of representative points

Two types of representative points were selected, and the category structure matrix for one of them was resolved as far as possible. When it became indivisible, the matrix for the other was then resolved further. Lastly, only the structure matrices that could not be resolved using both representative points were counted.

Results are shown in Table 13. Confirmation was also made as to which of the representative points should be taken first—the one which achieved a better result, or the one which achieved an inferior result in Table 11. It was found better to resolve the structure matrix using as far as possible the type of representative point that achieved a better result, and after that, using another representative point.

However, combinations of the centers of gravity and ending points are considered better than those too — similar centers of gravity and midpoints. Combinations of the centers of gravity and beginning points do best, which appears to indicate that it is better to select representative points that can supplement each other.

The probability of resolution (q) is 0.95 in the best case (where the resolution was carried out first with the **G**, and then with the **B**), which represents a significant improvement over the use of a single type of representative point.

Table 13. Value distribution of $Z(d)$ when using two kinds of representative points

d	B and E	M and B	G and B	M and E	G and E	G and M
1	1 651	1 846	1 913	1 706	1 838	1 700
2	34	12	12	10	14	77
3	7	5	2	3	7	14
4	10	1	2	0	2	1
5	1	4	2	5	4	3
6	5	3	4	4	3	3
7	3	1	0	4	2	2
8	1	0	0	4	0	0
9	1	1	0	2	1	1
10	1	0	0	1	0	0
11	1	1	0	2	0	0
12	3	1	1	1	1	1
13	2	1	1	1	2	2
14	2	0	0	2	0	0
15	2	1	0	2	0	0
16	1	1	0	1	1	1
17	0	0	0	1	0	0
18	0	0	0	0	0	0

3.3.4 Resolution using three types of representative points

Three types of category structure matrices were used. Resolution was first performed using one of the three types of representative points, then another type, and finally the third type. Table 14 shows the results of resolution.

Six experiments were performed on combinations of the **B**, **E**, and **G**, and six more experiments were performed on combinations of the **B**, **E**, and **M**. The distribution of the sizes of the structure matrices that could not be resolved did not depend on the sequence in which the resolution was carried out. Therefore, only the types of combinations and their results are shown.

Since the **G** and the **M** are similar, experiments on combinations of the two were omitted.

As can be seen from Table 14, the probability of resolution (q) for combinations of the **B**, **G**, and **E** was calculated to be 0.987.

3.4 Review

3.4.1 Categories that are difficult to resolve

Combinations of representative points have improved the probability of resolution of structure matrices, as shown in Table 12.

Table 14. Value distribution of $Z(d)$ when using three kinds of representative points

d	$Z(d)$	
	B, M, E	B, G, E
1	1 947	1 973
2	1	1
3	0	0
4	0	1
5	0	0
6	0	1
7	0	0
8	0	0
9	0	0
10	0	0
11	2	0
12	2	1
13	0	1
14	0	0
15	1	0
16	0	0
17	0	0
18	0	0

Table 15. Categories of difficult resolution

Selected representative points	Category
B, G, E	愛磯液稼確
B, M, E	磯液稼餓開馨

However, to improve the probability of resolution, the categories containing indivisible partial patterns were checked and are as shown in Table 15.

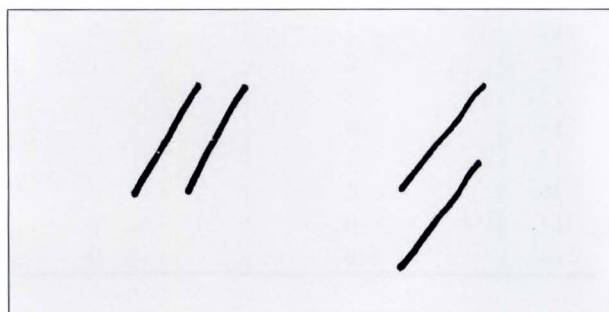
Some partial patterns in these characters do not satisfy the conditions for pattern resolution for any of the representative points.

The reasons for this are divided as follows:

- 1) A stability of 99.99 percent between two arbitrary strokes can be guaranteed by the appropriate selection of representative points for either the top-to-bottom relation or the left-to-right relation. But it cannot be guaranteed that all the pairs of strokes always have the same left-to-right (or top-to-bottom) relation.
- 2) The positional relation between two particular strokes in both the top-to-bottom and left-to-right direction may sometimes



Fig. 17—Left-to-right relation becomes sometimes unstable.



a) Left-to-right b) Top-to-bottom

Fig. 18—Two types of relational relations between leaning strokes.

be unstable.

In the case of 1) above, for example, in the kanji character 稼 shown in Fig. 17, its 5th and 7th strokes are mutually stable in the top-to-bottom direction, but are somewhat unstable in the left-to-right direction. In such a case, an attempt to resolve this character into a left portion containing strokes 1 through 5 and a right portion containing the remaining strokes will not succeed, due to the instability of strokes 5 and 7 in the left-to-right direction. Another example of 1) is the kanji character 餓. Since strokes 1 through 8 are all located to the left of the remaining strokes as viewed from the G, this kanji character can be resolved into a left portion and right portion. If the beginning points, mid-points and ending points are considered, however, the left-to-right relation between strokes 1 through 8 and some of the remaining strokes cannot be completely guaranteed. As a still

another example, the kanji character 確 cannot be resolved because the relation between stroke 7 and strokes 8-11 cannot be established for the B, G, E (the M of stroke 7 is always above strokes 8 through 11). Difficulties in resolving the kanji characters 開 and 馨, are considered to be equivalent to those in case 1) above.

Case 2 is an example with significant positional fluctuation due to individual differences, such as stroke 17 of the kanji character 磯. As with the relation between strokes 8 and 9 of the kanji character 液 and the relation between strokes 12 and 13 of the kanji character 稼, where the two diagonal strokes are parallel to each other, as shown in Fig. 18, the relation can be either a left-to-right relation or a top-to-bottom relation, depending on individual differences, and therefore neither the top-to-bottom relation nor the left-to-right relation of these characters as a whole is stable.

3.4.2 Introducing the diagonal approach

The preceding subsection reviewed the causes difficulty in resolving patterns for some categories.

Temporarily ignoring the dot or 17th stroke (final stroke) of the kanji character 磯, which fluctuates significantly due to the writers' habits, let us consider overcoming some other causes of instability with simple algorithms. One algorithm is a countermeasure for instability due to the relations shown in Fig. 18. In this case, the positional relation between the representative points, if not limited to the left-to-right or top-to-bottom relation, looks stable when viewed from upper left to lower right.

In general, if both the top-to-bottom relation and the left-to-right relation are instable, something irrational must be done to resolve the kanji pattern into the top-to-bottom relation or the left-to-right relation, unless it is a case of significant individual differences.

One method of solving this problem is to consider the stability of the upper left – lower right relation and the lower left – upper right relation in addition to the top-to-bottom relation and the left-to-right relation. In fact, much as for the kanji characters 開 and 馨 where the character structure consists of upper

Table 16. Value distribution of $Z(d)$ with the diagonal approach, using three representative points

d	$Z(d)$	
	B, M, E	B, G, E
1	1 999	1 999
2	0	0
⋮	⋮	⋮
10	0	0
11	1	1
12	0	0

left, upper right, and lower center portions, the interrelation of stroke sets should not be limited to the top-to-bottom or left-to-right relations.

Based on the foregoing study, experiments were carried out for cases where resolution conditions include diagonal relations, in addition to vertical or horizontal relations.

That is, the relations between stroke representative points $D_i(x_i, y_i)$ and $D_j(x_j, y_j)$, $x_i + y_i$ were compared to $x_j + y_j$, and the point with the smaller value was assumed to be the lower left and the point with the larger value the upper right. Similarly, $x_i - y_i$ and $x_j - y_j$ were compared, and the point with the smaller value was assumed to be the upper left and the point with the larger value the lower right. This is called introducing of the diagonal approach.

If this lower left – upper right relation or the upper left – lower right relation is stable, it is used to resolve the stroke sets.

Resolution was performed wherever possible, by using three types of representative points and introducing the diagonal approach. The results obtained are shown in Table 16. Using the value of q , the probability of resolution was evaluated to be $q = 0.995$.

This study, indicates that the probability of resolution for kanji patterns is 99.5 percent when the probability of the diagonal relation is considered in addition to the probabilities of the top-to-bottom relation and the left-to-right relation.

3.5 Summary

Each element of a structure matrix has two values, called the top-to-bottom relation and the left-to-right relation for each representative point of a stroke. If the most desirable observation method is used on each kanji category and each set of two specific strokes, observation can be performed with a stability of 99.99 percent. This was described in Subsec. 2.2.6.

In this section, experiments were performed for resolving kanji structures. These experiments were based on the assumption that kanji characters can be resolved in the top-to-bottom direction or the left-to-right direction. According to those experiments, it was found that up to 98.7 percent of kanji characters could be resolved. The principle of resolution is to observe as many specified representative points of a kanji character as specified in the dictionary, from either the top-to-bottom or the left-to-right direction, and to keep repeating such operations.

The probability of complete resolution was 98.7 percent for the categories shown in Table 1. This value is rather low, compared to the 99.99 percent stability of the relative positional relation between two arbitrary strokes of the same categories and patterns.

The major reason for this, as reviewed in Sec. 3.4, is that the resolution of a kanji character should not be limited to its top-to-bottom relation or the left-to-right relation, some kanji characters having shapes that can be resolved stably in the diagonal direction.

The principle of resolution was therefore improved so that a diagonal approach from either the upper left or the upper right direction is allowed for specific kanji characters, in addition to top-to-bottom and left-to-right resolution, and the probability of resolution was thereby raised to 99.5 percent.

The technique introduced in Sec. 3.4 for resolving kanji characters is thus seen to be satisfactory.

Table 17. Structure dictionary of the kanji character 位

Steps	Number of strokes	Approaching direction	Type of representative point
1	2	Left-to-right	M
2	1	Top-to-bottom	
3	1		
4	1		
5	2		
6	1	Left-to-right	

4. Kanji character recognition by structure resolution

4.1 Overview of the recognition algorithm

As described in Chap. 3, kanji characters can be resolved into partial patterns containing only one stroke, with a probability of 99.5 percent, by repeating the operations predetermined for each specific category.

The operations are to observe as many representative points as specified from the specific directions.

A list of operations for the kanji character 位 is shown in Table 17. Since this list of operations is a dictionary to be used for resolving the kanji character 位, it is called the structure dictionary for the kanji character 位.

Table 17 shows only the operational portions of the contents of Fig. 12.

Although it is not shown in Table 17, the execution of step 1 causes the strokes in stroke order 1 and 2 to be separated, and the execution of step 2 for the strokes in stroke order 1 and 2 causes strokes in stroke order 1 to be separated.

Since the kanji character has been resolved into partial patterns with only one stroke by steps 1 and 2, step 3 is executed for the remaining pattern to separate the stroke of stroke order 3. Step 4 is executed for the remaining pattern, and the stroke of stroke order 4 is separated. Then, step 5 is executed for the still remaining pattern, and the strokes of stroke orders 5 and 6 are separated, leaving only the stroke of stroke order 7. Step 6 is executed for the patterns that have just been separated

(strokes of stroke orders 5 and 6), and as a result, the stroke of stroke order 5 is separated, leaving the stroke of stroke order 6.

Thus, operations from step 1 to step 6 cause the kanji character 位 to be separated into parts containing only one stroke. If separation is successful, as shown in this case, the stroke order can be given for all the strokes in the original pattern (see Sec. 3.1).

The patterns to be resolved can generally be summarized as follows:

- 1) The entire kanji character is to be resolved by step 1.
- 2) If the number of representative points to be separated by step i (number of strokes to be separated) is two or more, this stroke group is to be separated by the next step {step $(i + 1)$ }.
- 3) If the number of representative points to be separated by step i is only one, the entire remaining part is to be resolved by step $(i + 1)$. However, if that remaining part consists of only one stroke, step i is the end step. A kanji character consisting of n strokes can be resolved with $(n - 1)$ steps.

Based on the above, and assuming that a given kanji pattern belongs to a certain category, a stroke order can be allocated to each stroke of the kanji pattern by applying the structure dictionary for the category. Then, using the allocated stroke order, each stroke is compared with the standard character pattern for that category to calculate the differences among strokes, and the sum of differences is considered to be the tentative difference of that character. This tentative difference is calculated for each predictable category (that is, for each of the categories whose number of strokes matches the number of strokes of the input pattern, and the category with the minimum tentative difference is regarded as the recognized category of the input pattern.

If the input pattern is correctly recognized, then its structure will be correctly resolved; therefore, each individual stroke of the input pattern matches the corresponding dictionary stroke, so the difference will become sufficiently small.

However, in the other cases, the structure of the input pattern is resolved forcibly by an irrelevant structure dictionary, and the individual strokes of the input pattern are forced to correspond to the individual strokes of an irrelevant dictionary. Therefore, the difference is much larger than that of a correct structure resolution.

4.2 Definition of difference

Following structure resolution, various methods are available for defining in detail algorithm for matching individual strokes with the corresponding strokes of the dictionary pattern (this is called stroke level matching), and needless to say, more research is necessary to select the best method. For convenience, Euclidean distance is used as the basis for calculating the difference, as this minimizes the effect of small differences.

For actual stroke level matching between the input pattern and the dictionary pattern, the input pattern must be normalized to the dictionary pattern. That is, the centers of gravity of the input pattern is laid over the dictionary pattern, and the input pattern is adjusted (expanded or shortened) so that the secondary moment matches that of the dictionary pattern³⁾. Following this normalization process, the *i*-th stroke of the dictionary pattern is assumed to be *t_i*, the corresponding input stroke to be *s_i*, and the *N* points that approximate each stroke to be *P_{ij}* and *Q_{ij}* (*j* = 1, ..., *N*), respectively.

Assuming the Euclidean distance between *P_{ij}* and *Q_{ij}* to be *PQ_{ij}*, the difference *d_i* between *s_i* and *t_i* is as follows:

$$d_i = \frac{1}{N} \sum_{j=1}^N (PQ_{ij}). \quad \dots\dots\dots (16)$$

Assuming the difference of the entire pattern to be *D*, then

$$D = \sum_{i=1}^n d_i, \quad \dots\dots\dots (17)$$

where *n* represents the number of strokes of this pattern.

4.3 Recognition experiments

4.3.1 Overview of experiments

The preceding section describes a new recognition technique that limits pattern matching to stroke-level matching, using the structure resolution algorithm, instead of matching the entire input pattern with the entire dictionary pattern. To verify the effect of this technique, two experiments were carried out.

1) Experiment 1

A recognition experiment was carried out based on the flowchart shown in Fig. 19, using the handwritten kanji patterns for 200 categories written by 40 writers (see Table 1).

A recognition ratio of 99.7 percent was achieved.

2) Experiment 2

Since many of the kanji characters used for experiment 1) above contain a different number of strokes and there are fewer categories

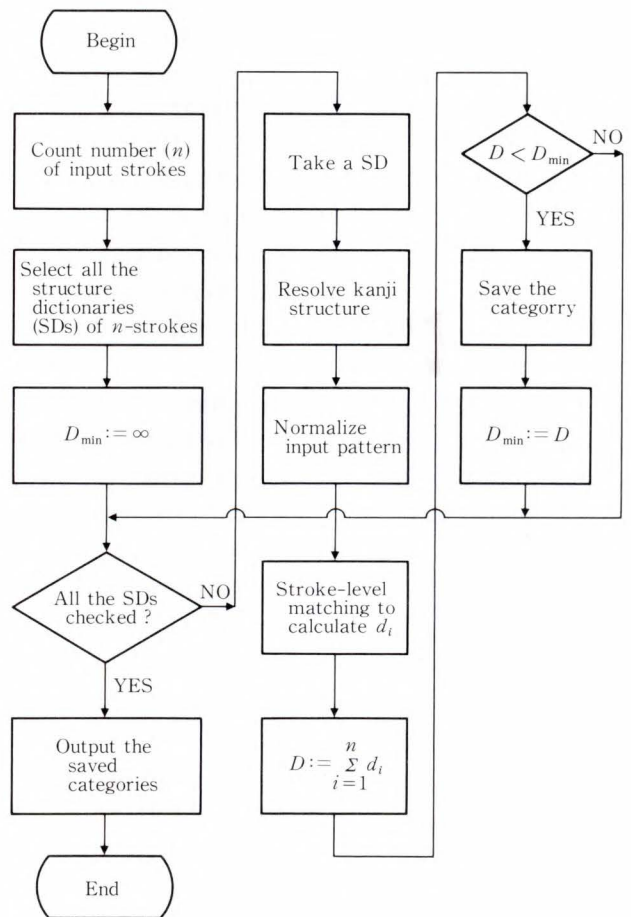


Fig. 19—Recognition flowchart.

Code	:	C	character code
Kakusū	:	n	No. of strokes
Tensū	:	N	No. of points
1	:	$X_{11} Y_{11}, X_{12} Y_{12}, \dots, X_{1N} Y_{1N}$	
2	:	$X_{21} Y_{21}, X_{22} Y_{22}, \dots, X_{2N} Y_{2N}$	
⋮	:	⋮	⋮
n	:	$X_{n1} Y_{n1}, X_{n2} Y_{n2}, \dots, X_{nN} Y_{nN}$	

Fig. 20—Form of pattern dictionary.

to be compared for the specific number of strokes, a higher recognition ratio may be easily achieved. Therefore, 203 categories of handwritten ten-stroke patterns were collected from 40 writers. These categories are shown in Table 2.

This is a worst case experiment in the sense that the number of these categories is the maximum among the numbers of categories for characters with the same number of strokes. To eliminate learning effect, the structure dictionary was written manually for each category, using human knowledge. As a result, a recognition ratio of 99.5 percent was achieved, and it was found that the increasing number of categories did not shift the recognition ratio significantly.

4.3.2 The dictionary structure

In the recognition experiments two dictionaries were prepared for each category: the structure dictionary and the pattern dictionary. The concept of the structure dictionary is as shown in Table 17, and the pattern dictionary is as shown in Fig. 20. The coordinate for the G of the pattern is assumed to be (0,0), and the frame of the pattern is assumed to be a square, one side of which is 100 units long. For example, the coordinate of the upper right corner of the frame is (+50,+50). Individual strokes within the frame are assumed to approximate n points of equal intervals, and their coordinates are recorded in the pattern dictionary. The numbers of the strokes are



Fig. 21—Sample pattern of a kanji.

Code	:	304C
Kakusū	:	7
Tensū	:	5
1	:	-18 42, -23 30, -29 19, -36 7, -45 -2,
2	:	-29 13, -26 1, -26 -10, -26 -22, -27 -37,
3	:	1 47, 5 45, 9 43, 11 38, 11 33,
4	:	-14 27, -1 28, 10 28, 22 30, 36 31,
5	:	-1 18, 0 6, 0 -5, 0 -17, 0 -33,
6	:	24 22, 22 10, 20 -1, 19 -13, 17 -28,
7	:	-18 -39, -2 -34, 12 -33, 27 -33, 45 -36,

Fig. 22—Pattern dictionary form of a kanji pattern shown in Fig. 21.

matched with the order in which they are extracted in structure resolution using the structure dictionary. (The structure dictionary cannot be guaranteed to match the natural stroke order, but it is considered likely to do so in most cases.)

The actual size of the dictionary is 13 Kbytes for a structure dictionary having 203 categories containing ten strokes, and 26 Kbytes for a pattern dictionary containing 5-point approximation. An example of a pattern and the contents of the pattern dictionary are shown in Figs. 21 and 22, respectively.

4.3.3 Recognition program

The program for the recognition experiment was compiled using the C language operating under the operating system (UNICUS) of a PANAFACOM U-1500. The program size is approximately 15 Kbytes. The recognition

Table 18. Difference of recognition ratio with/without information of writing order

Writing order	
Known	Unknown
99.78%	99.57%

Table 19. Relations between recognition and structure resolution

	Number of cases	
Resolution impossible and recognition impossible	13	35
Resolution successful and recognition impossible	22	
Resolution impossible and recognition successful	20	8 085
Resolution successful and recognition successful	8 065	
Sum	8 120	

speed per character is approximately proportionate to the number of categories with which the input patterns are to be compared. It was approximately four seconds for experiment 2), which was the worst case. By comparison, the recognition time in cases where the stroke order was known was approximately two seconds. The difference between the two times is considered to be the time required to link the input stroke to the dictionary stroke by structure resolution.

4.3.4 Results of experiments

The recognition process is divided into two stages: structure resolution and stroke level matching. A simple analysis was performed to determine how accurately the input strokes corresponded to the dictionary strokes through structure resolution, and the influence of this accuracy on the recognition ratio.

The patterns of the 203 categories of ten-stroke kanji characters were used for this analysis. Each stroke of these 8 120 input patterns (203×40) was manually given the correct stroke order. Then, stroke-level matching of these patterns was performed using dictionary patterns. Since the strokes corresponded completely in this case, the difference in rec-

ognition ratio is thought to have occurred during the structure resolution stage.

The difference between the recognition ratio in this case and the case where stroke order is known is 0.1-0.2 percent (see Table 18). To determine whether this difference occurred during the structure resolution stage, the recognition results were checked in relation to the structure resolution (see Table 19). It was expected that only correct structure resolution caused correct recognition, but the results included a few cases of correct recognition even when the structure resolution was not correct. This may be caused by the redundancy of kanji characters. However, a case where the writing order is known must have the same result as in a case of correct structure resolution. So it still can be said that the difference in the recognition ratio between cases in which the writing order is known and in which it is unknown is due to a failure in structure resolution.

The results of experiments 1) and 2) showed recognition ratios of 99.7 percent and 99.5 percent.

This algorithm features the use of structure resolution to make the individual strokes of the input pattern correspond to those of the dictionary pattern, instead of making a total comparison. While total comparison requires a processing time that is proportionate to the square of the number of strokes, structure resolution requires a processing time that is proportionate to the number of strokes; and, therefore, the relative efficiency of structure resolution increases with the number of strokes. Even taking into consideration that the total comparison method has a simple algorithm, the structure resolution in the case of ten-stroke kanji patterns requires a fraction of the time required for the total comparison method.

The stroke order used by any writer was ignored entirely, and the correct stroke order was reconfigured through structure resolution, so the dictionary need not contain countermeasures against incorrect stroke order. It was verified that patterns with unknown stroke order could be recognized with only one structure dictionary and one pattern dictionary.

Comparing the recognition method introduced in this paper to the method where the character has a fixed number of strokes and the order of all strokes is known, this method of processing needs double the time and the dictionary (byte) must be 1.5 times larger. That is, making correspondences between input pattern strokes and dictionary pattern strokes was accomplished in the same time as stroke level matching, using a dictionary which was 1.5 times larger.

4.4 Further considerations

As described above, 416 480 ($10\ 412 \times 40$) pairs of arbitrary strokes were checked for their relative positional relations, using the patterns of 198 categories of kanji characters handwritten by 40 writers.

However, since it was difficult to directly define the relative positional relation between two strokes, points were selected to represent the strokes and then the positional relations between those representative points were checked.

As a result, it was found that among the pairs of two arbitrary strokes of handwritten kanji characters (a total of 10 412 pairs for the 198 categories used for the experiments), 10 409 pairs had the same relative positional relations between the representative points, under a given condition, for all of the 40 different writers (see Table 11). The given condition was that the type of representative point (**B**, **M**, **E**, or **G**) to be observed and the direction (top-to-bottom or left-to-right) in which the observation was to be made were specifically determined for each pair of specific strokes in each specific category.

This condition does not include any conditions placed on the writers. Therefore, the results shown in Table 11 indicate that it is possible to observe stable information concerning kanji structure.

It is not known whether the same stability exists when changes are allowed in the number of strokes.

In the view of this writer, the sense that a certain partial pattern is to the left of (or

above) another partial pattern is not limited to individual writers. This sense does not change even when the number of strokes changes.

Therefore, the resolution method may be stable even when the number of strokes changes, but this remains to be confirmed in the future.

Although the series of operations for kanji structure resolution (the structure dictionary) is also stable information for a kanji character, its stability is lower than that of the information concerning relative positional relations between strokes. However, as discussed earlier, it is clear that the relative positional relations between a certain partial pattern and another partial pattern will be quite stable if the direction of observation (top-to-bottom, left-to-right, or diagonal) is determined for each kanji category. For example, it is not possible for the kanji character $\overset{\uparrow}{\downarrow}$ (position) to be written as $\overset{\downarrow}{\uparrow}$. However, the relative position in the top-to-bottom direction of the $\overset{\uparrow}{\downarrow}$ portion and the $\overset{\downarrow}{\uparrow}$ portion may be shifted, and their left and right positions may also get closer or a little farther apart, but inversion of the left portion and the right portion is impossible.

The structure dictionary is an implementation of these stable relations (see Fig. 12 and Table 17).

Possible future research includes:

- 1) Matching the structure matrix itself for recognition instead of stroke level matching.
- 2) This paper describes on-line handwritten characters, because strokes can be extracted easily, or rather the representative points of strokes can be extracted easily and, therefore, experiments can be carried out easily.

It will be proved, however, that the basic techniques described in this paper can be applied in not only on-line but also off-line processing.

- 3) This paper describes how a stroke of a kanji character is represented by one representative point, and this is possible because most kanji strokes are straight lines. For cursive characters such as those for handwritten alphanumeric characters and hiragana characters (Japanese cursive kana characters), a theory similar to the one described in

this paper may be developed using multiple representative points instead of one representative point.

- 4) Although this paper deals with kanji characters, more generalized applications may draw upon this research to consider the usefulness of replacing a certain pixel with a simpler pixel, or of replacing the relative positional relation of the original pixel with that of a simpler pixel.

This paper has described two types of stable information for kanji characters, the structure matrix and structure dictionary, and also described their interrelation. By using the structure dictionary as information for extracting stroke order for kanji character recognition through stroke-level matching, a recognition of 99.5 percent was achieved for kanji characters containing ten strokes.

The recognition method that uses a structure dictionary is called the structure resolution method. This method is significant when the kanji to be resolved consists of more than two strokes. If it contains only one stroke, this method is nothing more than stroke-level matching.

5. Conclusion

Two types of stable information for kanji characters have been described. One is the stability of the relative positional relation between kanji strokes, which can be summarized in the form of a structure matrix.

The other is the structure dictionary, which can assign unique numbers to the strokes of a kanji character of n strokes in $(n - 1)$ steps. In other words, this information is capable of giving the stroke order.

The structure matrix cannot be evaluated unless the stroke order is determined. Therefore, the structure matrix of the input pattern is evaluated after the stroke order of each stroke has been determined by applying the structure dictionary to that input pattern.

The structure dictionary can be produced using human knowledge, that is, the knowledge that one partial pattern is to the left of another partial pattern, etc., and it can also be produced

automatically from the structure matrix by the algorithm described in section 3.2. In the latter case, the structure matrix must be defined first, so in this case, the correct stroke orders of the experimental patterns to be collected must all be known.

6. Acknowledgement

The writer gratefully acknowledges helpful discussions and enlightening comments given during this work by Honorary Professors H. Enomoto and T. Iijima and Associative Professor N. Yonezaki at the Tokyo Institute of Technology. Acknowledgement is also due to Messrs. T. Fujita, T. Morishita, and M. Ohura of Fujitsu Laboratories for their discussions and assistance in collecting the data and, in programming.

References

- 1) JIS C 6226: Code of the Japanese Graphic Character Set for Information Interchange. Japanese Standards Association (1978).
- 2) Odaka, K., Arakawa, H., and Masuda, I.: Online Recognition of Handwritten Characters by Approximating Each Stroke with Several Points. *Trans. Inst. Electron. Commun. Eng., Jpn.*, **J63-D**, 2, pp. 153-160 (1980).
- 3) Odaka, K., Arakawa, H., and Masuda, I.: On-line Recognition of Handwritten Characters by Approximating Each Stroke with Several Points. *Elect. Commun. Lab. Tech. J.*, **29**, 11, pp. 1899-1918 (1980).
- 4) Odaka, K., Wakahara, T., and Masuda, I.: Stroke Order Free On-line Handwritten Character Recognition Algorithm. *Trans. Inst. Electron. Commun. Eng., Jpn.*, **J65-D**, 6, pp. 679-686 (1982).
- 5) Wakahara, T., Odaka, K., and Umeda, M.: Stroke Number and Order Free On-line Character Recognition by Selective Stroke Linkage Method. *Trans. Inst. Electron. Commun. Eng., Jpn.*, **J66-D**, 5, pp. 593-600 (1983).
- 6) Sato, Y., and Ichihara, T.: Feasibility Study on On-line Character Recognition of Cursive Writings Using Feature of Writing Pressure. in PRL 83-23, (1983).
- 7) Wakahara, T., and Umeda, M.: On-line Cursive Script Classification Using Stroke Linkage Rules. *Trans. Inst. Electron. Commun. Eng., Jpn.*, **J67-D**, 11, pp. 1285-1292 (1984).

8) Kobayashi, S., ed.: Shinsen Kanwa Jiten, (A Dictionary of Kanji Character Explained in Japanese). 2nd ed., Tokyo, Shogakukan, 1980.

9) Kato, O., Fujita, T., Miwa, M., Morishita, T., Fujii, A., and Tanahashi, J.: A Handwriting Input System for Japanese. *Proc. Inter. Feder. Infor. Proc.*, **80**, pp. 689-694 (1980).



Yasuo Ishii

Information Processing Network Center
FUJITSU LABORATORIES, KAWASAKI
Since 1988, TOKYO UNIVERSITY OF
INFORMATION SCIENCE
Bachelor of Applied Physics
The Tokyo University 1954
Dr. of Electrical Eng.
Tokyo Institute of Technology 1986
Specializing in Software Engineering

Cooperative Expert System Applied to Simulation of Human Group Behavior

• Nobuo Watanabe • Takashi Kimoto

(Manuscript received March 2, 1988)

This paper describes a model for a cooperative expert system which simulates human group behavior. When social phenomena are observed, Fujitsu has realized that experts usually act autonomously. But there are also many cases when experts must work in close cooperation. The major design goal of this study is to construct a framework to naturally represent cooperation among expert systems. Since expert systems interact only via conversation, an expert system cannot access or change another expert's knowledge base without the owner's permission. This system can also process non-deterministic tasks by parallel inference.

1. Introduction

There are few tasks that can be done by a single person. When we confront a problem that is not in our area of expertise, we ask a specialist and follow his advice on how to solve the problem. To solve the problem using computers, a study aimed at human group behavior instead of individual behavior is required. A system that simulates the world of many experts is useful for this study.

Our cooperative expert systems can represent such a world and can simulate its behavior naturally. This paper describes our attempt to design a distributed system based on cooperation among many expert systems, and our experimental system which simulates a historic battle fought by warlords of ancient Japan.

2. Advantages of distributed AI

Distributed systems have the advantages of speed, reliability, and expandability. These advantages of distributed artificial intelligence systems are described below.

2.1 Parallel processing

Parallel processing makes the system faster

and expands the system's capacity. For example, many parallel searches of a search tree or parallel execution of rules is enabled.

2.2 Tools for distributed systems

When the system involves objects that are far apart from each other, an effective measure against speed reductions caused by the data traffic is to process the lower level tasks locally and process higher level tasks centrally. This idea has a wide application. Sensor network systems, air traffic control systems, and distributed database systems are potential applications.

2.3 Individual expert systems

The quality of inference can be improved if many agents process the same task from different points of view. In addition, the arrangement of expert systems at different sites can raise the independence and privacy of individual knowledge.

The independence of individual knowledge is discussed first. The best representation of knowledge depends on the field of the task. Many models support multiple paradigms in a single expert system, but we believe it is simpler

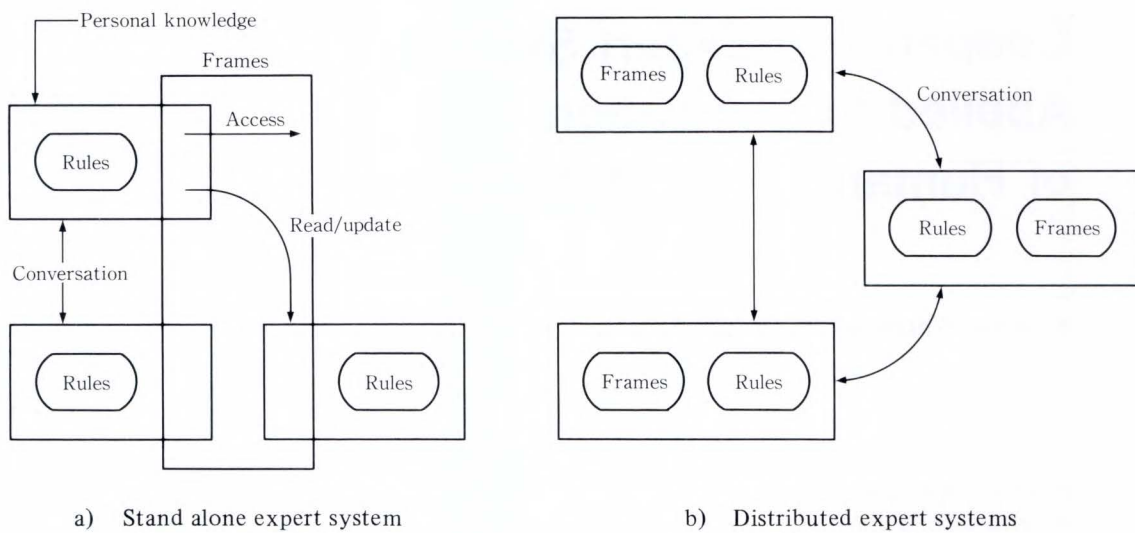


Fig. 1—Access to personal knowledge.

and more powerful if a single system has multiple expert systems based on different paradigms.

Second, it is important to consider security. In some professional fields, the expert is prohibited from disseminating his knowledge. The expert may also want to keep his knowledge a secret because of its value. In such cases, the knowledge of many people cannot be put together in a single expert system. Instead, it is better that each person manages his own knowledge. Such a complex intelligent system must also support a function whereby each agent can give others only the result and a brief explanation instead of the knowledge itself.

Consider the expert systems consisting of rule-based knowledge and frame-based knowledge (see Fig. 1). In a stand alone expert system, boundaries of individual knowledge become vague and it is difficult to determine how strongly a change in the knowledge will influence another person's action. Further, experts might be worried about unauthorized persons reading or changing his knowledge base. In distributed expert systems, an agent cannot access another's knowledge base without a conversation with the owner agent of the knowledge. This is a useful function to eliminate users' concerns about security.

3. Cooperative expert systems

Our model of cooperative expert systems is mainly aimed at the third advantage. An agent — processing object — represents one person. If the agents incorporate their knowledge, it increases cooperation and competition.

If a stand alone expert system simulates one person's thought process, then cooperative expert systems simulate a human group's behavior. Each agent plays a different role in the organization, and they work on the task with frequent interaction. It is interesting to apply this model to simulate animal behavior or in a more complex example, to simulate a human group's behavior under fire.

3.1 Requirements for individual agents

The many agents act concurrently and change the common environment simultaneously. Therefore, each agent is required to collect the latest information, and to plan and act dynamically because he cannot analyze the task and plan the solution in advance.

Each agent must have the functions described below.

- 1) Updating his world model simultaneously.
- 2) Collecting information from other agents.
- 3) Replanning based on new situation.
- 4) Replying to other agents' requests.

- 5) Requesting other agents to act for own benefit.

3.2 Problems

To clearly understand the cooperation, an experimental system was configured using 18 personal computers (Fujitsu FM16 β) that were connected by a network. One agent was assigned to each computer. This configuration makes it easy to understand that each agent can act independent of the others. We represent each knowledge base using rule-base and frame-base paradigms. The solutions to the above requirements are given below.

3.2.1 Simultaneous updating of each world model

The world model is common data that every agent can access.

It is constantly changing which causes a problem for all distributed database systems. The way in which each site manages the common data increases the amount of traffic to access. However, the way in which each site obtains a copy of the common data makes it difficult to make their copies exactly the same.

This inconsistency problem is the most serious problem for distributed database systems; but if our goal is to simulate human group behavior, this inconsistency instead becomes a rather interesting feature. Humans tend to act based on what they see rather than on the real world itself. A person acts, and if he doubts the environment, he senses the world again and replans.

Under these circumstances, we decided that each agent should have his own copy of the world model which is updated when the management computer sends update packets. Each agent draws an inference based on an old copy of the world.

3.2.2 Information collection from other agents

Individual agents have their own knowledge. That is why agents cannot use another agent's knowledge without the owner's permission. To obtain another agent's knowledge, they must interrupt the destination agent who might

be busy inferring. This approach makes it possible for the owner of the knowledge to decide whether to show or to hide his knowledge. This is one kind of request, but it is important to separately consider the individual management of the knowledge base.

3.2.3 Replanning when a new situation arises

We often find that a prior condition for an agent becomes inadequate when another agent updates the world model. In such cases, what does a human do? He acts based on what he sees. If he notices that the result is different from what he expects, he determines that some assumptions are inappropriate and checks the environment to see what has changed. It is difficult for a human to continue inference using variables that represent possible changes on some future day. This system, a simulator of a human group, has chosen the human way of inference. In this approach, the system assumes that a prior condition may not change until it processes one step of inference. Then it checks the world model to see whether the condition still holds. It is quite possible that this kind of inference leads to wrong conclusions, but it is more similar to human inference than "strict" inference.

While our system has this benefit, we must use the knowledge source considering that an action seldom leads to the expected result.

3.2.4 Answering other agents' requests

To enable timely answers to other agents' requests, a special knowledge source called "answering knowledge source" was added to each agent. This can be regarded as a kind of interrupt routine. As with ordinary interrupt routines, careful coding is needed because this special knowledge source is called during inference. Our system cannot guarantee consistency after calling the knowledge source.

3.2.5 Asking other agents for help

It is difficult to decide the protocol of conversation among agents. Different applications require different terminology, so it is possible that the best protocol depends on each application. Since we cannot decide the

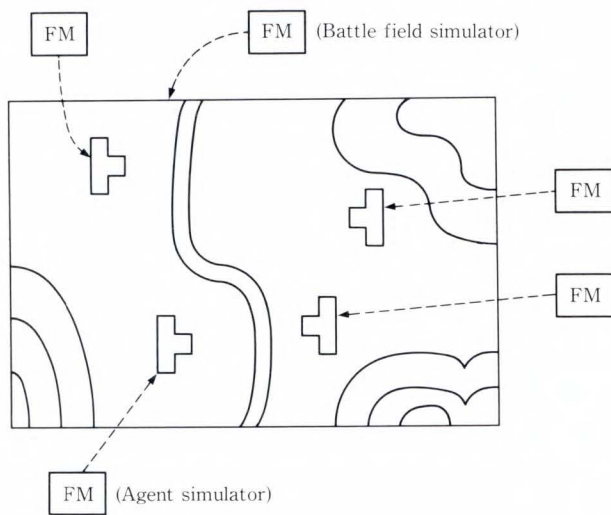


Fig. 2—Simulation game system using personal computers.

best universal protocol, our experimental system used a variety of protocols: from keywords that the receiver knows in advance, to S-expressions that the receiver has to evaluate. Although we avoided this problem in order to construct the entire system quickly, we are very interested in this problem of conversation among machines.

4. Application of a simulation game system

An experimental simulation game system was developed as an application of cooperative expert systems (see Fig. 2). The cooperative system can solve one problem being worked on by many agents. It has many agent computers that infer using their expert knowledge, and has a battlefield computer that simulates the battlefield and controls the network traffic.

The simulation game is a board game in which the many pieces represent army corps simulating a past battle. Unlike other games such as chess, more than one piece can be moved at a time which is a good example of cooperative inference. An ancient Japanese battle called the Battle at Sekigahara was simulated to test not only the historical accuracy but also a variety of hypotheses.

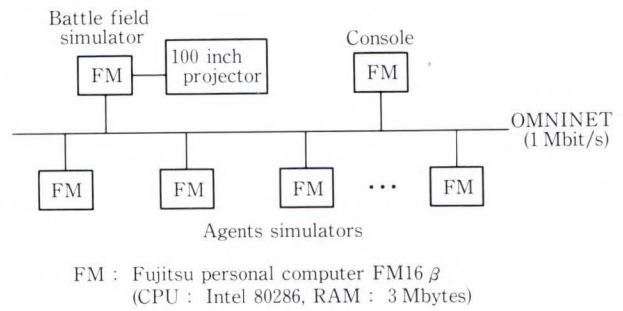


Fig. 3—Configuration of cooperative expert system.

4.1 System configuration

4.1.1 Hardware configuration

Figure 3 shows the configuration of the experimental system. Twenty personal computers (Fujitsu FM-16 β) were connected using Omnet which is the standard network bus for personal computers.

Personal computers were used for one of the following three purposes:

1) Battlefield computer

Only one of the twenty computers acts as the battlefield computer. It simulates the world model (battlefield), broadcasts the simulation result, judges the battle, and displays the battlefield on a 100 inch projector.

2) Agent computers

Eighteen computers play as pieces (agents) of the game. Each agent corresponds to one commander and his men.

3) Console computer

One computer is for the human operator to start, break, restart, and end the simulation.

4.1.2 Software configuration

Figure 4 shows the software configuration. The operating system of each computer is MS-DOS Version 3.1. The network controller module is CP-MGR Version 1.0 (includes pseudo-multi-tasking and computer communication). All modules except the network controller have been developed using GCLISP.

Major module sizes are as follows:

- 1) Master controller: 3.0 Ksteps
- 2) Agent monitor: 3.0 Ksteps
- 3) Master simulator: 1.3 Ksteps
- 4) Display module: 1.9 Ksteps
- 5) Inference engine: 1.0 Ksteps

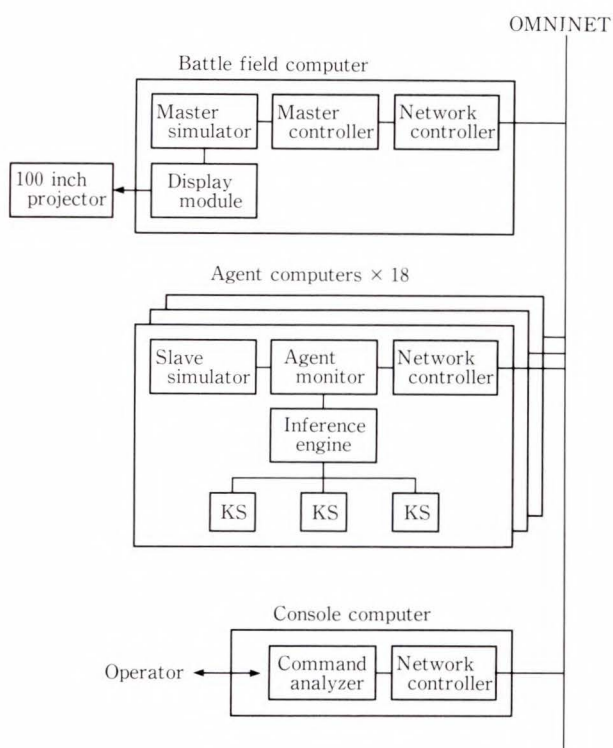


Fig. 4—Software configuration.

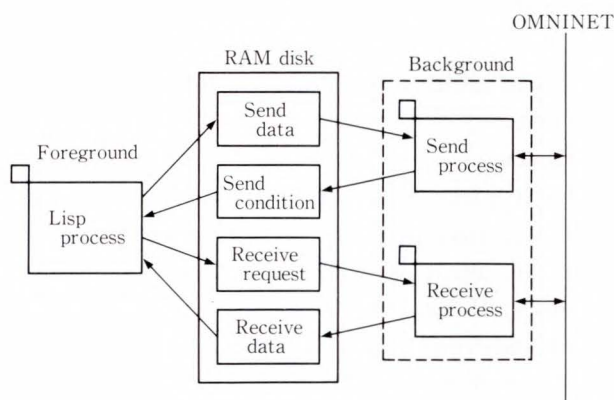


Fig. 5—Network control processes.

6) Knowledge source: 4.0 Ksteps

4.1.3 Network control

Figure 5 shows how agents communicate with each other via Omnet. Each computer has two background processes: a send process and a receive process. The main process communicates with these processes via RAM disk (file-like formatted main memory). Figure 6 shows the send processing sequence and Fig. 7 shows the receive sequence. Figure 8 shows the

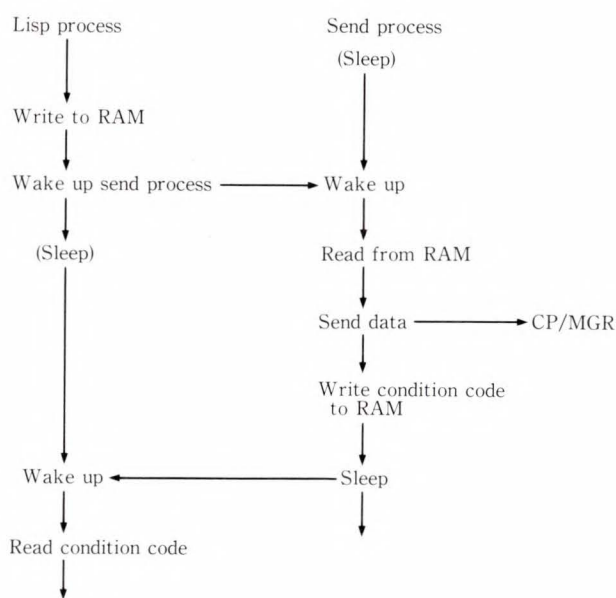


Fig. 6—Send sequence.

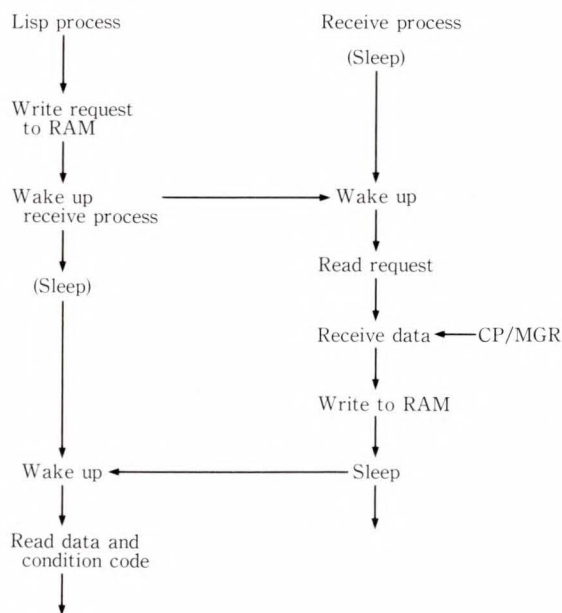


Fig. 7—Receive sequence.

data format for RAM disk. The module was divided into three processes because GCLISP does not have the function to call CP/MGR directly.

4.2 Rules of the game

This simulation game is similar to chess except that many pieces can move at the same time.

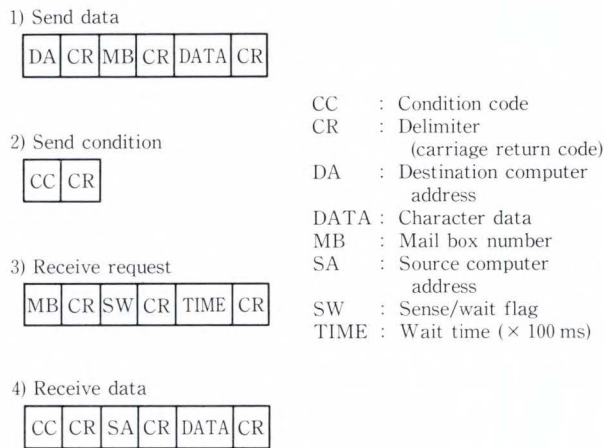


Fig. 8—Send/receive frame format (in RAM disk).

4.2.1 Processing sequence of the game

Simulation is divided into turns.

One turn has the following three phases:

1) Moving phase

All agents move at the same time. Normally in a board simulation game, the two teams move at different times. This rule was changed to make the game more like a real battle.

2) Cannon phase

All agents having cannon can fire their cannon once in this phase.

3) Fight phase

All agents can attack other agents.

Figure 9 shows the sequence of the master control module in the battlefield computer. In each phase, all agent computers send action packets to the battlefield computer. Because the battlefield computer processes those packets one by one, simulation becomes non-deterministic. For example, suppose one agent sends a move packet to a place that was empty last turn. If another agent has moved there first, then the first agent would receive a result packet that says “could not move there”. Due to this non-determinism, the simulation will be different from time to time.

4.2.2 Battlefield

1) Map

The battlefield was represented as a map consisting of many unit areas. Each unit area has an attribute such as a plain, hill, river, woods, or road. Some parameters are dependent

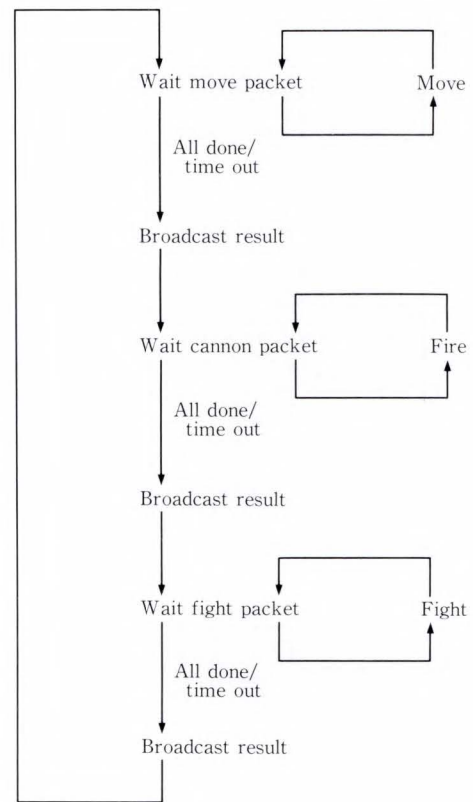


Fig. 9—Sequence of master controller.

on this attribute: moving rate, attack rate, and view rate.

2) Pieces

Each piece has one variable attribute and five static attributes. Life is a variable attribute. When an agent is attacked by others his life decreases. If his life becomes zero, he dies and is removed from the battlefield.

Other attributes are static. Moving power is an agent’s ability to move on a plain field in one turn. Moving ability on other fields is derived from the product of the agent’s moving power and the area’s moving rate.

Defense power is the agent’s ability to decrease the enemy’s attacking power. Real damage is determined by the product of the agent’s own defense power and the enemy’s attacking power.

Attacking power is the agent’s ability to take an enemy’s life.

Attack range is the distance within which an agent can attack the enemy.

View range is the distance within which an

agent can see other agents.

3) Move

An agent can move to any empty area if the distance is within his real moving ability. Moving ability is the product of the agent's moving power attribute and the moving rate of the area where the agent is located. Even if there is another agent on the way to the same destination, he can move unhindered.

4) Attack

An agent can attack any enemy within his real attack range. The damage to the enemy is the product of his attack ability, the enemy's defense power, and some random number. If the enemy does not die in the first attack, the enemy can make a counterattack soon after.

5) End of battle

Each player determines whether or not the battle is concluded according to the circumstances.

4.3 World model simulator

The world model simulator simulates the battlefield and move/attack action of the agents. The master simulator in the battlefield computer controls the entire sequence of move/attack actions of all agents and does not get involved in the conflict. The slave simulator in each agent computer replies to the information collection requests from agents to reduce the amount of data transferred. The slave simulator updates the world model based on

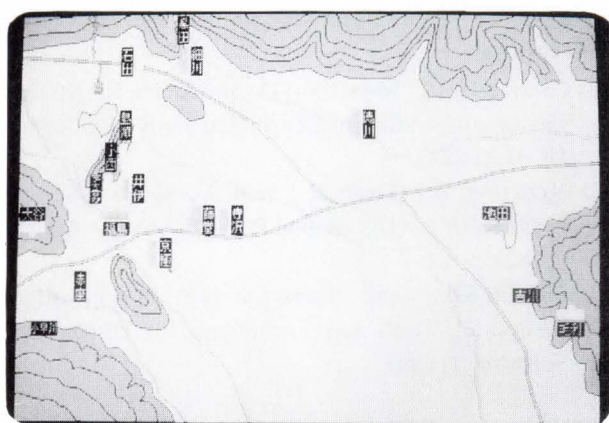


Fig. 10—Display output of world model simulator.

the update packet from the master simulator. Figure 10 shows the display output of the world model simulator.

4.4 Outline of experimental system

4.4.1 Agent monitors and knowledge sources

The agent monitor calls knowledge sources to move, fire, and fight; sends the action packet to the master controller in the battlefield computer, and receives the result packet from the master controller. The agent monitor also has inter-agent communication functions to cooperate with other agents. We developed two types of communication functions: an orderly (one to one communication), and signal fires (one to all communication). Each agent has at least four knowledge sources: moving, fighting, responding to signal fires, and responding to orders. These knowledge sources are previously registered with the agent monitor, and the agent monitor calls them as required. Knowledge sources for responding to signal fires and orders are called as soon as the corresponding packets arrive. Figure 11 shows the display output of the agent monitor.

4.4.2 Functions of agent monitors

The agent monitor calls three knowledge sources in one turn in the following sequence: moving, firing, and fighting. It waits for the result packet after each call to update the slave world model (see Fig. 12).

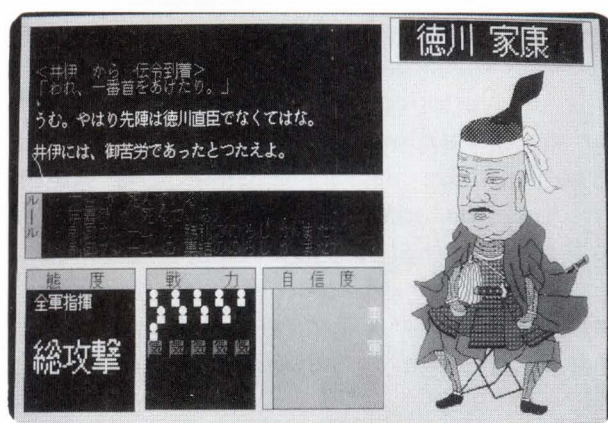


Fig. 11—Display output of agent monitor.

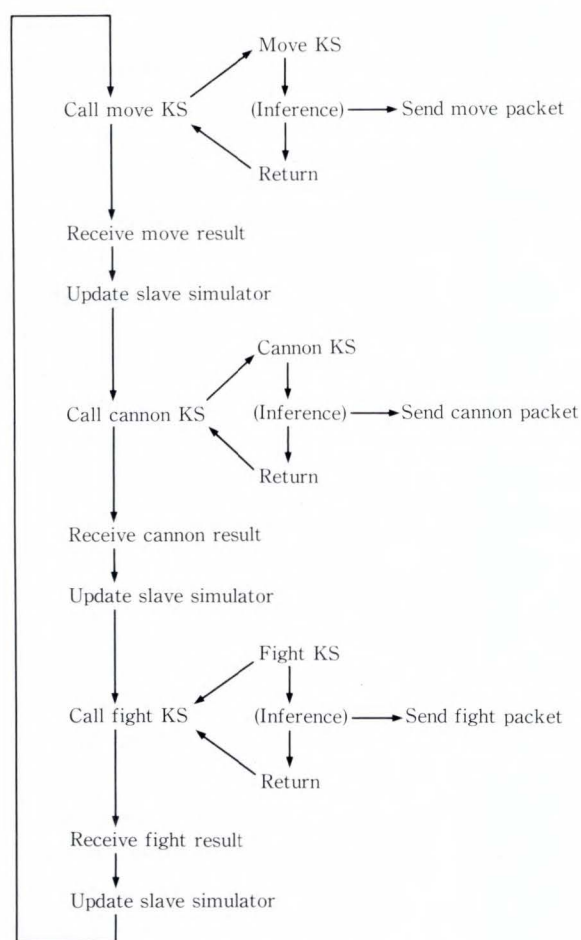


Fig. 12—Sequence of agent monitor.

4.4.3 Simulation

The simulation was tested based on an old Japanese battle in 1600 called the Battle at Sekigahara. The rule-based bits of knowledge were created based on the character, army forces, financial resources, and personal expertise of eighteen important commanders. The system can perform a simulation based not only on historical facts, but also based on various hypotheses. The results based on the hypotheses are described below. The system performs the simulation non-deterministically so the result is not always the same.

Because our agents do not have the ability to learn, they can deal with only the events that are known in advance. The simulation

shows that even these poor agents can cooperate with each other with some very interesting results.

1) Making a commander's will stronger

First, a commander's will was changed to make it stronger. In real history, commander Kobayakawa betrayed his side due to a threat. In this simulation he did not betray and many commanders observing his attitude took his side and they won.

2) Decreasing the threshold of judgement in his men

Second, Ishida's threshold of having confidence in his men was decreased. In real history he led one side and lost. In this simulation he won to his side many commanders and subsequently won.

3) Replacing one commander with his father

Lastly, Nagamasa Kuroda was replaced by his father Josui Kuroda who was a famous and resourceful general. When the battle came to a standstill, he appealed to the commanders observing the battle situation and organized a third group.

5. Conclusion

A model for a cooperative expert system was proposed to simulate human group behavior and an experimental simulation game system was developed as an application. This model is useful for such an application, but there are problems which require further study: learning, protocols of conversation, and world model conflicts being the most interesting problems.

References

- 1) Cammarata, S., McArthur, D., and Steeb, R.: Strategies of cooperation in Distributed Problem Solving. IJCAI, (1983).
- 2) McArthur, D., Steeb, R., and Cammarata, S.: A Framework for Distributed Problem Solving. AAAI, (1982).
- 3) Filman, R.E., and Friedman, D.P.: Coordinated Computing Tools and Techniques for Distributed Software. (1984).



Nobuo Watanabe

Artificial Intelligence Laboratory
FUJITSU LABORATORIES,
KAWASAKI
Bachelor of Information Science
Tokyo Institute of Technology 1979
Master of Information Science
Tokyo Institute of Technology 1981
Specializing in Artificial Intelligence,
Neural Networks



Takashi Kimoto

Artificial Intelligence Laboratory
FUJITSU LABORATORIES,
KAWASAKI
Bachelor of Computer Science
Gunma University 1980
Master of Computer Science
Tohoku University 1982
Specializing in Artificial Intelligence,
Neural Networks

ISDN Subscriber Loop Transmission LSI Using Echo Cancelling Method

• Toshitaka Tsuda • Misao Fukuda • Yutaka Awata

(Manuscript received December 1, 1987)

This paper describes a 144 kbit/s digital subscriber loop (DSL) transmission system based on hybrid-mode transmission with an echo cancelling method. It uses advanced LSI technology to obtain compactness, low cost, and high reliability. An echo canceller (EC) LSI has been developed using CMOS technology. Combined with the multiplexing processor (MXP) LSI, the EC LSI provides basic DSL equipment functions. The system consists of a specially arranged frame format with a newly developed DPLL circuit for stable timing extraction, and automatic balancing network, and a two-stage echo canceller.

Using this line termination circuit, the DSL equipment showed a reach of over 6 km when used with 0.5 mm diameter cable for 160 kbit/s bidirectional digital transmission.

1. Introduction

The world is entering the ISDN era, where a variety of services will be offered through a unified user/network interface. This can be done by establishing an end-to-end digital link. Therefore, for the penetration of the ISDN, the economical realization of bidirectional digital transmission on existing copper pair cable is mandatory. Extensive studies are under way in this field, and some results have been published¹⁾⁻¹⁰⁾. Two promising transmission technologies are emerging, one being time compression burst-mode transmission (the ping-pong method) and the other being hybrid-mode transmission using an echo canceller.

For hybrid-mode transmission, a unique method which relieves the system from the problem of timing recovery is proposed¹¹⁾. Based on this method, a digital subscriber loop (DSL) transmission system was developed. A two-chip method, shown in Fig. 1, was selected for making the DSL equipment. One chip is for circuit termination, with the main

function of forming a transmission format including frame synchronization. Since the processing is done by software in the multiplexing processor LSI (MXP), this chip provides system engineers with maximum flexibility in designing a transmission frame format¹²⁾. The other chip is the line termination LSI (EC LSI). Its main functions are echo cancellation, line equalization, and timing extraction.

The EC LSI, now complete, uses the CMOS process¹³⁾. The LSI is described in some detail in this paper. It exhibited excellent performance, such as error-free transmission over more than 6 km of 0.5 mm diameter cable, and a quick activation time of less than 220 ms.

Chapter 2 of this paper briefly compares the burst-mode and hybrid-mode transmission, Chap. 3 describes the design concepts, Chap. 4 describes the transmission frame format used in the authors' approach, Chap. 5 describes the circuit configuration and the activation procedure, and Chap. 6 discusses the actual LSI and its performance.

The contents of this manuscript was published in part by the IEEE Journal on Selected Areas in Communications in April, 1988.

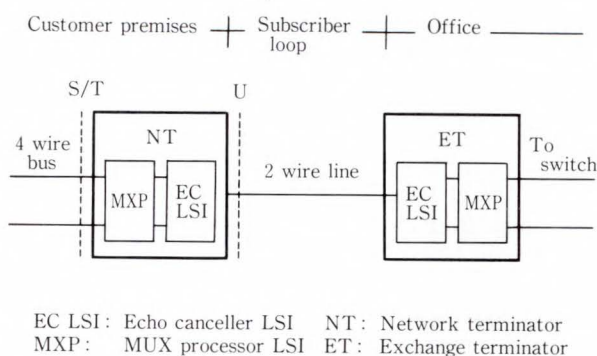


Fig. 1 - Digital subscriber loop transmission.

2. Comparison of the burst-mode and hybrid-mode transmission

2.1 Transmission technique

Figure 2 shows a schematic diagram of the burst-mode and the hybrid-mode transmission systems.

In the burst-mode transmission of Fig. 2-a), data to be transmitted is time-compressed into packets. Bidirectional digital transmission is achieved by alternately transmitting the packets of burst signal in each direction between the exchange terminator (ET) and the network terminator (NT). Therefore, on the subscriber loop, the received signal is free from the interference of the transmitted signal, while the line bit rate of the packets of burst signal exceeds twice the information data rate. The burst-mode transmission, which is based on a simple principle, is comparatively easy to apply to the equipment. Moreover, since the transmitted and received signals are separated on a time axis, the near end crosstalk is avoided using the burst-synchronization technique, where phases of the burst signals of all the subscriber loops are synchronized and transmitted simultaneously from the ET⁵⁾.

Hybrid-mode transmission, using the echo cancelling method shown in Fig. 2-b), enables simultaneous bidirectional digital transmission, or a full duplex digital transmission. Separation of the transmitted and received signals is performed using a conventional hybrid transformer. The problem of this technique is the large echo leakage. The echo peak amplitude of the transmitted pulses suppressed by the

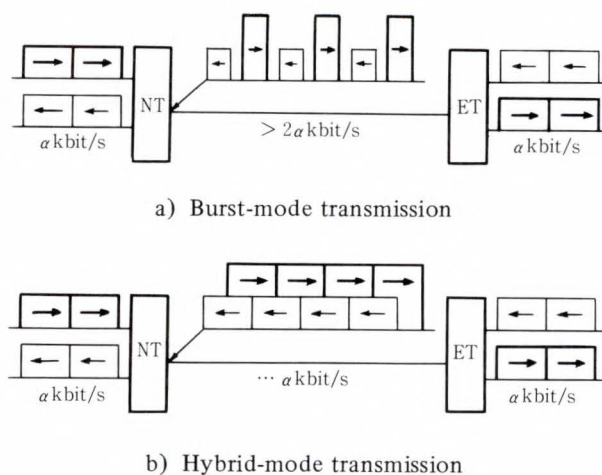


Fig. 2 - Transmission techniques.

hybrid transformer has a 10-dB loss compared with the transmitted signal amplitude, while the minimum received signal amplitude has a 50-dB loss due to the \sqrt{f} loss characteristics of the subscriber loop. The key to realizing hybrid-mode transmission is the construction of a high-performance echo canceller which achieves echo cancellation of over 60 dB. Despite this difficulty, the hybrid-mode transmission is considered a promising method, because the line bit rate is almost the same as the information bit rate, which is about half compared with that of the burst-mode transmission. The reduction of the line bit rate is a great advantage for the digital subscriber loop transmission because the subscriber loop loss increases in proportion to the square-root of frequency, or the transmission line bit rate. This means that the hybrid-mode transmission is expected to obtain a longer reach of digital subscriber loop transmission.

2.2 Circuit structure

Figure 3 shows block diagrams of the DSL equipment for burst-mode and hybrid-mode transmission. The MXP LSI, which performs the circuit terminating functions, is used for both methods. The circuit structure of the hybrid-mode transmitter (U/B, DRIV) is the same as that of the burst-mode transmission of Fig. 3-a), as shown in Fig. 3-b). An adaptive echo canceller (EC) and a balancing network circuit (BN) are added to the hybrid-mode

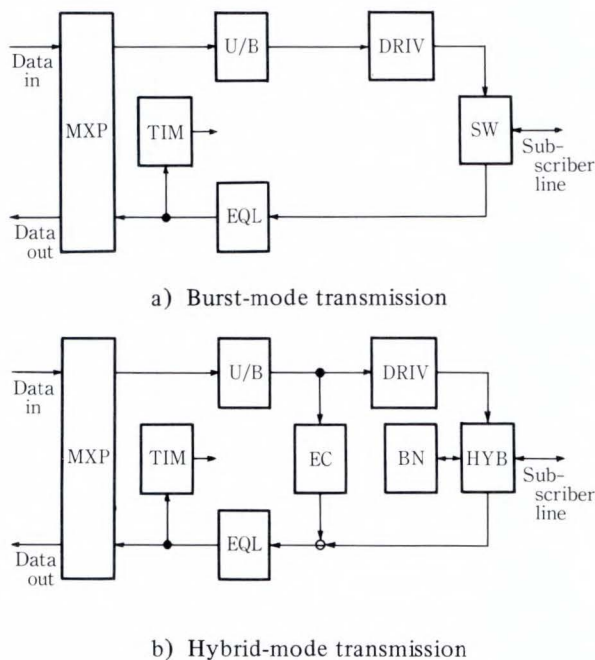


Fig. 3—Circuit structure.

receiver for the echo cancellation. Apart from the echo canceller and balancing network circuit, the timing extractor (TIM) and the line equalizers (EQL) which contain the \sqrt{f} AGC equalizer and the decision feedback equalizer are almost the same as those of the burst-mode transmission system. Consequently, the hybrid-mode transmission system requires a complicated circuit structure and large circuit scale for the echo canceller and the balancing network circuit.

Taking account of the above-mentioned characteristics of both methods, an LSI for burst-mode transmission was developed in the first stage, and proved to have good performance¹⁴⁾. An LSI for hybrid-mode transmission was developed in the second stage. The technologies employed in the development of the burst-mode transmission LSI were applied to this line terminating LSI using the echo cancelling method, which is described in this paper in some detail.

3. Design considerations and solutions

The following points were considered in the design of the transmission system and circuit structure.

Table 1. Main specifications for the echo canceller LSI

Line bit rate	160 kbit/s, 96 kbit/s
Channel capacity	2B + D (160 kbit/s) B + D (96 kbit/s)
Line code	Bipolar (AMI)
\sqrt{f} equalizer dynamic range	0-50 dB at Nyquist frequency
Decision feedback equalizer	2 taps (1 T, 2 T)
Echo canceller	Balancing network + 2-stage echo canceller > 70 dB
Peak jitter width	< 5%
Manufacturing process	Si-gate CMOS

- 1) To avoid the use of high-precision components
- 2) To reduce the number of gates
- 3) To use as simple and stable an algorithm as possible
- 4) Suitable partitioning of functions to analog and digital circuits
- 5) Reasonable distribution of the processing load to each functional block

As a result of the study, the transmission system and EC LSI developed by the authors have the following characteristic functions:

- 1) A specially formatted transmission frame structure with a newly developed DPLL circuit is adopted for simple and stable timing recovery.
- 2) An automatically selected balancing network is used to reduce the load of the echo canceller by suppressing the echo leakage.
- 3) The echo canceller has a two-stage structure to reduce the echo replica precision.
- 4) The line equalizing function is partitioned into an analog linear \sqrt{f} AGC equalizer and a digital decision feedback (DFB) equalizer.
- 5) An alternate mark inversion (AMI) line code is used because of its simplicity.
- 6) Echo cancellation and DFB equalization are performed simultaneously with a common D/A converter to reduce the number of gates.

Table 1 lists the main specifications of the EC LSI. It should be noted that two line bit rates are provided, one for (2B + D) channel

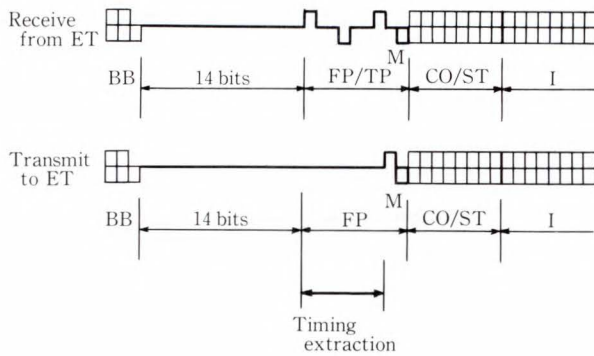


Fig. 4—Timing diagram for timing extraction.

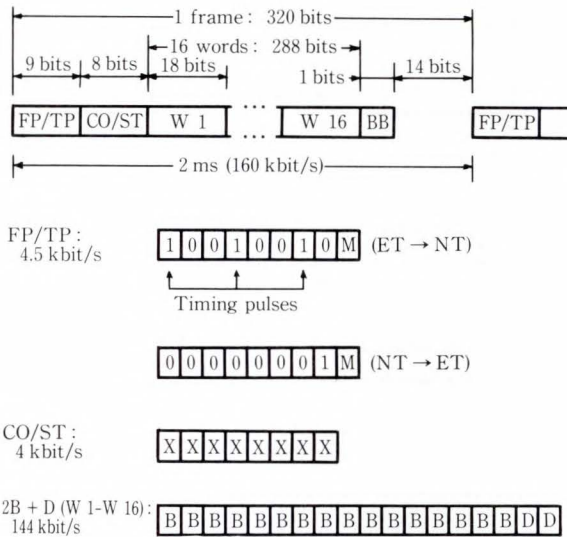


Fig. 5—An example frame format for 160 kbit/s line transmission.

transmission and the other for (B + D) channel transmission. The latter is designed to offer a digital link on a longer cable, although the channel capacity is limited.

4. Frame format

Since the echo cancelling method requires very stable timing clocks to perform highly precise echo cancellation, a specially arranged frame format was adopted to achieve stable timing extraction¹¹⁾. The frame is constructed with frame/timing pulses (FP/TP) which contain an 1/0 alternating bit (M), control/status bits (CO/ST), information bits (I) and a dc balancing bit (BB). Figure 4 is a detailed timing diagram for timing extraction at the NT. Frame pulses of

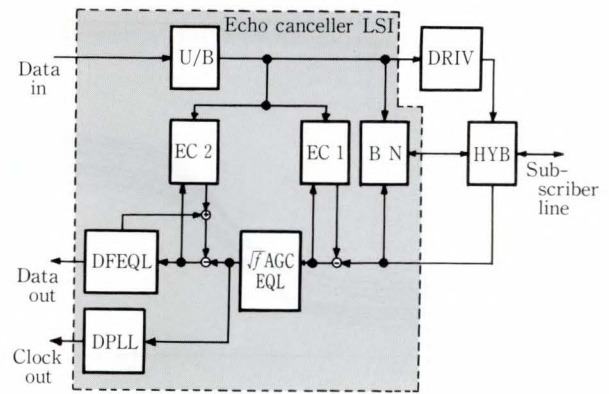


Fig. 6—Block diagram of echo canceller LSI.

the transmitted frame, consisting of 0 pulses followed by a 1 pulse, are synchronized with those of the received frame pulses. The 0s cover the FP/TP reception period of the received frame. A 14-bit blank period precedes FP to avoid the influence of the echo tail of the previous frame. With this frame format, the timing extraction circuit is free from the influence of echo signals and stable timing extraction can be obtained.

However, this kind of frame arrangement is not necessary at the ET in the switching office. Because the ET has a master clock which governs the complete systems, it is sufficient to shift the phase of the master clock to attain the clock for the decision and the echo cancellation in accordance with the round-trip delay of the subscriber loop. Owing to line equalization and echo cancellation in the analog domain, a sufficient marginal eye opening on the time axis makes the system resilient to phase shift due to drifting of the round-trip delay. The adjustment is done during the initial training period using a DPLL circuit.

The line bit rate is set depending on the frame repetition cycle and the capacity of CO/ST. The authors used a 160 kbit/s line bit rate, whose frame structure is shown in Fig. 5. This contains 144 kbit/s 2B + D channels of the CCITT I-430 standard format and a 4 kbit/s CO/ST channel. The frame repetition cycle is 2 ms. For the 96 kbit/s line bit rate, which is expected to enable a longer reach, the infor-

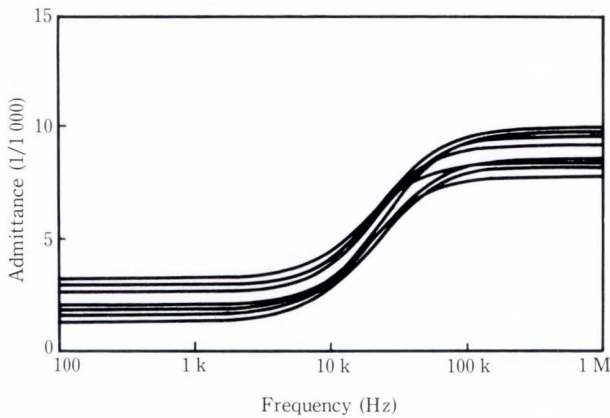


Fig. 7—Admittance characteristics of balancing networks.

mation capacity decreases to 80 kbit/s for the B + D channels and the capacity of CO/ST can be set to 7 kbit/s.

5. Circuit configuration

Figure 6 is a block diagram of the EC LSI. The LSI provides functions such as unipolar to bipolar (AMI code) signal conversion in the transmitter, and echo cancellation and the 3R functions (reshaping, retiming and regenerating) in the receiver.

Data to be transmitted is framed and converted to bipolar pulses (U/B) and sent to the line driver (DRIV). The echo leakage is suppressed by the hybrid transformer (HYB). The automatically controlled balancing network circuit (BN) reduces echoes as much as possible¹¹⁾. The two-stage echo canceller consists of a first-stage echo canceller (EC 1) and a second-stage echo canceller (EC 2)¹¹⁾. The \sqrt{f} AGC equalizer (\sqrt{f} AGC EQL) compensates for the loss characteristics of the subscriber loop. The decision feedback equalizer (DFEQL) compensates for residual intersymbol interference and the echo caused by bridged taps¹⁴⁾. Timing extraction is achieved using a newly developed digital phase locked loop circuit (DPLL)¹³⁾. In the following sections, the key techniques are described in detail.

5.1 Automatically controlled balancing network circuit

The purpose of this circuit is to suppress the

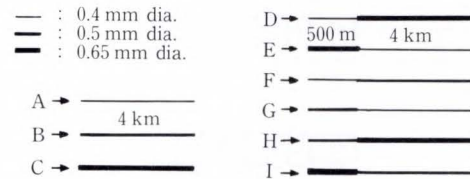
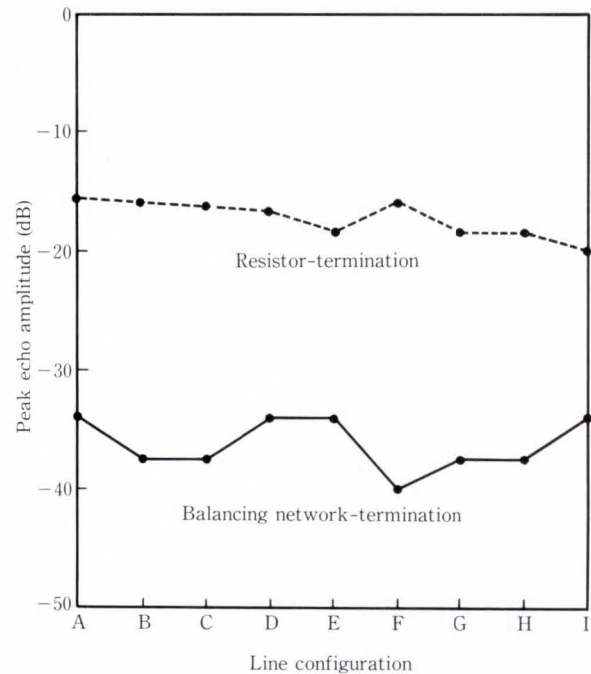


Fig. 8—Echo suppressing characteristics.

echo leakage from the transmitter to the receiver by matching the line impedance and balancing network impedance as closely as possible.

It was confirmed experimentally that eight impedance characteristics were enough to suppress the peak amplitude of the echo up to over 30 dB for the wide range of the line configurations. Figure 7 shows the admittance characteristics of eight balancing networks. The echo suppressing characteristics by the eight balancing network circuits for various line configurations are shown in Fig. 8. As can be seen in this figure, an improvement of more than 18 dB over a simple resistor termination is obtained.

Figure 9 shows the structure of the automatically controlled balancing network circuit. Taking account of manufacturing fluctuation in the CMOS process, two resistor networks, each consisting of eight resistors, were prepared on the LSI chip to approximate various line

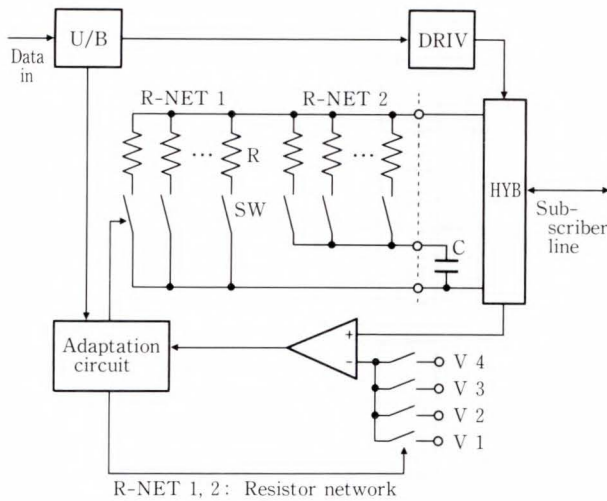


Fig. 9—Block diagram of automatic balancing network.

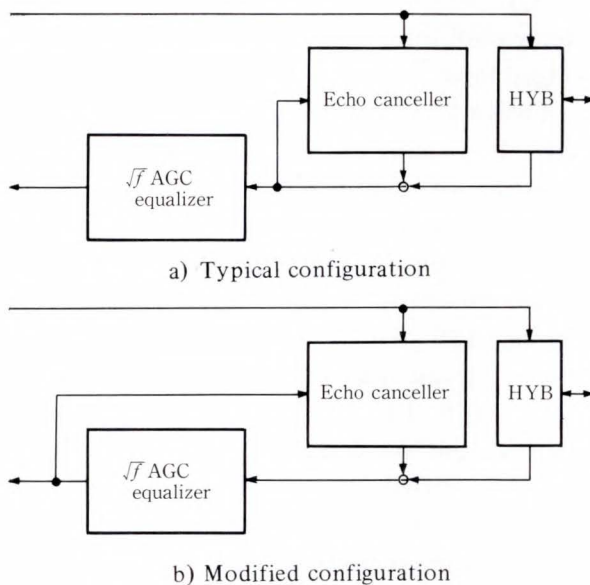


Fig. 10—Echo canceller configurations.

conditions. The optimum combination of two resistors, one from each network, is chosen by detecting the echo peak during the initial training procedure. The convergence algorithm is as follows. The reference level of the comparator (COMP) is first switched to the lowest level, V 1. The echo peak is compared to the reference level each time a combination of two resistors, one from each network, is selected. When the echo peak is lower than the reference level, that combination is chosen. If the echo peak exceeds the reference level for all combinations of two

resistors, the next higher level, V 2, is chosen as the reference level. The procedure is repeated until an echo peak lower than the reference level is detected. Convergence is quick because the comparison need be made only 64 times for each reference level. Only one capacitor is necessary outside the LSI.

5.2 Two-stage echo canceller

Figure 10-a) shows a typical hybrid transmission system configuration with an echo canceller. In this configuration, the echo canceller suffers from the following problems.

- 1) High-precision amplitude and dense time axis echo cancellation are required.
- 2) Even if a satisfactory echo cancellation is obtained at the sampling point, a residual echo may exist away from the sampling point. This will cause unacceptable eye closure at the decision point due to the filtering characteristics of the \sqrt{f} equalizer.

The second problem can be solved by the detecting error signal at the output of the \sqrt{f} equalizer, shown in Fig. 10-b), for adaptation of the echo canceller. This configuration, however, introduces the problem of instability or the need for a very sophisticated algorithm for adaptation, since each tap coefficient for echo cancellation becomes correlated due to the filtering of the \sqrt{f} equalizer. These problems can be solved by using an echo canceller with a two-stage structure, which was introduced in the authors' system.

Figure 11 is a block diagram of the two-stage echo canceller. Both the first stage echo canceller (EC 1) and the second stage echo canceller (EC 2) use a table look-up method. EC 1 operates on a high-speed sampling clock (four times the baud-rate) with a coarse quantization step size which aims to prevent signal saturation in the \sqrt{f} AGC EQL. EC 2 compensates for the residual echo due to the coarse quantization step size of the EC 1 and the filtering effect of the \sqrt{f} AGC EQL at the decision points. EC 2 operates on a baud-rate sampling clock with a fine quantization step size.

Considering the various line configurations

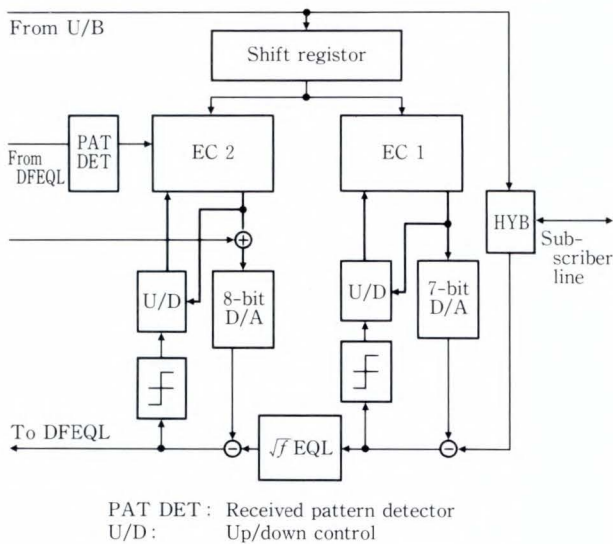


Fig. 11—Block diagram of two-stage echo canceller.

including mixed gauges and bridged taps, EC 1 covers 5 baud-rate intervals with 20 taps and EC 2 covers 8 baud-rate intervals with 8 taps, the first five of which overlap with the EC 1.

By adopting the two-stage structure, it was found that 7-bit precision was sufficient for the D/A converter of EC 1 and 8-bit precision for EC 2, one bit being for overflow protection since this D/A converter has to represent the added value of the echo replica and DFEQL signal.

After the initial convergence using the training procedure, only EC 2 enters the adaptive operation mode. In this mode, the tap adaptation is carried out when the all the 0 patterns are detected in the received data train. The echo replica is updated if the error signal is detected having the same polarity eight consecutive times for each corresponding transmitted pulse pattern. This procedure enables the stable adaptation of EC 2 and the echo replica catches up with the characteristic changes of the transmission line with a long time constant.

5.3 Line equalizers

Two types of line equalizers are built into the EC LSI chip. One is the \sqrt{f} AGC EQL which compensates for subscriber loop loss up to 50 dB at the Nyquist frequency. The other is the

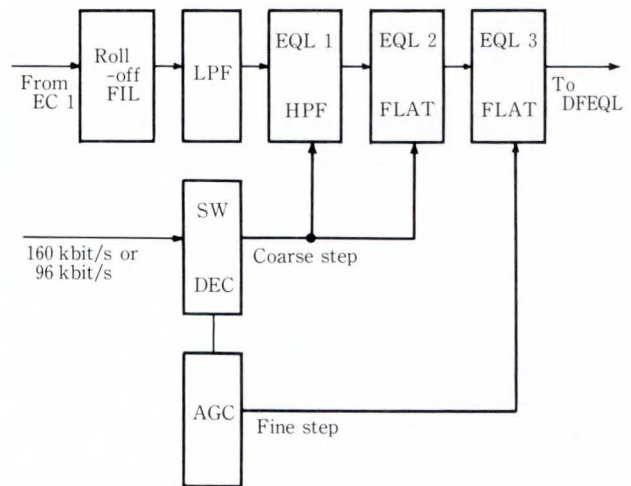
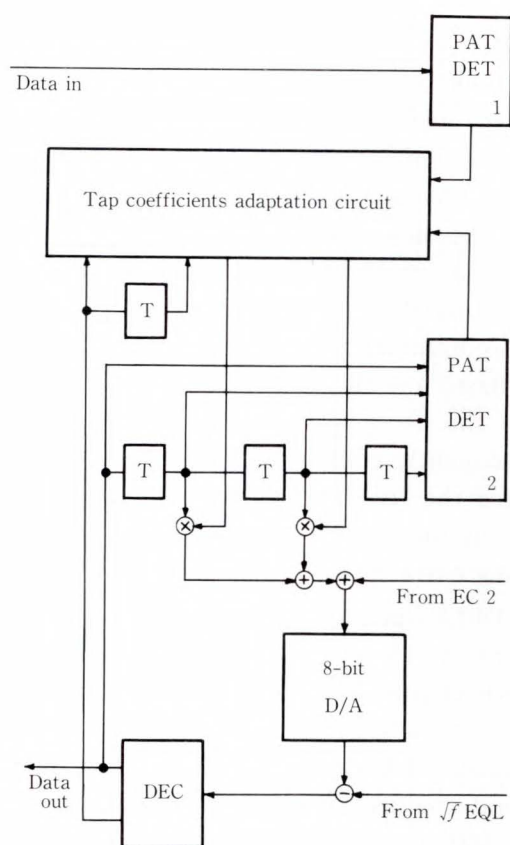


Fig. 12—Block diagram of \sqrt{f} AGC equalizer.

DFEQL which compensates for the residual intersymbol interference and the echo caused by bridged taps^{14), 15)}.

Figure 12 is a block diagram of the \sqrt{f} AGC EQL. It is constructed using analog circuits consisting of two variable-gain flat amplifiers (EQL 2, EQL 3), a high-pass filter with variable cutoff frequency (EQL 1), a low-pass filter (LPF), a roll-off filter (ROLL OFF FIL), a switch decoder (SW DEC) and an automatic gain control circuit (AGC). Two filters, LPF and ROLL OFF FIL, located at the front end, suppress the out-band-signal components and release the signal from the amplitude saturation at the high-pass filter section. The equalizer EQL 1 compensates for the \sqrt{f} loss characteristics. This is also an effective means of shortening the echo tail. The \sqrt{f} AGC EQL is designed to be used with two transmission bit rates (160 kbit/s or 96 kbit/s). The optimum combinations of variable flat gain of EQL 2 and slope gain of EQL 1 corresponding to the loop loss characteristics are memorized in the on-chip ROM. The desired transmission bit rate can be chosen by pin-programming the LSI.

Figure 13 is a block diagram of the DFEQL with two taps. The DFEQL operates on a baud-rate sampling clock. Tap coefficients are automatically trained during the first training period. After the convergence of the tap coefficients it is sufficient to update them with



PAT DET 1: Transmit pattern detector
 PAT DET 2: Received pattern detector
 DEC : Decision circuit

Fig. 13—Block diagram of decision feedback equalizer.

a very long time constant, so the adaptation of the tap coefficients is carried out when the isolated pulse pattern (0100) in the received data train and the all 0 pattern in the transmitted data train are detected at the same time, thus avoiding the interaction between EC 2 and DFEQL. The DFEQL shares an 8-bit D/A converter with the EC 2.

5.4 Timing extraction circuit

A new DPLL circuit was developed to improve the jitter characteristics of the regenerated clock.

Jitter has the following causes:

- 1) Pattern jitter
Due to intersymbol interference.
- 2) Idling jitter
Due to the control mechanism of the DPLL,

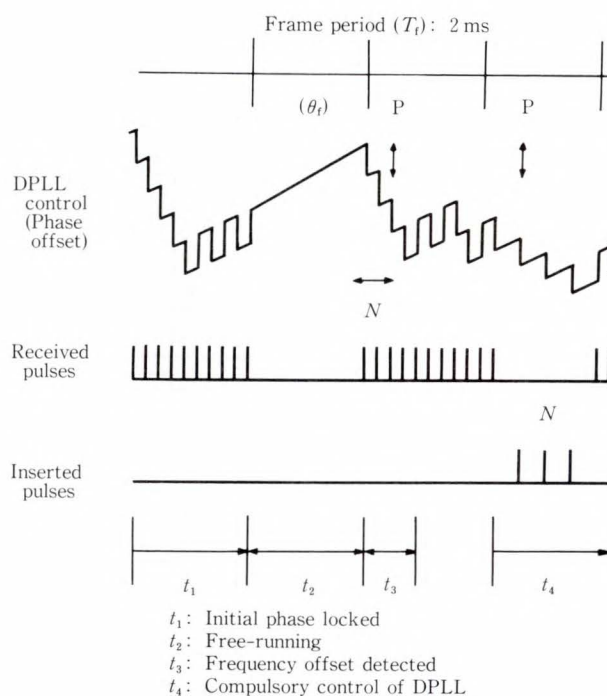


Fig. 14—DPLL control.

which is estimated to be the ratio of the baud rate to the master clock frequency.

3) Free-running jitter

Due to the frequency offset between the master clock frequency of the ET and that of the NT.

In this method, the clock signal is extracted only from the fixed pulse pattern (FP/TP). Therefore, the pattern jitter due to intersymbol interference is negligible. Since the master clock frequency is set to 15.36 MHz for a baud-rate of 160 kbit/s, the idling jitter width is estimated to be between one and two percent. The main jitter factor is the free-running jitter. The authors' proposed DPLL control method achieves stable timing extraction even when the frequency offset is more than ± 100 ppm between the ET and the NT. This is realized by measuring the frequency offset during the initial training period, and assigning the insertion/drop control timing whose frequency is a function of the measured frequency offset. The timing phase jumps caused by the insertion/drop control of the DPLL may cause a slight degradation of the echo canceller performance, but it is found that the total system performance is barely influ-

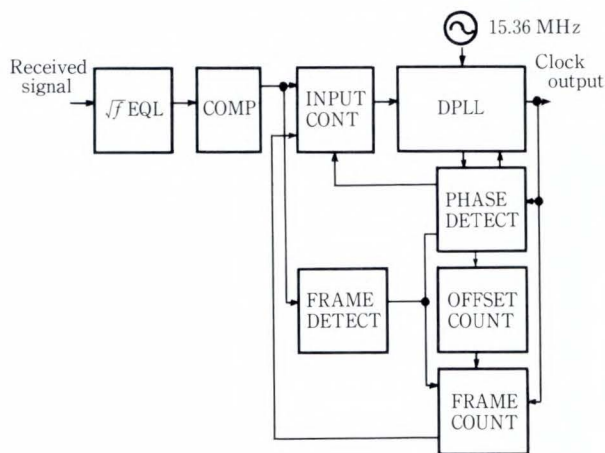


Fig. 15—Block diagram of timing extraction circuit.

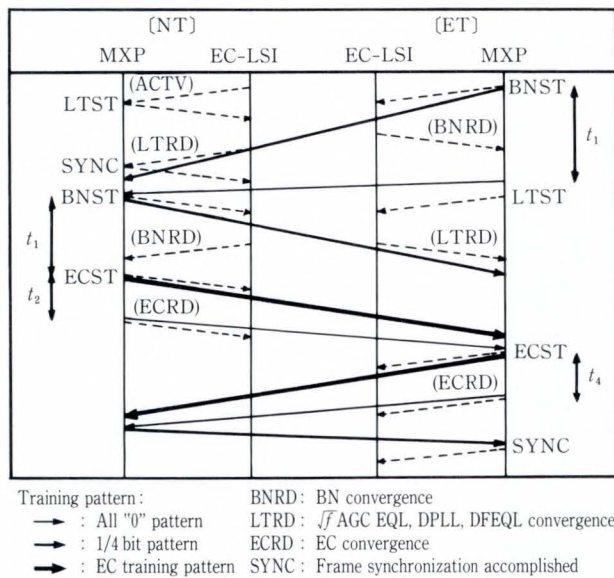


Fig. 16—Initial training procedure.

enced by such timing phase jumps.

Figure 14 is a schematic diagram of the DPLL training procedure.

1) Initial convergence period (t_1)

After the line equalizer converges, the DPLL is phase-locked to the pulses received from the far end.

2) Free-running period (t_2)

After the DPLL is phase-locked, the input of the received pulses to the DPLL is inhibited for one frame period (T_f). The DPLL goes into free-running operation during this period and the phase difference (θ_f) appears due to the frequency offset.

3) Detection of the frequency offset (t_3)

After free-running, the DPLL is again phase-locked, and during this period the number of received input pulses that needed to be phase-locked (N) is counted, which can be regarded as the frequency offset between the ET and the NT per frame. The direction of control (drop/insertion) (P) is also memorized.

4) Compulsory control of the DPLL (t_4)

Based on the results of P and N obtained with the above procedure, the DPLL must be subsequently controlled N times for each frame during the free-running period. As a result, the free-running jitter is suppressed. During the timing extraction period using the FP/TP pulses, the DPLL operates normally.

Figure 15 is a block diagram of the new DPLL circuit. The following circuits have been added to a standard DPLL circuit. The frame detector (FRAME DETECT) sets the frame period before frame synchronization is accomplished. The input controller (INPUT CONT) allows only timing pulses (TP) and compulsory pulses to pass through to the DPLL. The phase detector (PHASE DETECT) detects the convergence of the DPLL and also memorizes the direction of the drop/insertion control. The offset counter (OFFSET COUNT) detects the frequency offset. Based on the output of the OFFSET COUNT, the frame counter (FRAME COUNT) sets the timing of compulsory control of the DPLL by dividing the frame period into N equal intervals.

5.5 Activation procedure

To ensure quick and stable convergence, an initial training procedure for each functional block, such as BN, \sqrt{f} AGC EQ, DFEQL, DPLL and EC, is provided. Figure 16 shows the initial training procedure for the EC LSI when an activation request arises from the ET side.

The procedure starts when the signal power is detected. The equalizers, \sqrt{f} AGC EQ, DPLL and DFEQL, are trained in that order using the training pattern (1/4-bit pattern: repeated pattern of a 1 pulse followed by three 0 pulses). At the same time the optimal balancing network

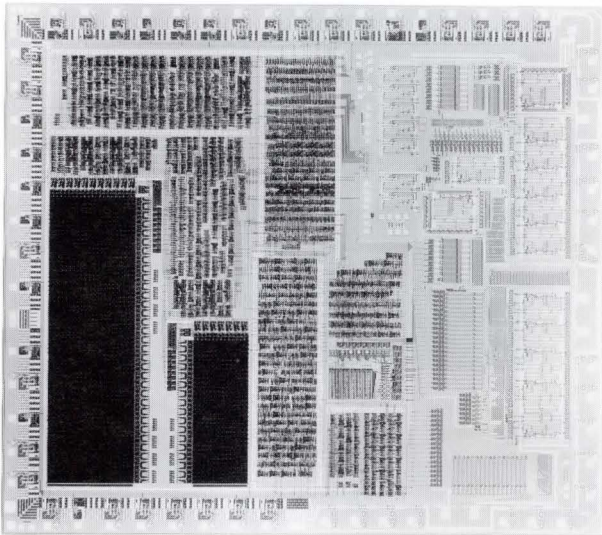


Fig. 17—Microphotograph of the EC chip.

characteristic is chosen. Following this sequence, EC 1 and EC 2 are trained with the training time for EC 2 being a little longer than that for EC 1 using the special training pattern which contains every combination of 8-bit patterns. To keep the timing clock phase correct, the specially arranged frame format is used in the training period. Four timers, t_1 to t_4 , are used to control the sequence, and are set up by a built-in MXP timer.

6. EC LSI

All the functional blocks mentioned above were implemented on the single-chip EC LSI. Figure 17 is a microphotograph of the EC chip. The LSI was designed using an analog/digital CMOS process¹⁶⁾. Table 2 also lists the specifications of the EC chip.

The 8-mm \times 9-mm chip was designed including 4 500 basic cells, a ROM (32 W \times 8 bits) and two RAMs (512 W \times 11 bits and 256 W \times 7 bits) in the digital section with operational amplifiers, comparators, capacitors, resistors, and two D/A converters in the analog section. The block layout was done by separating both sections with power supply lines and a test circuit to avoid interference between the analog and digital parts.

Data transfer between the analog and digital sections is through the test switching circuit,

Table 2. Chip specifications

Physical	
Channel length	2.3 μ m
Chip size	8 mm \times 9 mm
Package	RIT-64
Organization	
Random gate scale	4 500 basic cells
Operational amplifier	12
Comparator	7
ROM	1 (32 W \times 8 bits)
RAM	2 (512 W \times 11 bits) (256 W \times 7 bits)
D/A converter	2 (7 bits, 8 bits)
Others	Resistor, and capacitor
Operational	
Supply voltage	5 V
Power dissipation	150 mW

which enables these sections to be tested independently. When the digital section is tested, all I/O signals are routed to the tester which generates pseudo I/O signals. During the dc test of the analog section, digital control data is directly applied from outside through the test switching circuit and every amplifier, comparator, D/A converter, and \sqrt{f} EQ are tested. The EC LSI also features an initial training control circuit which generates the initial training sequence of each functional block by receiving training patterns from the multiplexing processor LSI.

7. Performance characteristics

The total DSL system was installed and evaluated in terms of eye openings, eye diagrams, jitter characteristics, sinusoidal crosstalk margin, and activation time. It was tuned to a line bit rate of 160 kbit/s.

To evaluate the performance of all equalizers, eye openings were measured by changing the lengths of the 0.5 mm diameter cable. The results are shown in Fig. 18. The bottom line is without echo cancellation. For the middle line, only EC 1 is operating. The top line is when the two stage echo canceller operates. It can be seen that impaired eye openings due to residual echoes are restored by EC 2, especially for long cable lengths, and consequently good eye

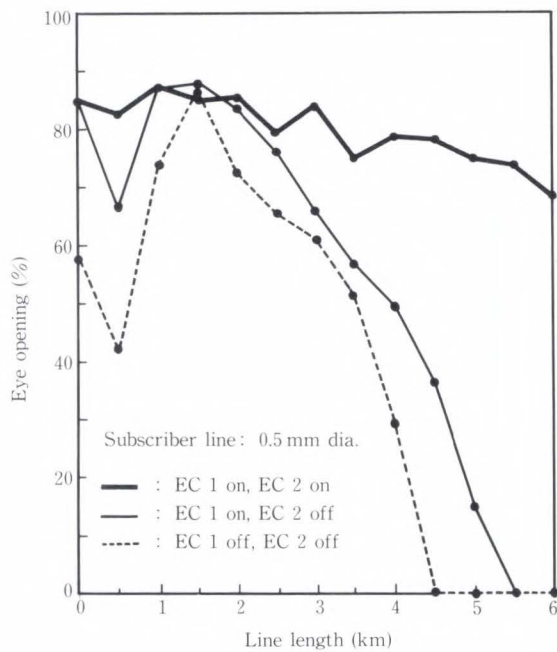


Fig. 18—Eye openings.

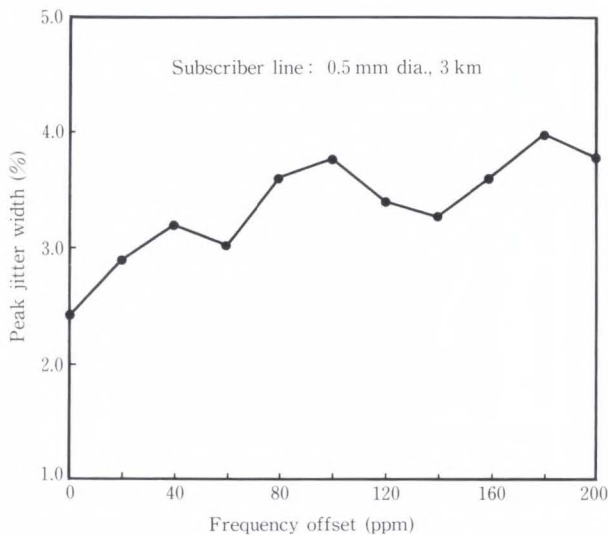


Fig. 20—Jitter characteristics.

openings of more than 70 percent can be obtained.

Figure 19 shows example eye diagrams at the output of the DFEQL of the NT side. The diagram in Fig. 19-a) was obtained by connecting the NT and the ET through a 6-km cable of 0.5-mm diameter with an attenuation of 45 dB at 80 kHz. The diagram in Fig. 19-b) represents the case when two bridged taps are added to a 4.5-km cable, with a total attenuation of 47 dB

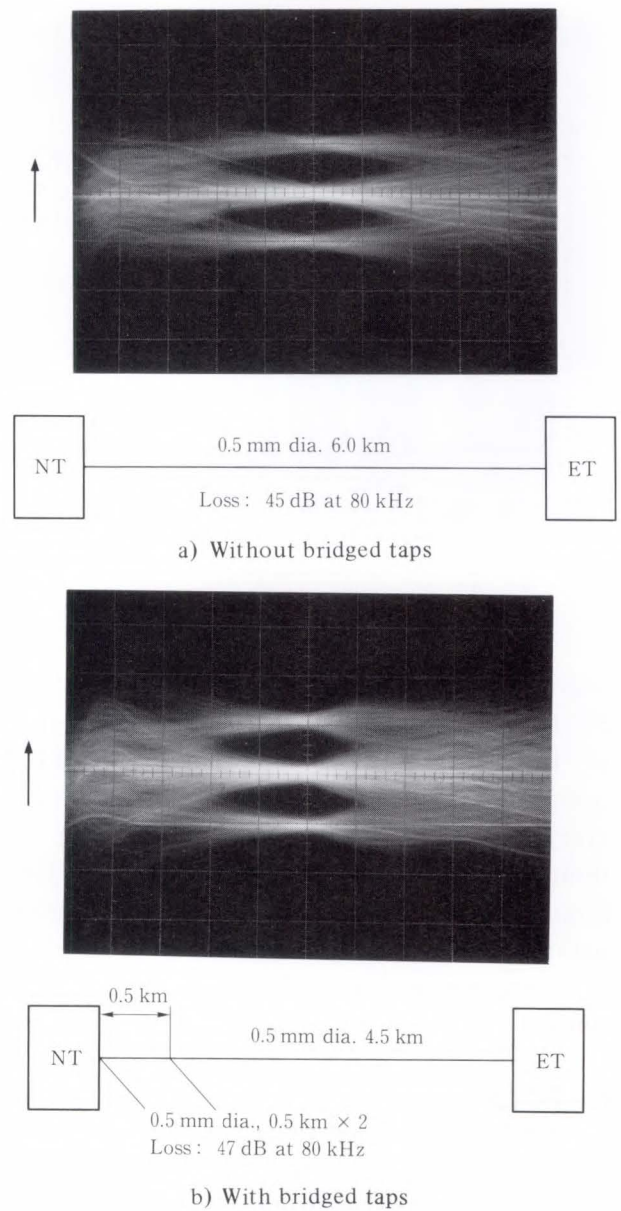


Fig. 19—Eye diagrams.

at 80 kHz. In both cases clear eye openings are obtained at the decision point.

The jitter characteristics of the extracted clock were measured with different frequency offsets between the NT and the ET. The results are shown in Fig. 20. This was measured without a high-pass filter, which is a more severe test condition for jitter measurement, but still meets the five percent peak to peak requirement.

To evaluate the noise margin, the error rate was measured in the presence of sine wave interference with an amplitude X . The results are shown in Fig. 21. In this measurement, the

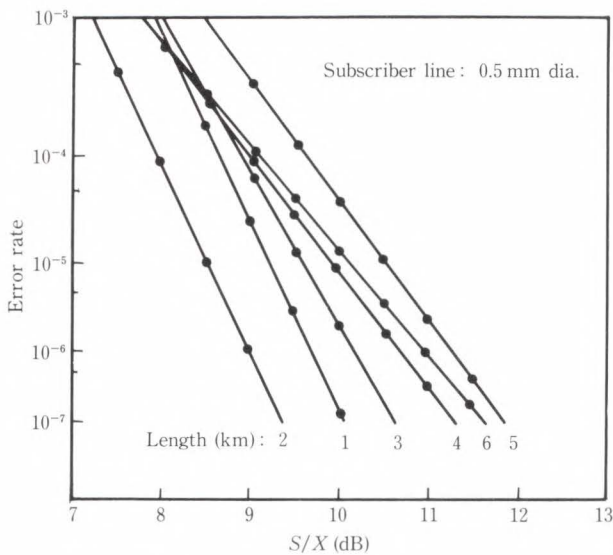


Fig. 21—Error-rate characteristics by equalizing waveform marginal checking.

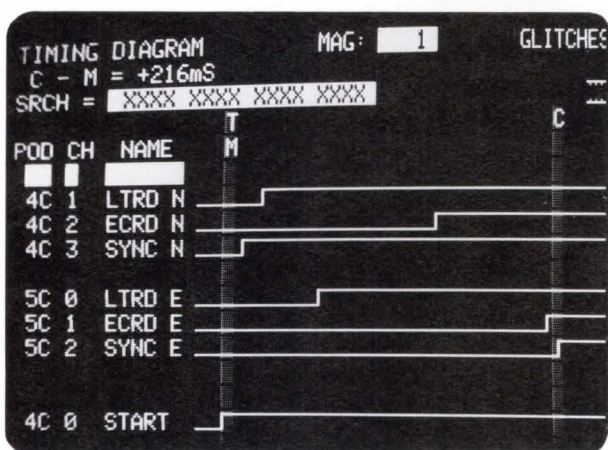


Fig. 22—Activation time.

cable lengths were changed from 1 km to 6 km and frequency offset was more than 30 ppm. A good S/X ratio of less than 12.7 dB at an error rate of 10^{-7} was obtained for a variety of loop lengths.

Figure 22 shows the measured activation time of the EC LSI. LTRD-N, ECRD-N, and SYNC-N indicate the convergence of the line equalizers including DPLL, that of EC, and the accomplishment of frame synchronization, respectively, at the NT side, while LTRD-E, ECRD-E, and SYNC-E indicate those of the ET side. The total activation time from start-up to

the establishment of bidirectional error free transmission was less than 220 ms.

8. Conclusion

This paper described an echo canceller LSI for ISDN subscriber loop transmission. A specially arranged time-compressed frame format combined with the use of a newly developed DPLL circuit provides excellent timing extraction performance. The approach requires only 8 bits precision for the D/A converter, which made the LSI implementation easier. As the EC LSI has been developed and combined with a processor LSI for multiplexing and circuit termination, it can perform basic DSL equipment functions. Experiments were carried out using a line transmission rate of 160 kbit/s and the AMI code. As a result, more than 6-km transmission on 0.5-mm twisted-pair cable was found to be possible.

9. Acknowledgement

The authors would like to express their gratitude to Dr. K. Murano of Fujitsu Laboratories Ltd., and Messrs. Y. Mochida, K. Ohta, H. Gambe, and M. Yamamoto of Fujitsu Limited for their invaluable guidance and encouragement, and Mr. Y. Hino of Fujitsu VLSI Limited for his outstanding work in LSI design.

References

- 1) Inoue, N., Komiya, R., and Inoue, Y.: Time-Shared Two-Wire Digital Subscriber Transmission System and Its Application to The Digital Telephone Set. *IEEE Trans. Commun.*, **COM-29**, 11, pp. 1565-1572 (Nov. 1981).
- 2) Agazzi, O., Hodges, D. A., and Messerschmit, D. G.: Large-Scale Integration of Hybrid-Method Digital Subscriber Loops. *IEEE Trans. Commun.*, **COM-30**, 9, pp. 2095-2108 (Sept. 1982).
- 3) Wouda, K. J., Tol, S. J. M., and Reijntjens, W. J. M.: An ISDN Transmission System with Adaptive Echo Cancelling and Decision Feedback Equalization - a Two Chip Realization. *IEEE ICC'84 Conf. Rec.*, pp. 685-690 (May 1984).
- 4) Gerwen, P. J. V., Verhoeckx, N. A. M., and Claasen, T. C. M.: Design Considerations for 144 kb/s Digital Transmission Unit for the Local Telephone

- Network. *IEEE J. Select. Areas Commun.*, **SAC-2**, 2, pp. 314-323 (March 1984).
- 5) Komiya, R., Yoshida, K., and Tamaki, N.: The Loop Coverage Comparison Between TCM and Echo Canceller Under Various Noise Considerations. *IEEE Trans. Commun.*, **COM-34**, 11, pp. 1058-1067 (Nov. 1986).
 - 6) Special Issue on Integrated Service Digital Network: Technology and Implementations - II. *IEEE J. Select. Areas Commun.*, **SAC-4**, 8, pp. 1281-1372 (Nov. 1986).
 - 7) Wouda, K. J., Tol, S. J. M., Zuidweg, P., and Reingruber, O.: Towards a Single Chip ISDN Transmission Unit. Proc. ISSLS'86 pp. 250-255 (Oct. 1986).
 - 8) Blake, R. B., Gottfried, N. L., Trivedi, B. J., and Zucker, W. F.: An ISDN 2B + D Basic Access Transmission System. Proc. ISSLS'86, pp. 256-260 (Oct. 1986).
 - 9) Adams, P. F., Cox, S. A., Carpenter, R. B. P., and Cole, N. G.: A Long Reach Digital Subscriber Loop Transceiver. IEEE GLOBECOM'86 Conf. Rec., pp. 39-43 (Nov. 1986).
 - 10) Mochida, Y., Ohta, K., and Moriya, T.: ISDN-Oriented Transmission Network. *FUJITSU Sci. Tech. J.*, **22**, 4, pp. 241-249 (Sept. 1986).
 - 11) Fukuda, M., Tsuda, T., and Murano, K.: Digital Subscriber Loop Transmission Using Echo Canceller and Balancing Networks. IEEE ICC'85 Conf. Rec., pp. 1181-1185 (June 1985).
 - 12) Murano, K., Kuwahara, H., Watanabe, T., Ohta, K., Gambe, H., Gotohda, T., and Takaoka, H.: A Processor VLSI for Multiplexing and Circuit Termination Functions - MUX Processor. IEEE ICC'86 Conf. Rec., pp. 1674-1678 (June 1986).
 - 13) Fukuda, M., Tsuda, T., Kaneko, K., Awata, Y., Hino, Y., and Takada, A.: An Echo Canceller LSI for ISDN Subscriber Loop Transmission. IEEE ICC'87 Conf. Rec., pp. 596-600 (June 1987).
 - 14) Chujo, T., Ueno, N., Takada, A., Hino, Y., and Fukuda, M.: A Line Termination Circuit for Burst-Mode Digital Subscriber Loop Transmission. *IEEE J. Select. Areas Commun.*, **SAC-4**, 1, pp. 176-183 (Jan. 1986).
 - 15) Ishikawa, M., Kimura, T., and Tamaki, N.: A CMOS Automatic Line Equalizer LSI Chip Using Active-RC Filtering. *IEEE J. Solid-State Circuits*, **SC-19**, 4, pp. 506-509 (Aug. 1984).
 - 16) Hino, Y., Chujo, T., Ueno, N., Fujita, K., Yamamoto, M., Yamaguchi, K., and Kikuchi, H.: A Burst-Mode LSI Equalizer with Analog-Digital Building Blocks. IEEE ISSCC'84 Conf. Rec., pp. 238-239 (Feb. 1984).



Toshitaka Tsuda

Computer Networks and Visual
Communication Laboratory
FUJITSU LABORATORIES,
KAWASAKI
Bachelor of Electrical Eng.
The University of Tokyo 1970
Dr. of Philosophy in Electrical Eng.
The University of Tokyo 1975
Specializing in Picture Coding, Digital
Signal Processing and Communication
LSI



Yutaka Awata

Development Dept.
FUJITSU DIGITAL TECHNOLOGY
LIMITED
Bachelor of Electronics Eng.
Ehime University 1982
Specializing in Communication LSI



Misao Fukuda

Communications Processing
Technology Laboratory
FUJITSU LABORATORIES,
KAWASAKI
Bachelor of Applied Physics
Waseda University 1978
Master of Applied Physics
Waseda University 1980
Specializing in Communication LSI

Interference from Digital QAM System to Analog FM System

• Yoshimasa Daido • Hiroshi Nakamura

(Manuscript received February 29, 1988)

Considering high-power transmission of high-capacity digital radio system such as a 256 QAM, this paper describes a method for determining the conditions under which a new digital system can be installed without disturbing the already existing analog FM systems. The ratio of the FM signal to interference level is calculated as a function of the channel separation between the FM and the digital systems, using various parameters such as bit rate, rolloff factor, and modulation level of the digital system. This paper also shows that spectrum shaping of the QAM system by cosine rolloff filter results in a more rapid decrease in the interference level for increase of the channel separation than that of the conventional PSK system using a 5-section Butterworth filter with BT of 1.2 as a transmit filter.

1. Introduction

Improvement of spectrum efficiency has been the most important task in field of microwave digital radio systems in for the last ten years. To this end, 16-QAM and 64-QAM digital radio systems have already been used in the field¹⁾⁻³⁾. Even 256-QAM systems have been developed and are now field-tested in Japan by NTT⁴⁾⁻⁶⁾.

However, a system with a higher level of modulation requires higher transmission power. For example, a 256-QAM system requires a transmission power eight times that needed by a 16-QAM system when the repeater spacing and bit rate are the same. The increased transmission power means that the system can strongly interfere with adjacent systems. Thus, to install a new multi-level QAM system, it is necessary to accurately estimate the conditions under which communication quality of surrounding systems are not degraded.

Since many analog FM systems have been installed nearly everywhere, this paper estimates degradation of their communication quality caused by installation of the multi-level QAM system. Though interference between the analog

FM systems and digital PSK systems has been estimated^{7),8)}, spectral shaping of the multi-level QAM system differs from that of the conventional PSK system cited in reference 7. As this paper will indicate, the difference between the PSK and the QAM system is considerable. Thus, spectral shaping using a cosine rolloff filter is assumed in this paper.

Spectrum of the analog FM signal is required in the estimation mentioned above. A considerable number of papers⁹⁾⁻¹¹⁾ were published in early 1970 to give analytic expression of the FM spectrum. Of these papers, reference 9 has given a rigorous autocorrelation function of the FM signal. Authors have expanded the autocorrelation function into a Taylor series to give an analytic expression of the FM spectrum. However this expansion has made mathematical procedure rather complex. On the other hand, computer simulations^{7),8)} of the FM spectrum have also been reported, and computer simulation has a simpler mathematical procedure than those of references 9 to 11. However, computer simulations are time consuming. This paper adopts an intermediate method between the computer simulation and the analytic approach:

Equation (12) of reference 9 is numerically estimated to simplify the mathematical procedure. Since the computation time of computers has substantially decreased recently, the FACOM M-380 high-speed digital computer is able to give the FM spectrum with 400 sampling points in frequency within just 4 s.

This paper is composed of 5 chapters. Chapter 1 is the introduction. Chapter 2 describes the calculation method of interference from the digital QAM system to the analog FM system and has three sections. Section 2.1 gives the autocorrelation function of the analog FM signal, Sec. 2.2 gives the spectrum of the FM signal, and Sec. 2.3 gives the signal to interference noise ratio (SIR) of each FM channel. The calculated results of the interference are given in Chap. 3. Chapter 3 has two sections. Section 3.1 gives the calculated FM spectra, and Sec. 3.2 shows the dependence of signal to interference noise ratio on channel separation between digital QAM and FM systems. Comparison of the dependence for various system parameters such as bit rate, is also given. After the conclusion in Chap. 4, an appendix is given in Chap. 5 to supplement the mathematical procedure of Sec. 2.1.

2. Calculation method of interference from digital QAM system to analog FM system

2.1 Autocorrelation function of the analog FM signal

As described in the introduction, the estimation of interference requires spectrum of the analog FM signal. Since the spectrum is given by an inverse Fourier transformation of the autocorrelation function, its analytic expression given by Rowe et al.⁹⁾ is briefly reviewed in this section.

Figure 1 is a block diagram of an analog FM modulator. The data source of this figure gives a signal whose statistical properties are the

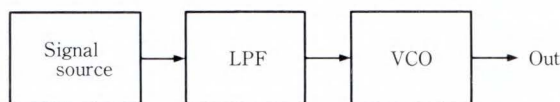


Fig. 1—Block diagram of FM modulator.

same as those of a white Gaussian random variable. Since a low-pass filter (LPF) eliminates the higher frequency components, the output signal of the LPF accurately represents the actual baseband signal.

When pre-emphasis¹²⁾ is applied to the baseband signal, the amplitude transfer function of the LPF is given by the following equation.

$$H(\omega) = \begin{cases} (10)^{1/4} [\{ 5.25 (\omega_r \omega)^2 + (\omega_r^2 - \omega^2)^2 \} / \{ 5.25 (\omega_r \omega)^2 + 7.9 (\omega_r^2 - \omega^2)^2 \}]^{1/2} \cdot (\omega_1 < |\omega| < \omega_{max}) \\ 0 (|\omega| < \omega_1 \text{ or } |\omega| > \omega_{max}), \end{cases} \dots \dots \dots (1)$$

where ω_{max} and ω_1 are the maximum and minimum angular frequency of the baseband signal, respectively. The resonant angular frequency ω_r is related to the maximum baseband frequency by the following equation:

$$\omega_r = 1.25 \omega_{max} \dots \dots \dots (2)$$

When pre-emphasis is not applied, $H(\omega)$ is unity for frequencies lower than the maximum baseband frequency. The output signal of the LPF is fed to a voltage controlled oscillator (VCO) whose oscillation frequency deviates from free running frequency proportionally to the input signal voltage.

The output signal $v_1(t)$ of the LPF is related to the output signal of the data source $v_0(t)$ as follows:

$$v_1(t) = \int_{-\infty}^{+\infty} h(t, u) v_0(u) du, \dots (3)$$

where $h(t, u)$ is the impulse response of the LPF and is given by

$$h(t, u) = \frac{1}{2\pi} \int_{-\infty}^{+\infty} H(\omega) \exp\{j\omega(t-u)\} \cdot d\omega \dots \dots \dots (4)$$

Since $v_1(t)$ is the input signal of the VCO, its output signal $v_2(t)$ is expressed as

$$v_2(t) = V_0 \exp \left\{ jk \int_{-\infty}^t v_1(u) du \right\}, \dots \dots \dots (5)$$

where k is the constant representing frequency deviation of the VCO. In this expression, the carrier component $\exp(j\omega_c t)$ is omitted for

simplicity of notation. The autocorrelation function $R(\tau)$ of $v_2(t)$ is given from its definition¹³⁾,

$$R(\tau) = \{ v_2(t+\tau) v_2^*(t) \} \\ = V_0^2 [\exp \{ jk \int_t^{t+\tau} v_1(u) du \}], \dots (6)$$

where $\{ \dots \}$ means the ensemble average of all possible values of $v_2(t)$ and $*$ means complex conjugate. Substituting Equation (3) into Equation (6) gives

$$R(\tau) = V_0^2 [\exp \{ jk \int_{-\infty}^{+\infty} v_0(u) \cdot f(t, \tau, u) du \}], \dots (7)$$

where the order of integration is changed and $f(t, \tau, u)$ is given by

$$f(t, \tau, u) = \int_t^{t+\tau} h(x, u) dx \dots (8)$$

The ensemble average of Equation (7) is calculated by considering white Gaussian nature of $v_0(t)$ and gives the autocorrelation function⁹⁾,

$$R(\tau) = V_0^2 \exp [-k^2 p \int_{-\omega_{\max}}^{+\omega_{\max}} \{ H(\omega) \}^2 \cdot (1 - \cos \omega \tau) / \omega^2 \times d\omega], \dots (9)$$

where p is the baseband signal power within one hertz. Derivation of Equation (9) from Equation (7) is given in the appendix. The argument of the exponential function in Equation (9) is directly estimated with numerical integration.

2.2 Power spectrum of analog FM signal

As is well known, the power spectrum is obtained by Fourier transformation of the autocorrelation function¹⁴⁾. Thus, the power spectrum density $P(\omega)$ of the FM signal is

$$P(\omega) = V_0^2 \int_{-\infty}^{+\infty} \exp(j\omega\tau) \cdot \exp [-k^2 p \int_{-\omega_{\max}}^{+\omega_{\max}} \{ H(\lambda) \}^2 \cdot (1 - \cos \lambda \tau) / \lambda^2 d\lambda] d\tau \dots (10)$$

The total transmission power of the FM signal is obtained by integrating Equation (10) with respect to ω ,

$$\int_{-\infty}^{+\infty} P(\omega) d\omega = 2\pi V_0^2, \dots (11)$$

where the following integral expression of the

Dirac delta function is used in the derivation of Equation (11):

$$\int_{-\infty}^{+\infty} \exp(j\omega\tau) d\omega = 2\pi \delta(\tau) \dots (12)$$

Thus, the normalized FM spectrum $P_{\text{FM}}(\omega)$ is obtained by dividing equation (10) by $2\pi V_0^2$:

$$P_{\text{FM}}(\omega) = 1/2\pi \int_{-\infty}^{+\infty} \exp(j\omega\tau) \cdot \exp [-k^2 p \int_{-\omega_{\max}}^{+\omega_{\max}} \{ H(\lambda) \}^2 \cdot (1 - \cos \lambda \tau) / \lambda^2 d\lambda] d\tau \dots (13)$$

Since the carrier component is eliminated, the angular frequency represents the deviation from the carrier.

In experiments, the power given to each channel is usually used instead of spectral power density. It may be reasonable to give the FM spectrum which can be compared with the experimental model, although this comparison is not made here. The power for a channel is obtained by integrating Equation (13) within the channel bandwidth B :

$$P_c(\omega) = B \int_{-\infty}^{+\infty} \exp(j\omega\tau) \cdot \{ \sin(\pi B \tau) / \pi B \tau \} \cdot \exp [-k^2 p \int_{-\omega_{\max}}^{+\omega_{\max}} \{ H(\lambda) \}^2 \cdot (1 - \cos \lambda \tau) / \lambda^2 d\lambda] d\tau \dots (14)$$

The power spectrum given by Equation (14) depends on parameters k and p . Since pre-emphasis does not influence the total baseband power, the baseband power density p is given by the total baseband power P_{in} and bandwidth,

$$p = \frac{P_{\text{in}}}{(\omega_{\max} - \omega_1)} \dots (15)$$

The modulation sensitivity k is usually expressed in terms of the frequency deviation f_v corresponding to unit input power P_0 of the FM modulator:

$$k = \frac{2\pi f_v}{(2P_0)^{1/2}} \dots (16)$$

2.3 Interference from digital QAM system to analog FM system

This section discusses the quality of demodulated FM signal. A signal to noise ratio (SNR) high enough to give good communication quality is assumed when there is no interference

from the digital QAM system. Considering the interference from the digital system as noise, signal to interference noise ratio (SIR) is defined as a power ratio of the FM wave to the interfering wave. An equation giving the SIR is already given by Stojanovic et al.¹⁵⁾, i.e.,

$$S/I = (k^2 P_{in} / \omega_{max}) \cdot \eta (2\pi/\omega)^2 \cdot \left\{ \frac{H(\omega)}{\int_{-\infty}^{+\infty} P_c(\omega - \lambda) P_{DG}(\lambda) d\lambda} \right\}^2 \dots \dots \dots (17)$$

where $P_{DG}(\omega)$ is the power spectrum of interfering wave. The transmission power spectrum of the digital QAM signal is the same as the output power spectrum of transmit filter for white input spectrum. In this paper, it is assumed that filters are equally shared between the transmitter and receiver. In other words, amplitude transfer function of the transmit filter is assumed to be the square root of a cosine rolloff filter. The power spectrum of the interfering signal is normalized so that integration of the spectrum over frequency is unity, i.e.,

$$P_{DG}(\omega) = \begin{cases} T/(2\pi) (|f|/f_0 < 1 - \alpha) \\ \frac{T}{4\pi} \left[1 + \cos\pi \left\{ \frac{f - f_0(1 - \alpha)}{2\alpha f_0} \right\} \right] & (1 - \alpha < |f|/f_0 < 1 + \alpha) \\ 0 (|f|/f_0 > 1 + \alpha) \end{cases} \dots \dots \dots (18)$$

where T is the symbol period, α is the rolloff factor and f_0 is the Nyquist frequency $\{ f_0 = 1/(2T) \}$. Since normalization eliminates information of strength of the interference, the strength is considered in parameter η of Equation (17), which is the ratio of the total desired power to the total undesired power.

3. Calculated results of interference from QAM system to FM system

3.1 Spectra of FM transmitters

Figure 2 shows the power spectra of FM 960-channel signals. The solid curve shows the spectrum with pre-emphasis and the dashed

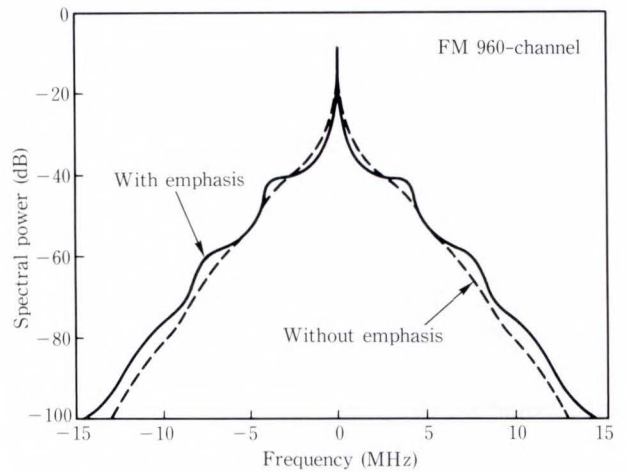


Fig. 2—Spectra of FM 960-channel transmitter. Frequency deviation of 200 kHz per 0 dBm input is assumed. Baseband signal is assumed to have the frequency range from 60 kHz to 4.188 MHz. Average power of -15 dBm is assumed for each baseband channel.

curve shows that without pre-emphasis. In this figure, a frequency deviation of 200 kHz per 0 dBm input power of the FM modulator is assumed. The input power level of the FM modulator is -15 dBm per channel. The minimum baseband frequency is 60 kHz and the maximum baseband frequency is 4.188 MHz. The horizontal axis represents the relative frequency to the carrier and the vertical axis represents the normalized power spectrum. Parameter B of Equation (14) is assumed to be 4 kHz.

Figure 3 shows the power spectra of FM 1800-channel signals. A frequency deviation of 140 kHz is assumed for 0 dBm input power of the FM modulator. The minimum baseband frequency is 312 kHz and the maximum baseband frequency is 8.204 MHz. The ratio of the minimum baseband frequency to the maximum is larger in the case of the 1800-channel than that of the 960 channel. The two dips on both sides of the carrier correspond to an absence of baseband signal near DC. These dips are also observed in the calculated spectrum shown in reference 11. A comparison of Figs. 2 and 3 shows that larger energy is concentrated on the carrier for the 1800-channel FM signal

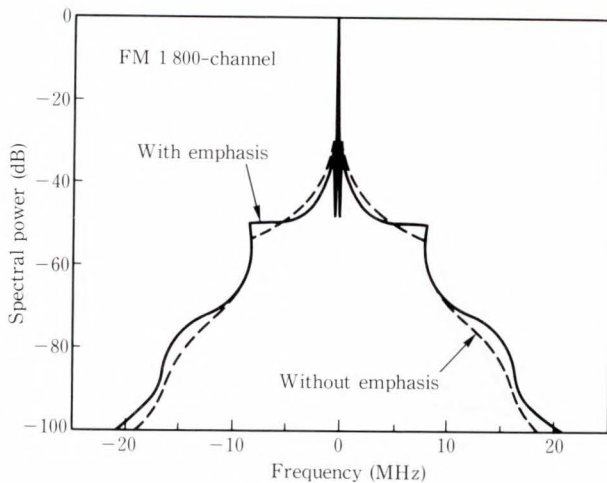


Fig. 3—Spectra of FM 1800-channel transmitter. Frequency deviation of 140 kHz per 0 dBm input is assumed. Baseband signal is assumed to have a frequency range from 312 kHz to 8.204 MHz.

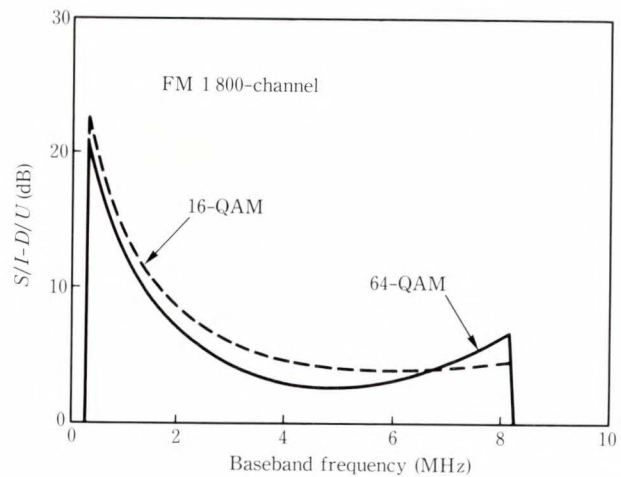


Fig. 4—Signal to interference noise ratio (SIR) of each channel. Both 16-QAM and 64-QAM digital systems have a bit rate of 90 Mbit/s and rolloff factor of 50 percent. The carrier of digital system is assumed to be located at the carrier of the FM 1800-channel system.

than the 960-channel FM signal.

3.2 Degradation of signal to noise ratio of FM signal caused by interference from digital QAM system

This section discusses the quality of the FM signal. SIR of the FM signal calculated by Equation (17) includes η , which is the power ratio of the desired FM signal to the undesired digital QAM signal (DUR). The ratio differs for each combination of the two systems. Since the ratio can easily be calculated, it may be convenient to subtract DUR from SIR.

The purpose for estimating the SIR is to determine the conditions under which all FM channels communicate with little interference. The first step in the estimation is to find the channel with the worst SIR. Figure 4 shows the SIR of the FM 1800 channel signals. The interference for the solid curve is given by a 64-QAM system, and that for the dashed curves is given by a 16-QAM system. In both cases, a bit rate of 90 Mbit/s is assumed. Since the baud rate is obtained by dividing the bit rate by information transmitted per symbol period, the baud rates of the 16-QAM and 64-QAM systems are 22.5 Mbaud and 15 Mbaud, respectively. In this figure, the carrier of the FM

system coincides with that of the digital system. A rolloff factor of 50 percent ($\alpha = 0.5$) is assumed for the digital system. As can be seen from the figure, the channel with the worst SIR differs from the top channel. This difference is also shown in reference 16 for interference between the FM systems.

Next, the SIR of the worst channel is estimated as a function of the channel separation between the digital and the FM system. The SIR is a function of the channel separation and depends on various system parameters such as channel number of the FM system and bit rate of the digital system. First, the dependence on the parameters of the digital system is examined, and then the dependence on the FM system will be estimated. The FM 960 channel signal is considered in Figs. 5 to 8.

As the first example, a comparison of the difference caused by spectrum shaping is shown in Fig. 5. In this figure, the rolloff factor is assumed to be 0.2 (20 percent). A 5-section Butterworth filter with BT of 1.2 is assumed for the dashed curve in accordance with that of reference 7. The same baud rate of 22.5 Mbaud is assumed to give almost the same 6 dB bandwidth. As can be seen from the figure, the dif-

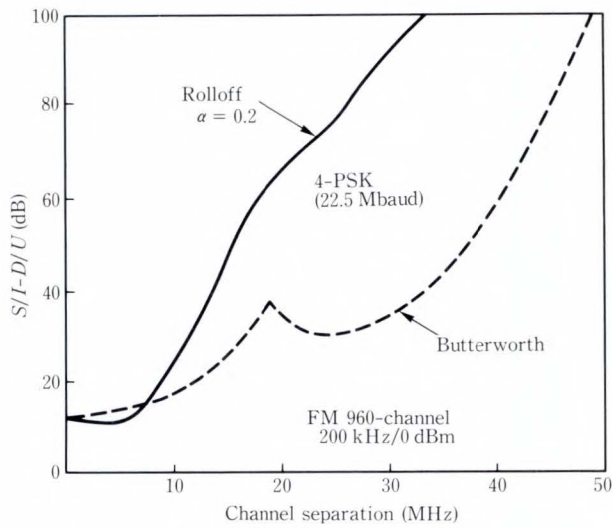


Fig. 5—Comparison of the worst channel SIR for different interference sources. Modulation is 4-PSK and the baud rate is 22.5 Mbaud. Solid curve corresponds to the spectrum shaping by a rolloff filter with a rolloff factor of 0.2 and dashed curve corresponds to that by a 5-section Butterworth filter with a BT product of 1.2.

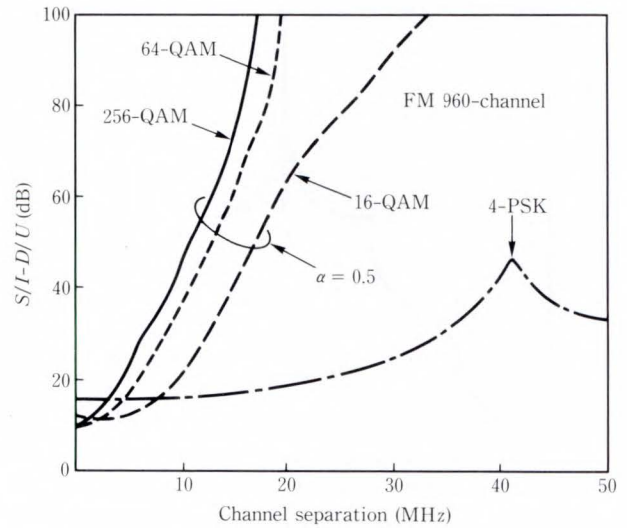


Fig. 7—Variation of the worst channel SIR for various modulation level of digital system. The same bit rate of 90 Mbit/s is assumed for all modulation levels from 4-PSK to 256-QAM. In the 4-PSK system, a 5-section Butterworth filter with a BT of 1.2 is assumed as spectrum shaping filter.

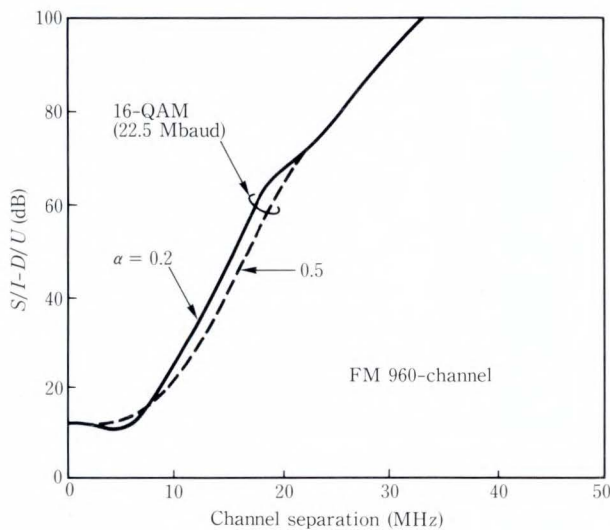


Fig. 6—Dependence of the worst channel SIR on rolloff factor of digital system.

ference between the two curves cannot be neglected. The difference is caused by the difference in spectrum shaping, as indicated in the introduction.

Since spectrum shaping depends on the roll-off factor, the dependence of the SIR of the

worst channel on the channel separation is estimated for 20 percent and 50 percent of rolloff factor. The two values can be regarded as upper and lower limits for the following reason. In the high capacity digital radio system, a rolloff factor larger than 50 percent is not suitable in practical use because of its lower spectral efficiency. However, a filter with a lower rolloff factor requires more accurate design and 20 percent can be considered as the lower limit attained by the present state of the art. As can be seen from the Fig. 6, the difference of the rolloff factor between 20 percent and 50 percent is much smaller than that between the Butterworth and rolloff. Since the difference of the rolloff factor between 50 percent and 20 percent is not large, the roll-off factor of 50 percent is used in the following calculation.

Next, the variation of the worst SIR by modulation level of the QAM system will be discussed. Hitherto, comparisons have been done under the same baud rate because our attention has been focused on the effect caused by difference in spectrum shaping. However, a higher level QAM system can transmit the

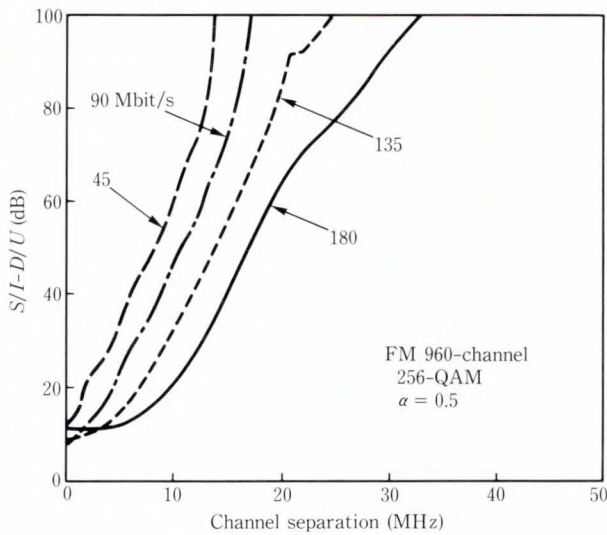


Fig. 8—The worst channel SIR vs. channel separation for various bit rates.

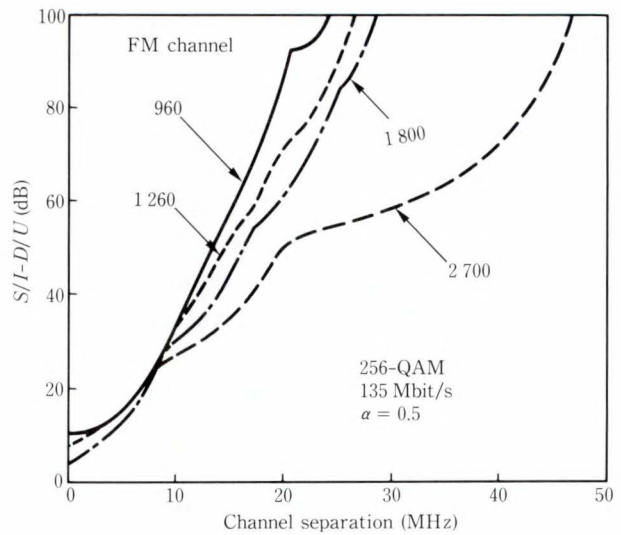


Fig. 9—Dependence of the worst channel SIR on channel number of FM system.

information in the same bit rate using a smaller bandwidth. The effect caused by bandwidth reduction should be considered. Figure 7 compares the worst SIR for different modulation level. The bit rate of 90 Mbit/s is assumed in this figure. This figure clearly shows that the QAM system with a higher modulation level can be installed with smaller channel separation than that with a lower modulation level.

Dependence of the SIR on bit rate of the 256 QAM system is shown in Fig. 8. As expected, larger channel separation is required for the system with a higher bit rate. The channel separation required for a specified system can be determined using this figure. When the channel separation is specified, this figure gives the maximum possible bit rate of the 256 QAM system.

Figure 9 shows the difference in the SIR for various channel numbers of the FM system. The 135-Mbit/s 256-QAM system with a rolloff factor of 50 percent is assumed as the interference source. The FM system with a larger channel number requires a larger channel separation, as shown in the figure.

Figures 5 to 9 determine the channel separation well enough to maintain good communication quality in the FM systems.

The required channel separation is determined by the following procedure:

- 1) Specifying the required SIR,
- 2) Calculating DUR, the ratio of the transmission power of two systems,
- 3) Subtracting the DUR from the required SIR and
- 4) Reading the channel separation where SIR is equal to the difference obtained by item 3) above.

4. Conclusion

Spectrum of analog FM signal was estimated by calculating autocorrelation function through numerical integration. Numerical integration gives rigorous results with a simplified mathematical procedure. The estimation method gives the FM spectrum within 4 s of computation time, with 400 sampling points of frequency.

The FM spectrum was used to estimate the interference from digital QAM systems to the FM system. Signal to interference noise ratio was estimated for each channel of the FM system. This calculation showed that the top channel is not always the worst channel.

Dependence of the worst signal to interference noise ratio on channel separation between the FM and the QAM system was

calculated to determine the channel separation with which the digital QAM system can be installed without disturbing the FM system.

These results are considered in estimating the feasibility of installing a digital QAM system in a channel adjacent to the FM system. After the possibility is confirmed, the method described in this paper gives useful information for selecting filters in the transmitter of the digital QAM system.

Since SNR of the FM signal will be degraded by fading, a reasonable value for the flat fade margin should be considered. In addition, nonlinearity of high power amplifier spreads the spectrum of the QAM system and increases the interference from the digital QAM system. An additional margin should be assumed besides the flat fade margin.

Though this paper does not describe the interference from the FM system to the digital QAM system, the FM spectrum of this paper can directly be used for estimating the interference.

Appendix

1. Calculation of statistical average of Equation (9)

Equation (7) can be rewritten in the form of summation according to the definition of an integral:

$$R(\tau) = V_0^2 \lim_{\Delta u \rightarrow 0} \left[\exp \left\{ jk \Delta u \sum_{n=-\infty}^{\infty} f \cdot (t, \tau, n \Delta u) v_0(n \Delta u) \right\} \right] \dots \dots \dots (A-1)$$

Since the argument of the exponential function is the summation, Equation (A-1) can be expressed as a product of the exponential functions. Input voltage $v_0(t)$ of the low-pass filter in Fig. 1 can be regarded as a white Gaussian random variable whose values sampled at different instants are statistically independent. The average of the product of statistically independent variables is equal to the product of the averages¹⁷⁾.

Thus, Equation (A-1) becomes

$$R(\tau) = V_0^2 \lim_{\Delta u \rightarrow 0} \prod_{n=-\infty}^{\infty} \left[\exp \left\{ jk \Delta u f \cdot (t, \tau, n \Delta u) v_0(n \Delta u) \right\} \right] \dots \dots \dots (A-2)$$

Here, the difference between discretely sampled values of $v_0(t)$ and the original continuous variable should be considered. Since uniform sampling is used in Equation (A-2), sampled values of $v_0(t)$ have spectral components between $-\pi/\Delta u$ and $\pi/\Delta u$. Thus, the total power of the sampled values is equal to $p(2\pi/\Delta u)$ where p is the spectral power density of the original $v_0(t)$,

$$\left[\int_{-\pi/\Delta u}^{\pi/\Delta u} |v_0(n \Delta u)|^2 \right] = p(2\pi/\Delta u) \dots \dots \dots (A-3)$$

The average power of the sampled value is equal to its variance. Since the Gaussian nature of variable $v_0(t)$ is assumed, the probability density function $P(v_0)$ of the sampled value is

$$P(v_0) = (\Delta u/4\pi p)^{1/2} \exp(-\Delta u v_0^2/4\pi p) \dots \dots \dots (A-4)$$

This probability density function is used to calculate the ensemble average of Equation (A-2):

$$\begin{aligned} &\langle \exp \left\{ jk \Delta u f(t, \tau, n \Delta u) v_0(n \Delta u) \right\} \rangle \\ &= \langle \int_{-\infty}^{+\infty} (\Delta u/4\pi p)^{1/2} \exp \left[\Delta u \cdot \right. \\ &\quad \left. \cdot \left\{ jk f(t, \tau, n \Delta u) v_0 - v_0^2/4\pi p \right\} dv_0 \right] \rangle \dots \dots \dots (A-5) \end{aligned}$$

Equation (A-6) can be rearranged as

$$\begin{aligned} &\langle \exp \left\{ jk \Delta u f(t, \tau, n \Delta u) v_0(n \Delta u) \right\} \rangle \\ &= \exp \left[-\pi p \Delta u \left\{ k f(t, \tau, n \Delta u) \right\}^2 \right] \cdot I \dots \dots \dots (A-6) \end{aligned}$$

where,

$$I = (\Delta u/4\pi p)^{1/2} \int_{-\infty}^{+\infty} \exp \left[-\Delta u \cdot \left\{ v_0 - j2\pi p k f(t, \tau, n \Delta u) \right\} / 4\pi p \right] dv_0 \dots \dots \dots (A-7)$$

Since the integrand of Equation (A-7) has no singular point, integration can be carried

out along a contour on which the argument of exponential function is real. This contour integral is equal to the integration of Equation (A-4) with respect to v_0 over the whole range. Thus I of Equation (A-7) is unity. Substitution of Equation (A-6) into (A-2) gives

$$R(\tau) = V_0^2 \lim_{\Delta u \rightarrow 0} \prod_{n=-\infty}^{\infty} \exp[-\pi p \Delta u \cdot \{kf(t, \tau, n \Delta u)\}^2] \dots (A-8)$$

The product of exponential functions can be expressed by an exponential function whose argument is the sum of all arguments of factored exponential functions given in Equation (A-8), i.e.,

$$R(\tau) = V_0^2 \exp[-\pi p k^2 \int_{-\infty}^{+\infty} \{f(t, \tau, u)\}^2 du] \dots (A-9)$$

where summation is replaced by the integral in accordance with the definition of an integral. Estimation of $R(\tau)$ using Equation (A-9) is time consuming, as the function $f(t, \tau, u)$ in Equation (A-9) is given as an integral expression (see Equation (8) in the text). To reduce computation time, Equation (8) is substituted into Equation (A-9). The integral $F(t, \tau)$ in Equation (A-9) is

$$F(t, \tau) \equiv \int_{-\infty}^{+\infty} \{f(t, \tau, u)\}^2 du = \int_t^{t+\tau} \int_t^{t+\tau} \int_{-\infty}^{+\infty} h(x, u) \cdot h(y, u) du dx dy, \dots (A-10)$$

where the order of triple integration is changed. Since the range of the integral with respect to u extends infinitely in the positive and negative directions, a closed expression can be expected for the integral.

Let $Q(x, y)$ be the integral with respect to u , i.e.,

$$Q(x, y) \equiv \int_{-\infty}^{+\infty} h(x, u) h(y, u) du \dots (A-11)$$

To calculate $Q(x, y)$, Equation (4) in the text is substituted into Equation (A-11):

$$Q(x, y) = \frac{1}{(2\pi)^2} \int_{-\infty}^{+\infty} \int_{-\infty}^{+\infty} \int_{-\infty}^{+\infty} H(\omega) H(\lambda) \cdot \exp\{j\omega(x-u) + j\lambda(y-u)\} \cdot d\omega d\lambda du \dots (A-12)$$

The order of integration is changed again and the integral with respect to u is given by the Dirac delta function¹⁸⁾, i.e.,

$$\frac{1}{2\pi} \int_{-\infty}^{+\infty} \exp\{-j(\omega + \lambda)u\} du = \delta(\omega + \lambda) \dots (A-13)$$

Substitution of Equation (A-13) into Equation (A-12) gives

$$Q(x, y) = \frac{1}{2\pi} \int_{-\infty}^{+\infty} \int_{-\infty}^{+\infty} H(\omega) H(\lambda) \delta(\omega + \lambda) \cdot \exp\{j(\omega x + \lambda y)\} d\omega d\lambda = \frac{1}{2\pi} \int_{-\infty}^{+\infty} H(\omega) H(-\omega) \cdot \exp\{j\omega(x-y)\} d\omega \dots (A-14)$$

Since the function $H(\omega)$ is zero in the range where the modules of ω is larger than ω_{\max} , the range of the integral in Equation (A-14) is restricted to the finite range where $|\omega|$ is smaller than ω_{\max} . Equation (A-14) is used in Equation (A-10) and $F(t, \tau)$ is given as

$$F(t, \tau) = \frac{1}{2\pi} \int_{-\omega_{\max}}^{+\omega_{\max}} H(\omega) H(-\omega) \cdot \int_t^{t+\tau} \exp(j\omega x) dx \cdot \int_t^{t+\tau} \exp(-j\omega y) dy \} d\omega \dots (A-15)$$

Equation (A-15) can be simplified by carrying out the integrals with respect to x and y , i.e.,

$$F(t, \tau) = \frac{1}{\pi} \int_{-\omega_{\max}}^{+\omega_{\max}} H(\omega) H(-\omega) \cdot \left\{ \frac{1 - \cos(\omega\tau)}{\omega^2} \right\} d\omega \dots (A-16)$$

Substitution of Equation (A-16) into Equation (A-9) gives Equation (9) in the text.

References

- 1) Komaki, S. et al.: Characteristics of a High Capacity 16-QAM Digital Radio System in Multipath Fading. *IEEE Trans. Commun.*, **COM-27**, 12, pp. 1854-1861 (1979).
- 2) Noguchi, T. et al.: 6 GHz 135 Mbps Digital Radio System with 64-QAM Modulation. *IEEE Int. Conf. Commun.* 1983, pp. F4.2.1-F4.2.5.

- 3) Fukuda, M. et al.: Design of 64-QAM Modem for High-Capacity Digital Radio Systems. IEEE Global Telecommun. Conf. 1983, pp. 25.5.1-25.5.5.
- 4) Daido, Y. et al.: 256-QAM Modem for High-Capacity Digital Radio Systems. IEEE Global Telecommun. Conf. 1984, pp. 547-551.
- 5) Ryu, T. et al.: A Stepping Square 256-QAM Digital Radio System. IEEE Int. Conf. Commun. 1986, pp. 1477-1481.
- 6) Ichikawa, H. et al.: 256-QAM Multi-carrier 400-Mb/s Microwave Radio System Field Tests. IEEE Int. Conf. Commun. 1987, pp. 1893-1898.
- 7) Dodo, J., and Kurematsu, H.: Interference Problems of Digital (PSK) and FM Radio Relay System. *FUJITSU Sci. Tech. J.*, **9**, 1, pp. 43-65 (1973).
- 8) Kurematsu, H., Manabe, T., and Kakubari, M.: Investigation of Interchannel Interference between Digital (PSK) and FM Radio Relay Systems. *FUJITSU Sci. Tech. J.*, **14**, 2, pp. 45-61 (1978).
- 9) Rowe, H.E. et al.: Spectra of Low-Deviation Frequency-Modulated Waves. *IEEE Trans. Commun.*, **COM-19**, 6, pp. 1172-1178 (1971).
- 10) Prabhu, V.K.: Spectral Density Bounds on an FM Waves. *IEEE Trans. Commun.*, **COM-20**, 5, pp. 980-984 (1971).
- 11) Mueller, M. et al.: Spectral Energy Distribution of Radio Link FM. *IEEE Trans. Commun.*, **COM-20**, 2, pp. 165-173 (1972).
- 12) CCIR Recommendation 275-3: Pre-emphasis Characteristic for Frequency Modulation Radio-Relay Systems for Telephony Using Frequency-Division Multiplex.
- 13) Urkowitz, H.: Signal Theory and Random Processes. Washington, Artech House Inc., 1983, pp. 361-363.
- 14) Urkowitz, H.: Signal Theory and Random Processes. Washington, Artech House Inc., 1983, p. 383.
- 15) Stojanovic, Z.D. et al.: A New Demodulation Method Improving FM System Interference Immunity. *IEEE Trans. Commun.*, **COM-29**, 7, pp. 1001-1011 (1981).
- 16) Pontano, B.A.: Interference into Angle-Modulated Systems Carrying Multichannel Telephony Signals. *IEEE Trans. Commun.*, **COM-21**, 6, pp. 714-727 (1973).
- 17) Davenport Jr., W.B. et al.: An Introduction to the Theory of Random Signals and Noise. McGraw-Hill, 1985, pp. 61-63.
- 18) Urkowitz, H.: Signal Theory and Random Processes. Washington, Artech House Inc., 1983, p. 10.



Yoshimasa Daido

Radio & Satellite Communication
System Laboratory
FUJITSU LABORATORIES,
KAWASAKI
Bachelor of Electronical Eng.
Tokyo Institute of Technology 1968
Master of Electrical Eng.
Tokyo Institute of Technology 1970
Specializing in Radio Communication
System



Hiroshi Nakamura

Radio & Satellite Communication
System Laboratory
FUJITSU LABORATORIES,
KAWASAKI
Bachelor of Electrical Eng.
University of Electro-Communications
1966
Specializing in Digital Radio System

High Quality Toner Image Transfer in Electrophotographic Printing

• Masashi Ogasawara • Masatoshi Kimura

(Manuscript received March 1, 1988)

This paper presents a newly developed transfer method for electrophotographic printers. This method uses a medium such as silicone rubber to which a toner image is first transferred by pressure and from which the image is then retransferred and fixed onto paper by pressure and heat. The resulting image resolution of 1 000 dots per inch is due to less toner scatter. This method is suitable for in-house printing and desktop publishing applications.

1. Introduction

The primary application of the electrophotographic process is in xerographic copiers and laser printers.

This process has seven steps: charging the photoconductor, exposing it to produce a latent electrostatic image, developing the image with toner, transferring the toner image to paper, fixing the image, cleaning the photoconductor, and erasing surface charges on the photoconductor.

There are two problems inherent in conventional electrostatic transfer¹⁾ of toner images by electrostatic force:

- 1) The quality of the transferred image can be degraded by nonuniformity in the electric transfer field.
- 2) Toner that has low electrical resistivity ($< 10^{14} \Omega\text{cm}$), and which easily produces a sharp toner image, is difficult to transfer to plain paper, which leaks an electric charge.

The expansion of in-house printing systems (IPS) and desktop publishing (DTP) has increased the need for printers that provide better quality imaging. Developments in electrophotographic technology have provided toner images with higher resolution, but the resolution of electrostatic transfer images is limited.

The nonelectrostatic transfer method

we studied uses a medium that has a high affinity for toner and low free surface energy ($< 40 \text{ dyn/cm}$).

The transfer principle and the results of experiments exploring various transfer characteristics are explained in the following sections.

2. Transfer principle

Nonelectrostatic transfer involves adhesive

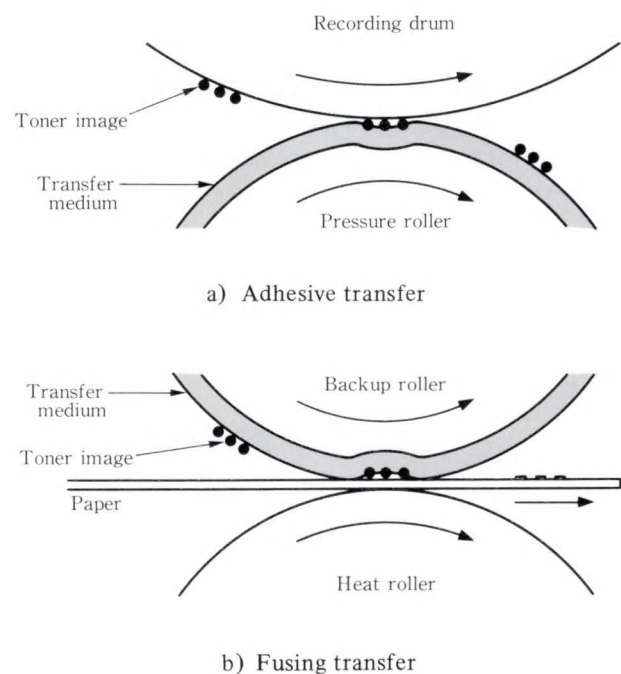


Fig. 1—Transfer mechanism.

(first) and fusing (second) transfers.

2.1 Adhesive transfer

In the first transfer zone, the transfer medium is brought into contact with the recording drum by a pressure roller { see Fig. 1-a } The transfer medium has a high affinity for toner, a low level of free surface energy, and is heat resistant. Materials having these properties include silicone rubber.

The toner image that forms on the recording drum passes between the recording drum and transfer medium and is pressed against the transfer medium by a pressure roller. The adhesive force of the transfer medium, which exceeds the electrostatic force of the recording drum, lifts the toner image off the drum onto the transfer medium.

2.2 Fusing transfer

In the second transfer zone, the second backup roller presses the transfer medium into indirect contact with the heat roller, the intervening material being the paper { see Fig. 1-b } . The toner image having been transferred to the transfer medium and carried to the second transfer zone is now pressed between the transfer medium and paper, where the toner is fused by heat passing from the heat roller through the paper. The fusing toner is repelled from the transfer medium surface because of the medium's low surface energy. The heated toner is simultaneously pressed into the paper fibers and fixed permanently on the paper surface.

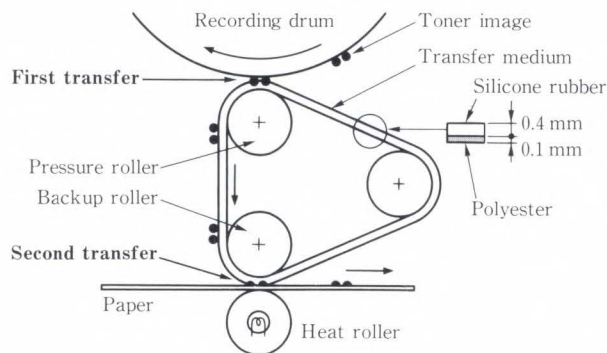


Fig. 2—Experimental setup.

3. Experiments

3.1 Setup

Figure 2 shows the experimental setup. The transfer medium is a continuous belt of 0.1 mm polyester film base coated with 0.4 mm of silicone rubber, providing a transfer medium with a smooth surface and low free surface energy (about 20 dyn/cm). Low electrical resistivity toner ($10^5 \Omega\text{cm}$) and plain paper (Xerox L Paper) are used.

First, the toner image is formed on the recording drum. In the first transfer zone, the image is transferred from the recording drum to the transfer medium by an adjustable spring-driven pressure roller. The image is carried to the second transfer zone, where it is pressed between the transfer medium and paper, heated, and transferred to the paper. The heat is provided by an adjustable halogen lamp.

3.2 Evaluation

Basic transfer conditions were investigated by adjusting parameters such as rubber hardness, roller pressure, and the surface temperature of the heat roller.

3.2.1 Transfer efficiency and fixing ratio

Transfer efficiency refers to the relative amounts of toner on the drum, transfer medium and paper before and after a transfer.

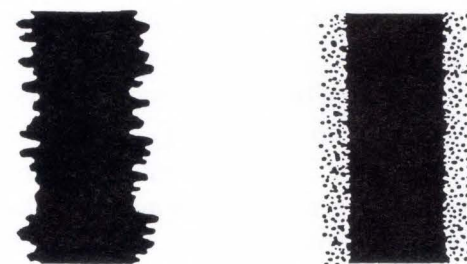
Efficiency for the first transfer, η_1 , and for the second, η_2 , are given as

$$\eta_1 = D_1/D_0 \times 100 (\%),$$

$$\eta_2 = D_2/D_1 \times 100 (\%),$$

where

D_0 : Optical toner-image density on the recording drum,



a) Raggedness

b) Blur

Fig. 3—Edge structure of toner image.

D_1 : Optical toner-image density on the transfer medium, and

D_2 : Optical toner-image density on paper.

Adhesion of the fixed image to paper is measured by applying adhesive tape (3M No. 810 tape) to the fixed image at a constant pressure with an iron roller and then peeling the tape off.

Fixing ratio f is given as

$$f = D_3/D_2 \times 100 (\%),$$

where

D_3 : Optical toner-image density on paper after the tape adhesion test.

3.2.2 Sharpness

In electrophotography, image sharpness is judged according to the concepts of raggedness and blur²⁾ (see Fig. 3).

Raggedness results when not enough toner is transferred to the image edges or when the toner is scattered during transfer. Scattered toner is spread and fused in "clumps" during image fixing.

Blur is usually the result of toner being scattered during transfer. Scattered toner changes the area of the screen dots and has poor gray-scale reproducibility. The randomness of the scattering makes screen dots uneven.

For raggedness, we evaluated the rising width of the characteristic curve of a line image by measuring the area rate of the toner image in the direction of line width.

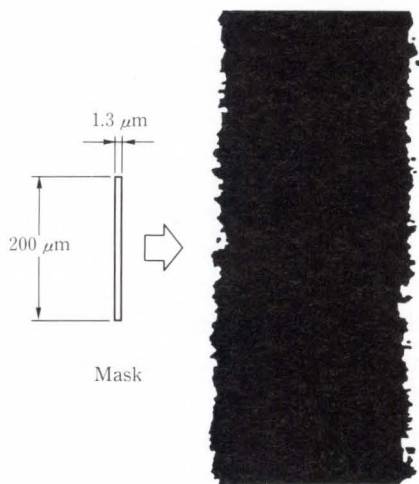


Fig. 4—Scanning mask.

The toner area rate (Fig. 4) is measured using a $1.3 \times 200 \mu\text{m}$ scanning mask in an image analyzer. The curve in Fig. 5 is the toner area rate for a position in the line image. The rising width, w_0 , is defined by

$$w_0 = (w_1 + w_2)/2,$$

where

w_1, w_2 : Distance over which the toner area rate goes from 10 percent to 90 percent.

For blur, we evaluated the amount of scatter in the area rate of screen dots before and after toner transfer³⁾

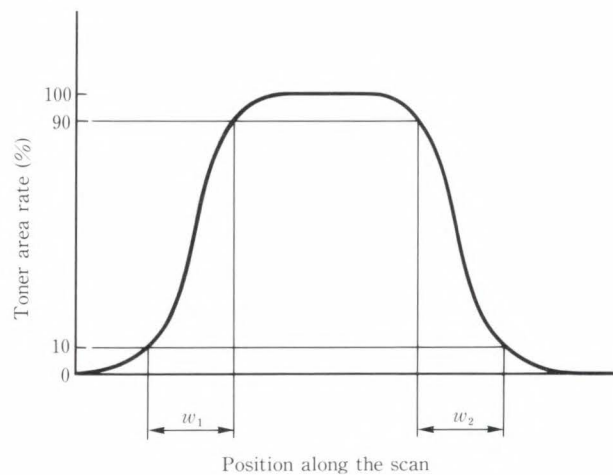


Fig. 5—Rising width w_1 and w_2 .

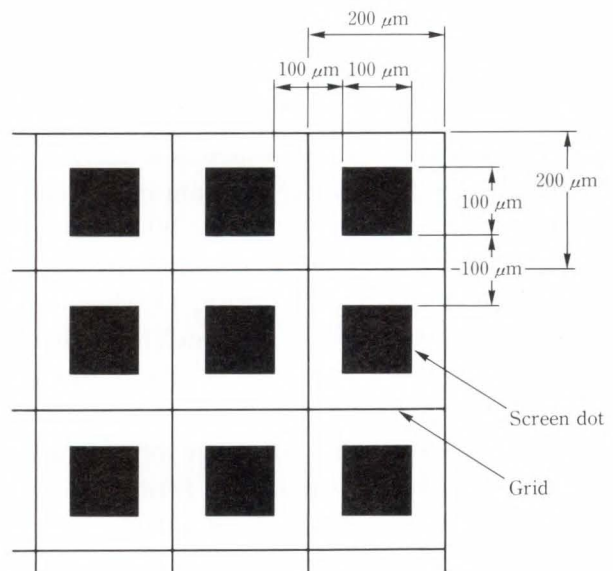


Fig. 6—Screen dot measurement.

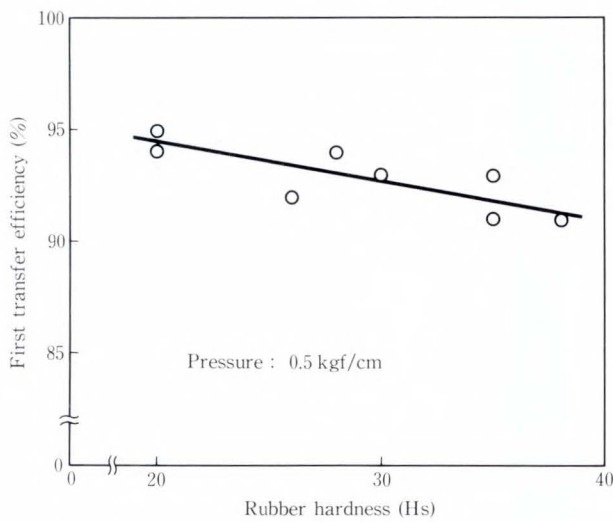


Fig. 7—Efficiency of first transfer as a function of rubber hardness.

One hundred screen dots of $100 \times 100 \mu\text{m}$ are separated by a $200 \times 200 \mu\text{m}$ grid (Fig. 6), and for each grid, the area rate, x_i , is measured by an image analyzer (toner separated from dot images included). After calculating the average, \bar{x}_i , and the standard deviation of area rate data, σ_{n-1} , scatter for the area rate in screen dots is given by σ_{n-1}/\bar{x}_i .

4. Results and considerations

4.1 First transfer

Figure 7 shows the efficiency of the first transfer for different hardnesses of rubber at 0.5 kgf/cm. Efficiency decreases gradually with increased rubber hardness because elastic deformation decreases with increased hardness at a constant pressure. With increased hardness, the surface of the transfer medium comes into increased contact with the toner. When rubber hardness is too low ($< 30^\circ$), rubber strength, especially tear strength, decreases to where the rubber cannot be used as a transfer medium. We used a transfer medium having a rubber hardness of 30° .

Figure 8 shows the efficiency of the first transfer at different pressures. Efficiency increases up to a saturation level of 94 percent at a pressure of 0.6 kgf/cm.

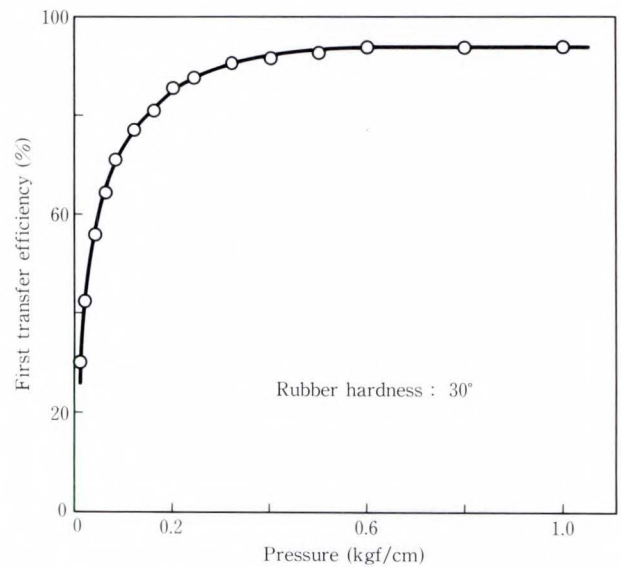


Fig. 8—Efficiency of first transfer as a function of pressure.

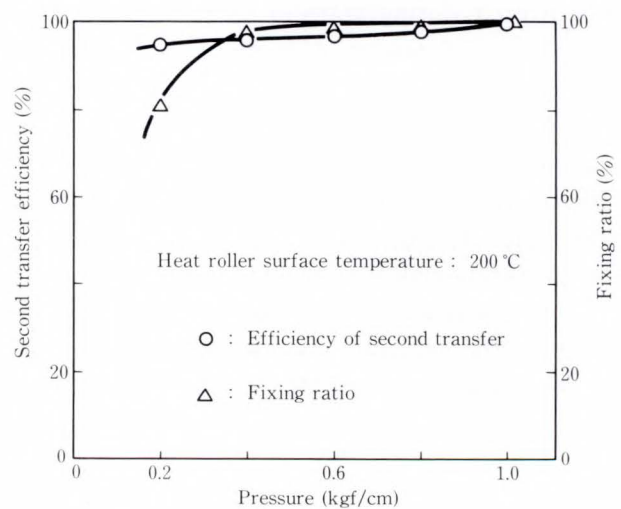


Fig. 9—Characteristics of transfer and fixing as a function of pressure.

4.2 Second transfer

Figure 9 shows the efficiency of the second transfer and the fixing ratio at different pressures in the second transfer zone when the heat roller surface temperature is 200°C . Efficiency increases with pressure, reaching 100 percent at 1.0 kgf/cm. The fixing ratio increases steeply up to 98 percent at 0.4 kgf/cm, and reaches 100 percent at 1.0 kgf/cm. As the pressure increases, the nip between the backup

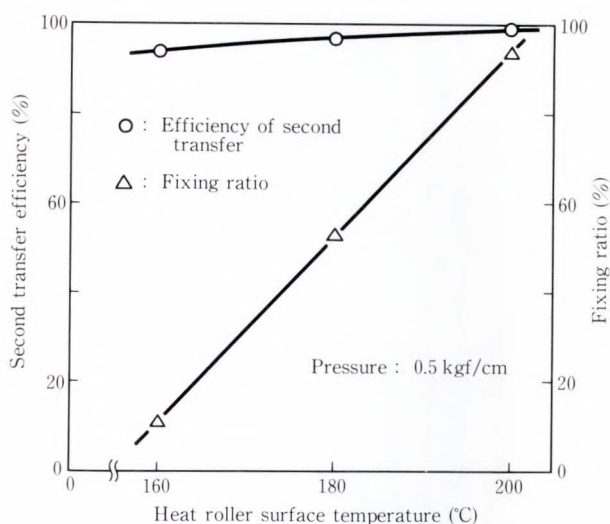


Fig. 10—Characteristics of transfer and fixing as a function of heat roller surface temperature.

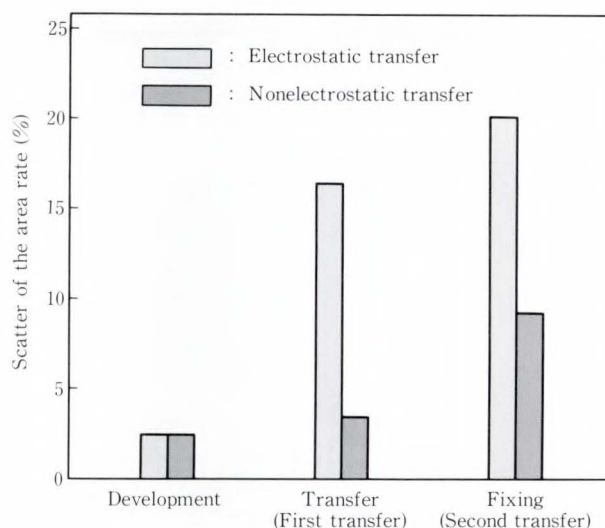


Fig. 12—Area rate scatter of screen dots in each step of electrophotographic process.

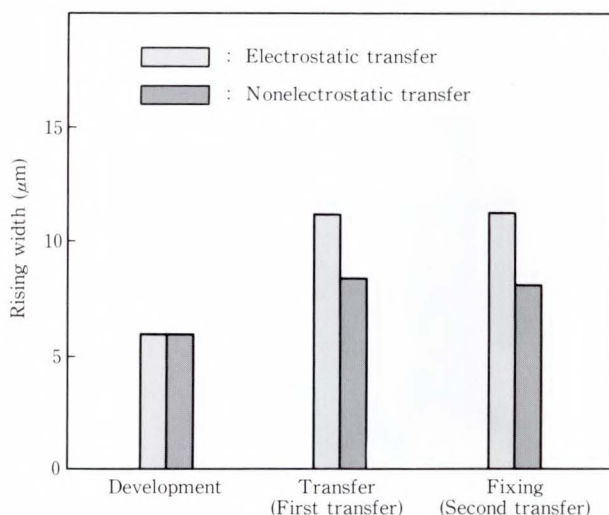


Fig. 11—Rising width of edge in each step of electrophotographic process.

roller and paper also increases, lengthening the toner heating interval. This increases repulsion of the fused toner from the transfer medium surface and aids toner entry into the paper fibers.

Figure 10 shows the efficiency of the second transfer and the fixing ratio at different heat roller surface temperatures under a constant pressure of 0.5 kgf/cm. Both the transfer efficiency and the fixing ratio increase with heat roller surface temperature. The fixing

ratio is particularly influenced by temperature.

4.3 Image sharpness

Based on the studies just discussed, we set up the following experiment.

Figure 11 shows the rising width of the line image edge in electrostatic and nonelectrostatic transfer. In electrostatic transfer, the rising width in transfer step is 1.9 times that at development. Fixing does not increase this ratio. In nonelectrostatic transfer, the rising width in the first transfer step is 1.4 times that at development, with no increase in the second transfer step.

Figure 12 shows scatter in the area rate for screen dots in electrostatic and nonelectrostatic transfer. In electrostatic transfer, the area rate scatter in transfer is 6.6 times that at development. The rate after fixing is 8 times that at development. In nonelectrostatic transfer, the scatter rate in the first transfer step is 1.4 times that at development. In the second transfer step, the rate is 3.7 times that at development. The reason for this is that the surface roughness of plain paper prevents sufficient contact between the paper and the transfer medium, preventing complete transfer of the toner image. In an attempt to clarify this phenomenon, we used coated paper with

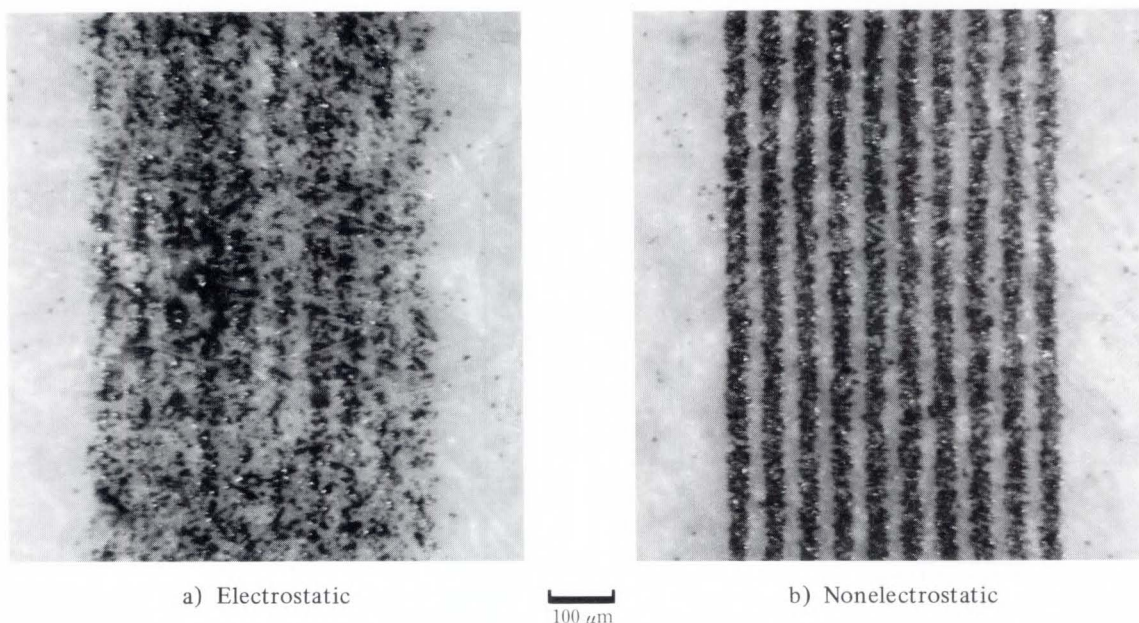


Fig. 13—Samples of high-resolution image printing.

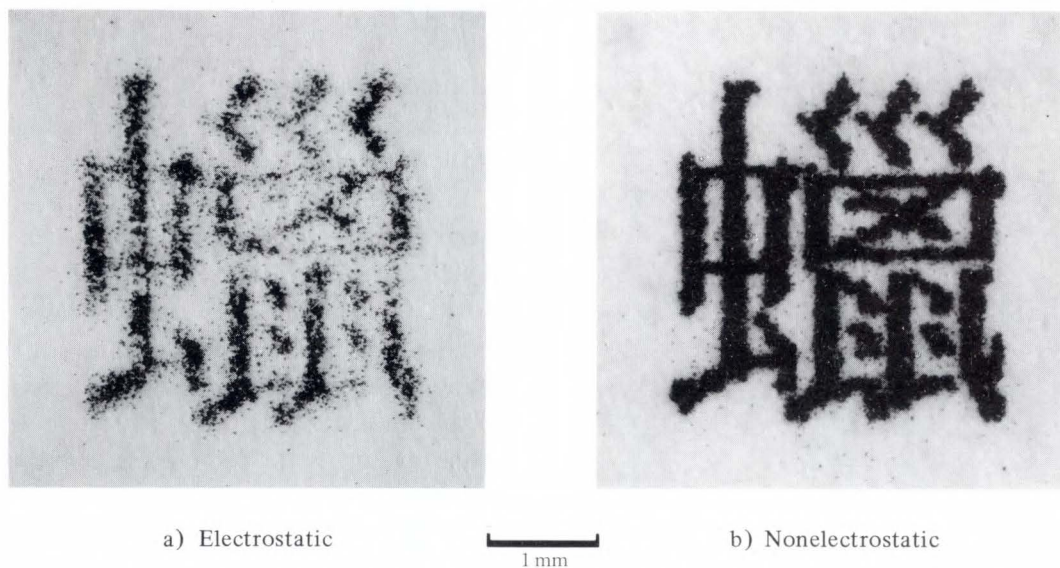


Fig. 14—Printing samples when transferred toner has low electrical resistivity to plain paper.

a smooth surface, and found that area rate scatter was limited to two times that at development.

To summarize, the nonelectrostatic transfer method we studied enabled sharper images than electrostatic transfer because less toner was scattered during the transfer steps.

4.4 Quality of transferred images

Figure 13 shows examples of a high-resolution image printing when using electrostatic

transfer a) and nonelectrostatic transfer b). The line image resolution is 1016 dots per inch (40 lines per millimeter). Clearly, for a toner image of 1000 dots per inch, the nonelectrostatic transfer method is much better than conventional electrostatic transfer.

Figure 14 compares plain paper electrostatic transfer a) and nonelectrostatic transfer b) printing samples when using toner having low electrical resistivity ($10^5 \Omega\text{cm}$). Nonelectrostatic transfer clearly produces a sharper toner image

on plain paper, even when low electrical resistivity toner is used.

5. Conclusion

A new transfer method for electrophotographic printers has been developed. Use of a transfer medium having a high affinity for toner and low free surface energy enables images to be transferred without electrostatic force.

A toner image of 1 000 dots per inch was transferred and was sharp on plain paper because of reduced toner scatter. Further, it was possible to transfer low electrical resistivity toner to plain paper because the electrical characteristics of the toner and the paper were independent.

Nonelectrostatic transfer produced high-quality image printing and is suitable for use in IPS and DTP applications.

References

- 1) Kimura, M., Nakajima, J., Horie, M., and Takahashi, H.: Electrostatic Transfer of Toner Image. (in Japanese), *Soc. J. Electrophoto.*, **19**, 1, pp. 25-32 (1981).
- 2) Inagaki, T.: Image Evaluation for Plain Paper Copiers. (in Japanese), *Optics*, **12**, 4, pp. 267-277 (1983).
- 3) Horie, K., and Maruyama, K.: What is the High Quality Image in Electrophotography? (in Japanese), *Soc. J. Electrophoto.*, **26**, 1, pp. 48-54 (1987).



Masashi Ogasawara

Printer Technology Laboratory
FUJITSU LABORATORIES, ATSUGI
Bachelor of Mechanical Eng.
Yokohama National University 1982
Specializing in Electrophotographic
Printing Technology



Masatoshi Kimura

Printer Technology Laboratory
FUJITSU LABORATORIES, ATSUGI
Bachelor of Electronic Eng.
Okayama University 1973
Dr. of Electronic Eng.
Osaka University 1986
Specializing in Electrostatic Recording
and Electrophotographic Technology

Liquid Phase Epitaxial Growth of Fe-Doped Semi-Insulating InP, GaInAsP, and AlGaInAs

• Toshiyuki Tanahashi • Makoto Kondo • Mitsuru Sugawara

(Manuscript received March 2, 1988)

Fe-doped InP, $\text{Ga}_x\text{In}_{1-x}\text{As}_y\text{P}_{1-y}$, and $\text{Al}_u\text{Ga}_v\text{In}_{1-u-v}\text{As}$ grown by liquid phase epitaxy have been extensively studied. The temperature, composition, and material dependences of Fe doping characteristics of these materials are well explained by three factors: the Fe solubility in the growth solution, the background electron concentration, and the Fe distribution coefficient. The high resistivities of 8×10^7 ohm·cm, 2×10^5 ohm·cm, and 1×10^9 ohm·cm have been obtained for InP grown at 900°C , $\text{Ga}_{0.26}\text{In}_{0.74}\text{As}_{0.57}\text{P}_{0.43}$ and $\text{Al}_{0.48}\text{In}_{0.52}\text{As}$ grown at 750°C , respectively.

The activation energies of the Fe acceptor levels in $\text{Ga}_x\text{In}_{1-x}\text{As}_y\text{P}_{1-y}$ and $\text{Al}_u\text{Ga}_v\text{In}_{1-u-v}\text{As}$ systems have been also studied. It is found that the Fe acceptor level is aligned at a constant energy relative to the vacuum level.

1. Introduction

Semi-insulating (SI) InP and III-V alloy semiconductors lattice matched to InP are useful for high speed optical and electronic device applications. In particular, SI layers are superior to p-n junctions as current confining layers in $\text{Ga}_x\text{In}_{1-x}\text{As}_y\text{P}_{1-y}$ -InP buried heterostructure (BH) lasers, because they offer a significant reduction in both parasitic capacitance and leakage current^{1),2)}.

In general, SI III-V semiconductors are obtained by introducing transition metals which form deep levels in the forbidden gap. Fe is well known as a deep level impurity which provides SI properties to InP. Fe-doped SI InP has been obtained by the liquid encapsulated Czochraski (LEC)³⁾ and the metal organic vapor phase epitaxy (MOVPE)⁴⁾⁻⁶⁾. So far, however, it has been difficult to obtain the liquid phase epitaxial (LPE) layers of SI InP and other III-V compounds by Fe doping. This is mainly because the Fe solubility and distribution coefficient are very small at the growth temperature

usually used.

Recently, the authors succeeded for the first time in achieving LPE growth of Fe-doped SI InP by using high growth temperatures above 850°C ⁷⁾. Moreover, Fe-doped SI $\text{Ga}_x\text{In}_{1-x}\text{As}_y\text{P}_{1-y}$ and $\text{Al}_u\text{Ga}_v\text{In}_{1-u-v}\text{As}$ lattice matched to InP have also been obtained by LPE growth at the low growth temperature of 750°C ^{8),9)}. These two alloy systems lattice matched to InP have almost the same energy gap range, which is very important for optical devices.

The authors' research into Fe doping characteristics of InP, $\text{Ga}_x\text{In}_{1-x}\text{As}_y\text{P}_{1-y}$, and $\text{Al}_u\text{Ga}_v\text{In}_{1-u-v}\text{As}$ is reported in this paper. The temperature and composition dependences of the Fe doping characteristics of the $\text{Ga}_x\text{In}_{1-x}\text{As}_y\text{P}_{1-y}$ system (including InP) and the difference in Fe doping characteristics between $\text{Ga}_x\text{In}_{1-x}\text{As}_y\text{P}_{1-y}$ and $\text{Al}_u\text{Ga}_v\text{In}_{1-u-v}\text{As}$ systems are mainly discussed. These characteristics are explained by three factors: the Fe solubility in the growth solution, the background electron concentration, and the Fe distribution coef-

ficient. The activation energies of the Fe acceptor levels in $\text{Ga}_x\text{In}_{1-x}\text{As}_y\text{P}_{1-y}$ and $\text{Al}_u\text{Ga}_v\text{In}_{1-u-v}\text{As}$ systems have been also studied.

2. Experiment

Undoped or Fe-doped epitaxial layers were grown on Sn-doped n^+ - or Fe-doped SI InP substrates. Sn- and Fe-doped layers were also grown on Zn-doped p^+ -InP substrates. InP and $\text{Ga}_x\text{In}_{1-x}\text{As}_y\text{P}_{1-y}$ layers were grown on (100) oriented substrates and $\text{Al}_u\text{Ga}_v\text{In}_{1-u-v}\text{As}$ were grown on (111)B oriented substrates. The growth temperatures of InP were 650 °C, 750 °C, 800 °C, 850 °C, and 900 °C. The $\text{Ga}_x\text{In}_{1-x}\text{As}_y\text{P}_{1-y}$ and $\text{Al}_u\text{Ga}_v\text{In}_{1-u-v}\text{As}$ layers were grown at 750 °C.

The lattice mismatch between the epitaxial layer and the substrate was less than 1×10^{-3} for $\text{In}_x\text{Ga}_{1-x}\text{As}_y\text{P}_{1-y}$ and $\text{Al}_u\text{Ga}_v\text{In}_{1-u-v}\text{As}$, as measured using double crystal X-ray diffraction.

The energy gaps of $\text{Ga}_x\text{In}_{1-x}\text{As}_y\text{P}_{1-y}$ layers were 0.75 eV for GaInAs ($y = 1$), 0.98 eV for GaInAsP ($y = 0.57$), and 1.24 eV for GaInAsP ($y = 0.16$), while those of $\text{Al}_u\text{Ga}_v\text{In}_{1-u-v}\text{As}$ were 0.80 eV for AlGaInAs ($u = 0.04$), 0.95 eV for AlGaInAs ($u = 0.16$), 1.24 eV for AlGaInAs ($u = 0.36$), and 1.45 eV for AlInAs ($u = 0.48$). These energy gaps were measured using photoluminescence. The arsenic compositions in $\text{Ga}_x\text{In}_{1-x}\text{As}_y\text{P}_{1-y}$ layers or the aluminum compositions in $\text{Al}_u\text{Ga}_v\text{In}_{1-u-v}\text{As}$ layers were determined using the composition dependence of the energy gap for each alloy system lattice matched to InP^{(10), (11)}.

Since the residual impurity in the epitaxial layers has to be reduced as possible in order to obtain the SI properties by Fe doping, the materials with the highest purity were carefully selected for the LPE growth. It was found that the background impurity density was mainly determined by the quality of indium. The impurity level of indium was 10^{-7} and that of iron was 10^{-4} . An AlIn mother alloy, which was composed of indium with an impurity level of 10^{-6} and aluminum with the same impurity level, was used as the aluminum source⁽¹²⁾. The other source materials, InP, InAs, and GaAs were undoped crystals with a carrier concentra-

tion of less than 10^{16} cm^{-3} . Specific purification techniques, such as baking for long periods of time⁽¹³⁾, were not employed.

The most serious problem in high temperature growth is thermal damage to the InP substrates and InP epitaxial layers. To eliminate this problem for the InP substrate, the InP substrate was covered with an InP single crystal until the growth started and was etched *in situ* by undersaturated In-P solution prior to the growth. The as-grown InP epitaxial layer was covered by another InP single crystal immediately after the growth.

The electron concentrations and the resistivities of the epitaxial layers were measured using Van der Pauw samples which were grown on SI substrates. When the resistivities exceeded $1 \times 10^5 \text{ ohm}\cdot\text{cm}$, they were determined from the current-voltage characteristics of n^+ (cap layer)-SI(Fe-doped layer)- n^+ (substrate) structure mesa diodes⁽¹⁴⁾. The samples for measurement were prepared as follows. Alloyed Au-Ge Ohmic contacts were formed on both sides of the wafers. Then mesa diodes with a diameter of 200-800 μm were fabricated by chemical etching.

Secondary ion mass spectroscopy (SIMS) analyses were performed on undoped and Fe-doped samples to estimate the Fe concentrations in the epitaxial layers.

Deep level transient spectroscopy (DLTS) measurements were performed on InP ($y = 0$) and GaInAs ($y = 1$) layers using n (Sn- and Fe-doped layer)- p^+ (substrate) mesa diodes⁽¹⁵⁾.

3. Results

3.1 Surface morphology

Normarsky microphotographs of the as-grown surfaces of the undoped InP layer and 0.4 wt% Fe-doped InP layer grown at 900 °C are shown in Fig. 1. Both as-grown surfaces were mirror-like. No significant degradation by high temperature growth and Fe doping was observed on the surface morphologies. Good surface morphologies were also obtained for $\text{Ga}_x\text{In}_{1-x}\text{As}_y\text{P}_{1-y}$ and $\text{Al}_u\text{Ga}_v\text{In}_{1-u-v}\text{As}$ layers grown at 750 °C. Figure 2 shows the surface morphologies of GaInAsP ($y = 0.57$) and

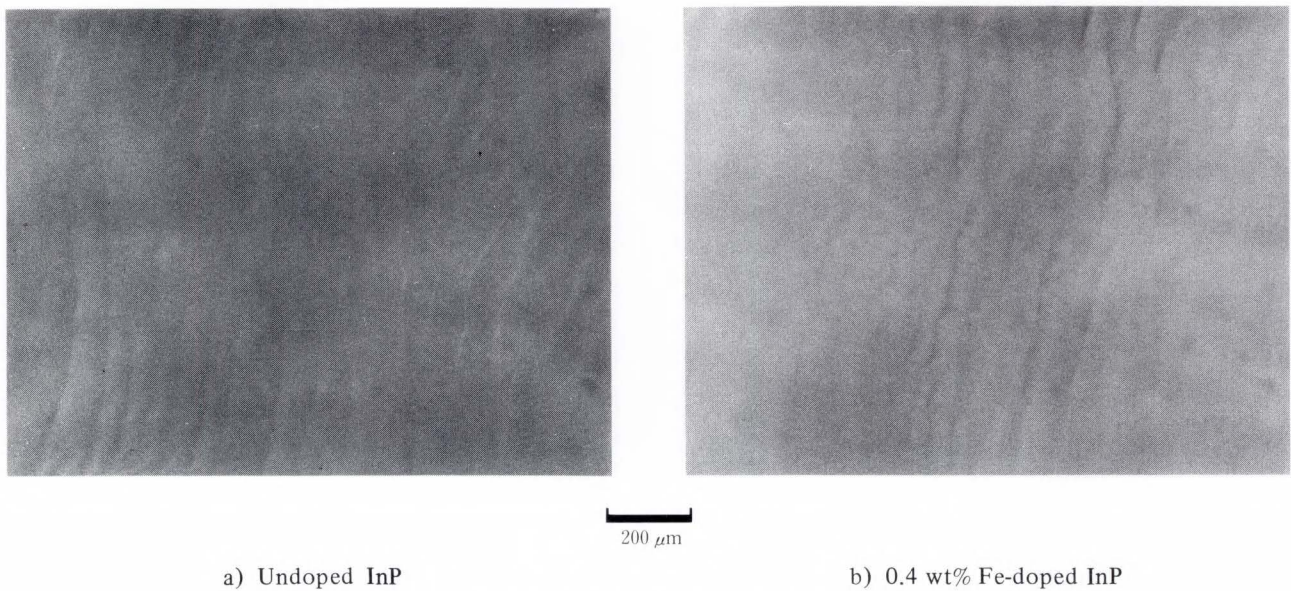


Fig. 1—Surface morphologies of InP grown at 900 °C.

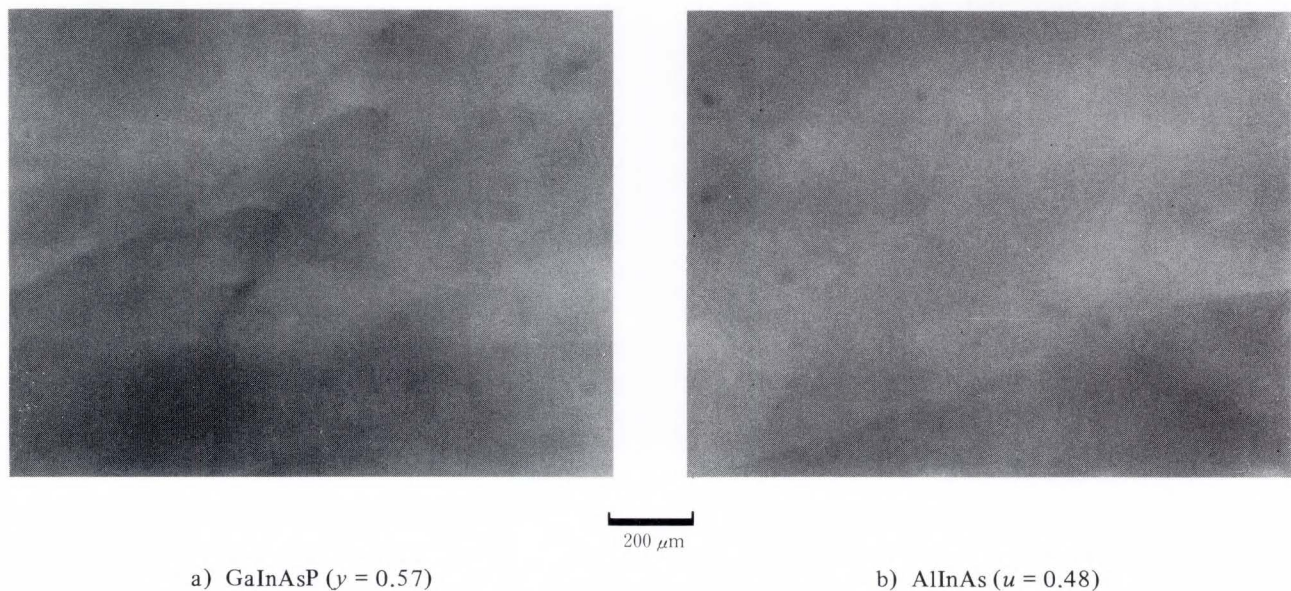


Fig. 2—Surface morphologies, grown at 750 °C.

AlInAs ($u = 0.48$).

3.2 Background electron concentration

Figure 3 shows the growth temperature dependence of the background electron concentration at 300 K and the electron mobility at 77 K in undoped InP. The electron concentration was about $1-1.5 \times 10^{15} \text{ cm}^{-3}$ and was almost independent of the growth temperature.

Figure 4 shows the electron concentration (300 K) and electron mobility (77 K) of

undoped $\text{Ga}_x\text{In}_{1-x}\text{As}_y\text{P}_{1-y}$ grown at 750 °C versus the arsenic composition. The electron concentration in $\text{Ga}_x\text{In}_{1-x}\text{As}_y\text{P}_{1-y}$ decreased gradually from about $1 \times 10^{15} \text{ cm}^{-3}$ for InP ($y = 0$) to about $5 \times 10^{14} \text{ cm}^{-3}$ for GaInAs ($y = 1$). The electron concentration (300 K) and electron mobility (77 K) in undoped $\text{Al}_u\text{Ga}_v\text{In}_{1-u-v}\text{As}$ grown at 750 °C versus the aluminum composition are shown in Fig. 5. The electron concentration in $\text{Al}_u\text{Ga}_v\text{In}_{1-u-v}\text{As}$ was about $1.2 \times 10^{15} \text{ cm}^{-3}$ for all the composi-

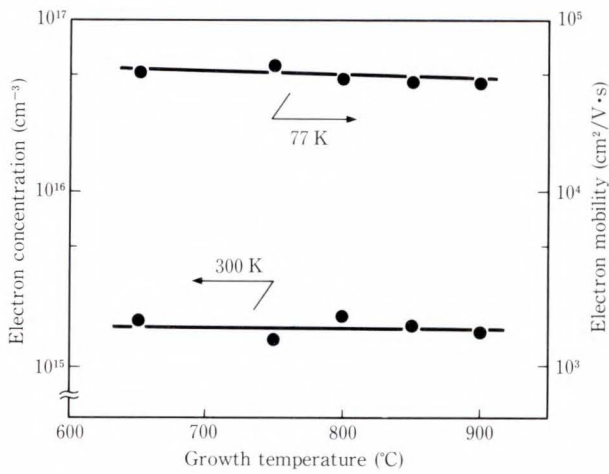


Fig. 3—Growth/temperature dependence of electron concentration at 300 K and electron mobility at 77 K in undoped InP.

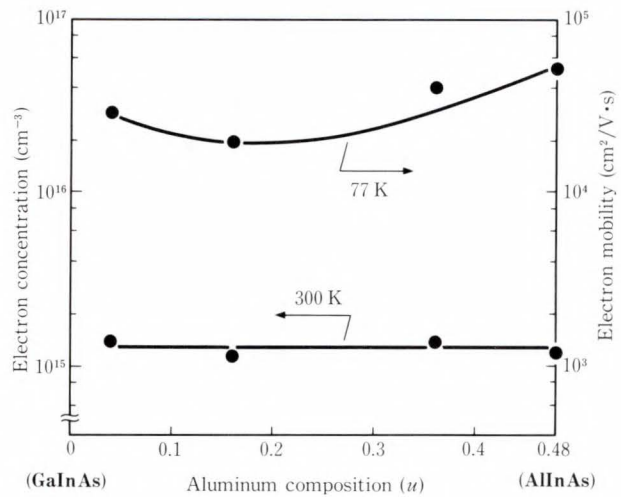


Fig. 5—Composition dependence of electron concentration at 300 K and electron mobility at 77 K in undoped $Al_uGa_vIn_{1-u-v}As$.

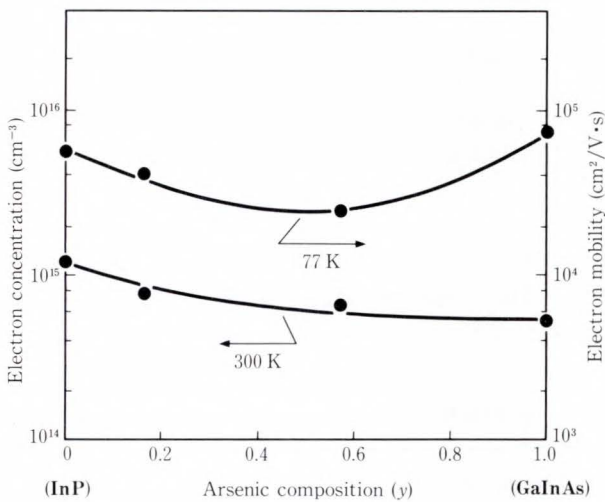


Fig. 4—Composition dependence of electron concentration at 300 K and electron mobility at 77 K in undoped $Ga_xIn_{1-x}As_yP_{1-y}$.

tions. Comparing the results of Figs. 4 and 5, the electron concentration in $Al_uGa_vIn_{1-u-v}As$ is greater than or equal to that in $Ga_xIn_{1-x}As_yP_{1-y}$. As shown in Figs. 3, 4, and 5, high purity epitaxial layers of InP, $Ga_xIn_{1-x}As_yP_{1-y}$, and $Al_uGa_vIn_{1-u-v}As$ were obtained without specific purification techniques.

3.3 Resistivity

Figure 6 shows the resistivity of Fe-doped InP versus the weight percent of Fe in the

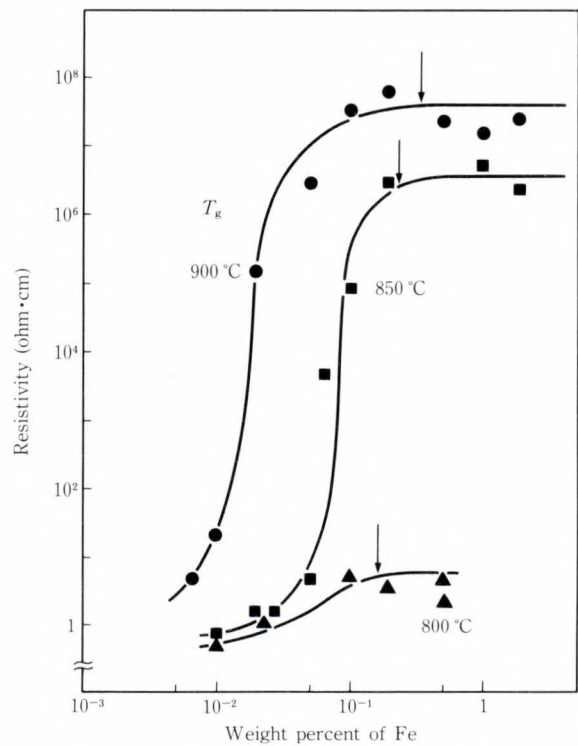


Fig. 6—Resistivity of Fe-doped InP versus the wt% of Fe in the growth temperature. The arrow shows the Fe solubility in an indium solution at each temperature¹⁶⁾ (see subsection 4.1.1).

growth solution at the growth temperatures of 800 °C, 850 °C, and 900 °C. At all growth temperatures, the resistivity increased as the

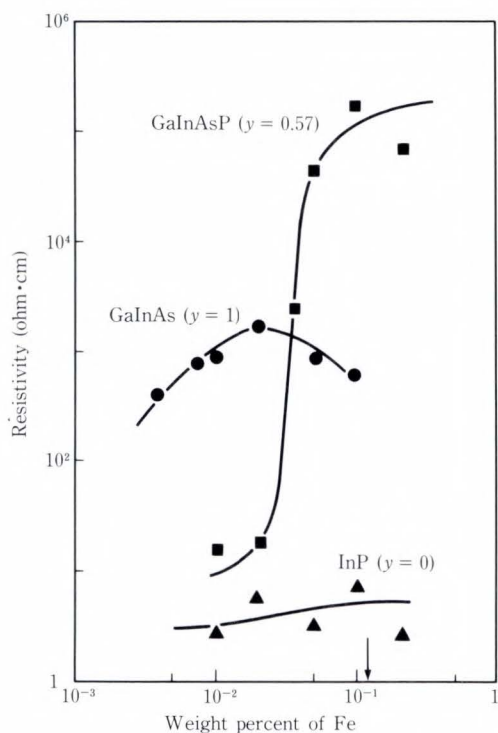


Fig. 7—Resistivity of Fe-doped $Ga_xIn_{1-x}As_yP_{1-y}$ versus the wt% of Fe in the growth solution. The arrow shows the Fe solubility in an indium solution at $750\text{ }^\circ\text{C}^{16)}$ (see subsection 4.1.2).

weight percent of Fe increased. The resistivities increased abruptly at the critical weight percent of Fe at $850\text{ }^\circ\text{C}$ and $900\text{ }^\circ\text{C}$. The Fe critical amount at $900\text{ }^\circ\text{C}$ was less than that at $850\text{ }^\circ\text{C}$. The resistivities saturated at $5 \times 10^6\text{ ohm-cm}$ and $5 \times 10^7\text{ ohm-cm}$ at $850\text{ }^\circ\text{C}$ and $900\text{ }^\circ\text{C}$, respectively. The maximum resistivity was $8 \times 10^7\text{ ohm-cm}$. This is the highest resistivity for InP obtained by LPE to date and is comparable to the resistivity of Fe-doped SI InP grown by MOCVD. All the layers were conductive at the growth temperature of $800\text{ }^\circ\text{C}$.

The resistivities of Fe-doped $Ga_xIn_{1-x}As_yP_{1-y}$ with three compositions (including InP) grown at $750\text{ }^\circ\text{C}$ versus the weight percent of Fe in the growth solution are shown in Fig. 7. GaInAsP ($y = 0.57$) and GaInAs ($y = 1$) were semi-insulating at the growth temperature of $750\text{ }^\circ\text{C}$, while InP ($y = 0$) was conductive. The maximum resistivity was about $2 \times 10^5\text{ ohm-cm}$ for GaInAsP ($y = 0.57$), and about $2 \times 10^3\text{ ohm-cm}$ for GaInAs ($y = 1$). These resistivities were near

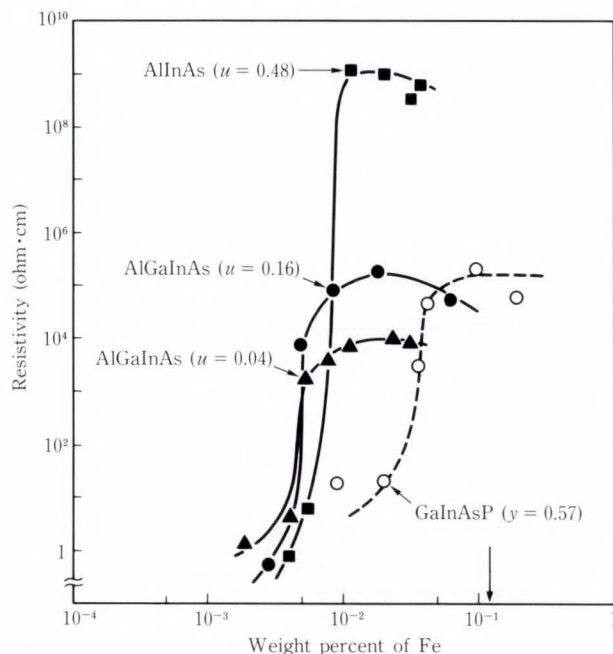


Fig. 8—Resistivity of Fe-doped $Al_uGa_vIn_{1-u-y}As$ versus the wt% of Fe.

The arrow shows the Fe solubility in an indium solution at $750\text{ }^\circ\text{C}^{16)}$ (see subsection 4.1.3).

the maximum theoretical values calculated from the energy gaps. The critical weight percent of Fe where the GaInAs ($y = 1$) resistivity abruptly increased was more than one order of magnitude less than that for GaInAsP ($y = 0.57$).

The resistivities of Fe-doped $Al_uGa_vIn_{1-u-y}As$ with three compositions versus the weight percent of Fe in the growth solution are shown in Fig. 8. In this figure, the results of GaInAsP with the arsenic content of 0.57 (from Fig. 7) are also shown. The resistivity increased abruptly at almost the same weight percent of Fe, and the layers were semi-insulating. The maximum resistivity for AlInAs ($u = 0.48$) with the largest energy gap of 1.45 eV in this system was about $1 \times 10^9\text{ ohm-cm}$. This is the highest resistivity obtained so far for SI alloys lattice matched to InP.

AlGaInAs ($u = 0.16$) and GaInAsP ($y = 0.57$) in Fig. 8 have almost the same energy gap. Comparing Fe doping characteristics between these two alloys, two important points are illustrated. The first is that the maximum

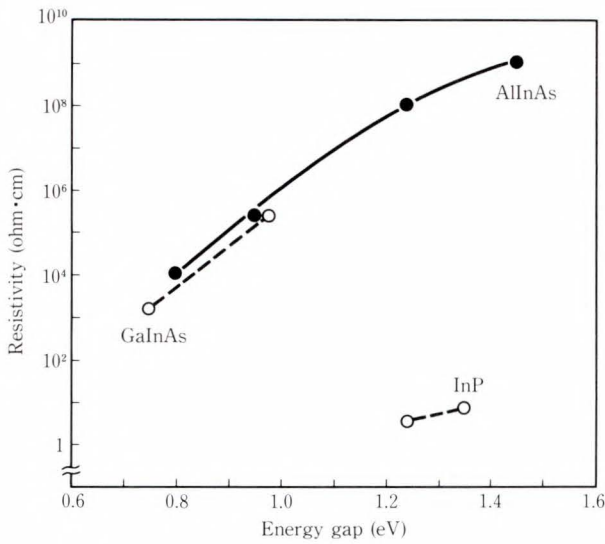


Fig. 9—Maximum resistivity versus the energy gap of the layer for Fe-doped (○) $\text{Ga}_x\text{In}_{1-x}\text{As}_y\text{P}_{1-y}$ and (●) $\text{Al}_u\text{Ga}_v\text{In}_{1-u-v}\text{As}$.

resistivity of both alloys are almost the same. This resistivity is near the maximum theoretical value calculated from the energy gap. The second is that the critical weight percent of Fe where the AlGaInAs ($u = 0.16$) resistivity increased is about one order of magnitude less than that for GaInAsP ($y = 0.57$).

Figure 9 shows the maximum resistivities obtained for Fe-doped $\text{Ga}_x\text{In}_{1-x}\text{As}_y\text{P}_{1-y}$ and $\text{Al}_u\text{Ga}_v\text{In}_{1-u-v}\text{As}$ at the growth temperature of 750 °C versus the energy gap of the layer. The results of Fe-doped GaInAsP ($y = 0.16$) and AlGaInAs ($u = 0.36$) are added to this figure.

Typical current density (j)-voltage (v) characteristics of $n^+\text{-SI-}n^+$ diodes for InP ($y = 0$) and GaInAsP ($y = 0.57$) are shown in Fig. 10. When low voltages were applied, the j - v curves obeyed Ohm's law. Above the Ohmic region, the current increased rapidly above the critical voltage¹⁷⁾.

Temperature dependences of resistivity for

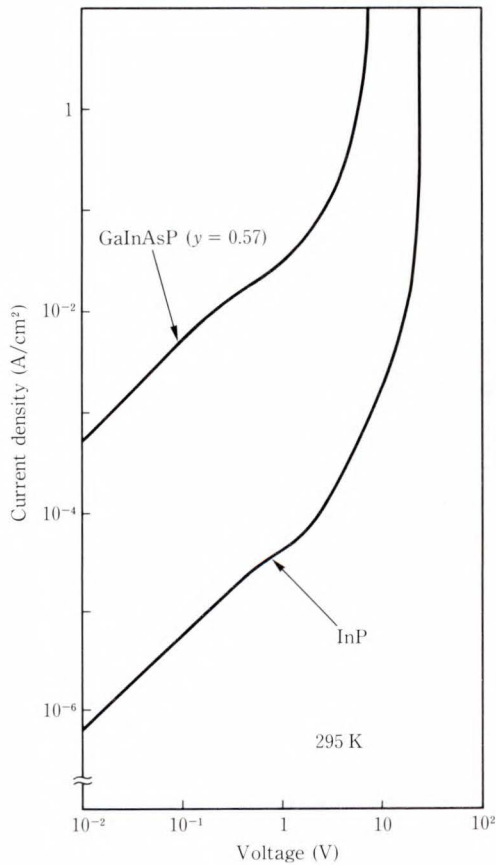


Fig. 10—Typical current density-voltage characteristics of $n^+\text{-Si-}n^+$ diodes at 295 K for Fe-doped InP ($y = 0$) and GaInAsP ($y = 0.57$).

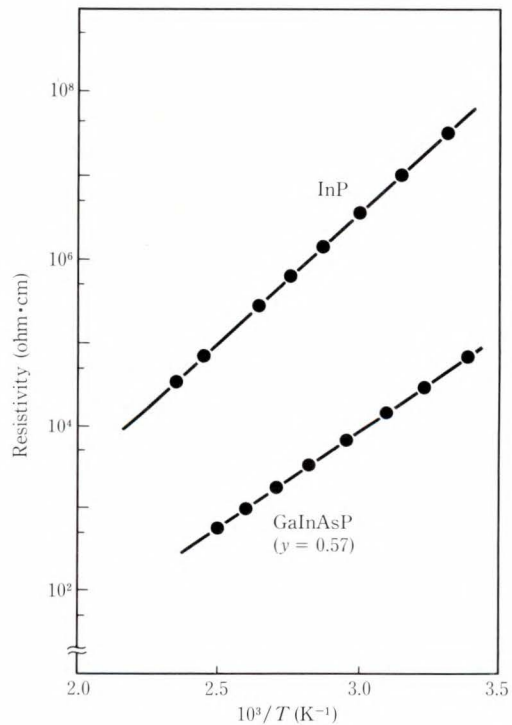


Fig. 11—Temperature dependence of the resistivity for Fe-doped SI InP ($y = 0$) and GaInAsP ($y = 0.57$).

Table 1. Results of the SIMS analysis

Material	T_{growth}	W_{Fe}^I (wt.%)	X_{Fe}^s (cm^{-3})
InP	800	0.1	1.5×10^{15}
	850	0.1	4×10^{15}
	900	0.01	2×10^{15}
	900	0.1	7×10^{15}
	900	1	8×10^{15}
GaInAsP ($y = 0.57$)	750	0.1	2.5×10^{15}
GaInAs ($y = 1$)	750	0.1	3×10^{16}
AlGaInAs ($u = 0.16$)	750	0.01	2×10^{15}
	750	0.05	9×10^{15}
AlGaInAs ($u = 0.04$)	750	0.03	8×10^{15}
AlGaInAs ($u = 0.36$)	750	0.03	6×10^{15}
AlInAs ($u = 0.48$)	750	0.03	5×10^{15}

SI InP ($y = 0$) and GaInAsP ($y = 0.57$) are shown in Fig. 11. This resistivity was near the maximum resistivity for each material. The activation energy of resistivity for InP ($y = 0$) and GaInAsP ($y = 0.57$) were 0.62 eV and 0.47 eV, respectively, whereas the activation energies of resistivity for SI AlGaInAs with an aluminum content of 0.04, 0.16, and 0.36 were 0.35 eV, 0.52 eV, and 0.78 eV, respectively.

3.4 Fe distribution coefficient

The results of SIMS analysis on the Fe-doped InP, $\text{Ga}_x\text{In}_{1-x}\text{As}_y\text{P}_{1-y}$, and $\text{Al}_u\text{Ga}_v\text{In}_{1-u-v}\text{As}$ are shown in Table 1. The Fe concentration in the InP layer increased with the growth temperature or the Fe weight percent in the low doping range, but saturated at 1 wt% Fe in the solution. The Fe concentrations in $\text{Ga}_x\text{In}_{1-x}\text{As}_y\text{P}_{1-y}$ and $\text{Al}_u\text{Ga}_v\text{In}_{1-u-v}\text{As}$ varied with the composition.

The Fe distribution coefficients could be estimated from the results of SIMS analysis in the low doping range, because the Fe concentration obtained from SIMS analysis was nearly proportional to the Fe content in the growth solution. Figure 12 shows the Fe distribution coefficient for InP versus the reciprocal of the growth temperature. The distribution coefficient for InP was about 2×10^{-5} ,

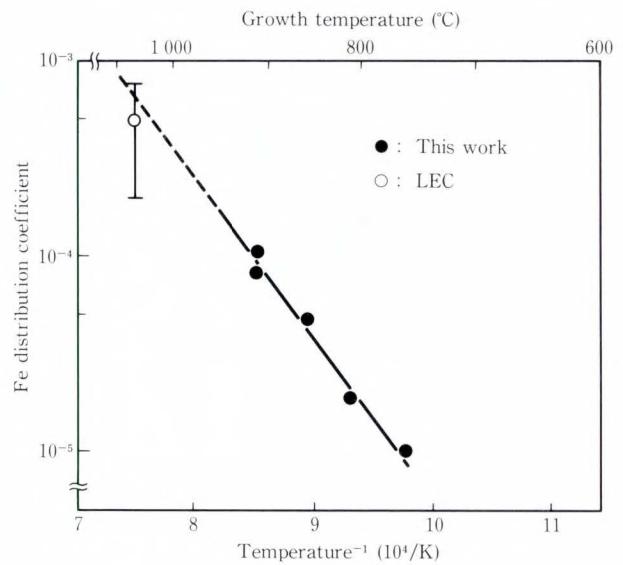


Fig. 12—Temperature dependence of the Fe distribution coefficient for InP.

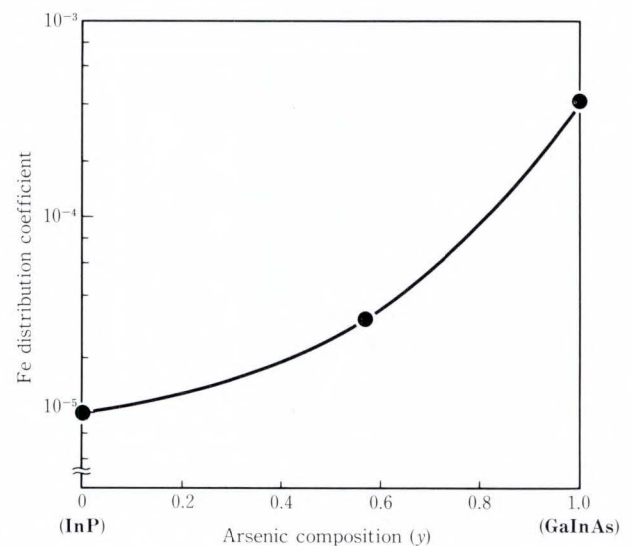


Fig. 13—Composition dependence of the Fe distribution coefficient for $\text{Ga}_x\text{In}_{1-x}\text{As}_y\text{P}_{1-y}$.

5×10^{-5} , and 1×10^{-4} at 800 °C, 850 °C, and 900 °C, respectively. The distribution coefficient at 1070 °C, predicted by extrapolating the line in Fig. 12, agrees well with that reported for LEC grown Fe-doped InP crystals¹⁸⁾.

Figure 13 shows the composition dependence of the distribution coefficient for the $\text{Ga}_x\text{In}_{1-x}\text{As}_y\text{P}_{1-y}$ system (including InP) at

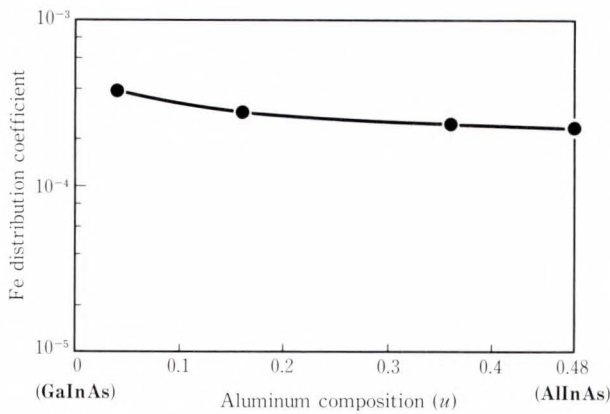


Fig. 14—Composition dependence of the Fe distribution coefficient for $Al_u Ga_y In_{1-u-y} As$.

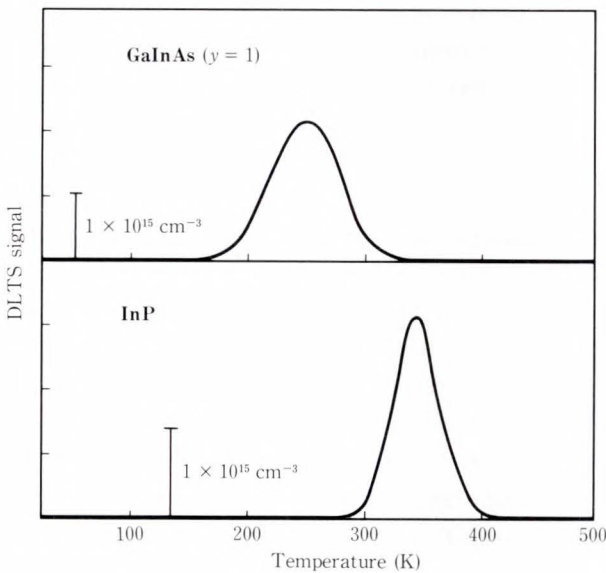


Fig. 15—Typical DLTS spectra of n-type Fe-doped InP ($y = 0$) and GaInAs ($y = 1$).

750 °C. The distribution coefficient was about 1×10^{-5} for InP ($y = 0$), about 3×10^{-5} for GaInAsP ($y = 0.57$), and about 4×10^{-4} for GaInAs ($y = 1$). In particular, the distribution coefficient increases about 40 times as the composition varies from InP ($y = 0$) to GaInAs ($y = 1$).

The Fe distribution coefficient for the $Al_u Ga_y In_{1-u-y} As$ system at 750 °C versus the composition are shown in Fig. 14. The distribution coefficient was about 2 to 4×10^{-4} , and was almost the same for all the composition.

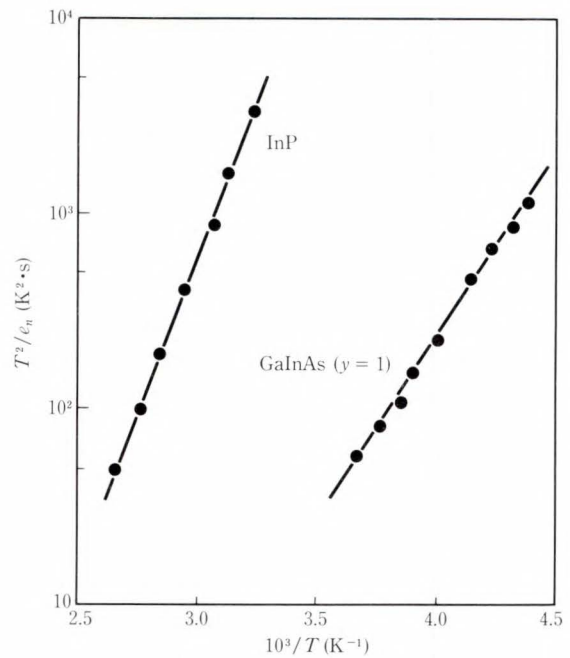


Fig. 16—Plots of $\ln(T^2/e_n)$ versus $1/T$.

3.5 Activation energy of Fe acceptor level

Figure 15 shows a typical DLTS spectra of Fe-doped InP ($y = 0$) and GaInAs ($y = 1$). Capacitance transients caused by electron emission from an impurity level are observed. Since these peaks are not observed in undoped InP ($y = 0$) and GaInAs ($y = 1$), this impurity level can be assigned to the Fe acceptor level. The electron emission rate e_n was measured as a function of temperature in order to obtain the activation energies of this level. Figure 16 shows the plots of $\ln(T^2/e_n)$ versus $1/T$. From the results of this figure, the activation energy was 0.63 eV in InP ($y = 0$) and 0.37 eV in GaInAs ($y = 1$)¹⁵.

4. Discussion

4.1 Fe doping characteristics

There are three factors in determining the Fe doping characteristics in LPE: the Fe solubility in the growth solution, the background electron concentration, and the Fe distribution coefficient. Considering these factors, we shall discuss the temperature dependence of Fe doping characteristics of InP, the composition dependence of Fe doping characteristics of the $Ga_x In_{1-x} As_y P_{1-y}$ system, and the differ-

ence of Fe doping characteristics between the $\text{Ga}_x\text{In}_{1-x}\text{As}_y\text{P}_{1-y}$ and $\text{Al}_u\text{Ga}_v\text{In}_{1-u-v}\text{As}$ system.

4.1.1 Temperature dependence of Fe doping characteristics of InP

Two important points are illustrated in the results of the resistivities of Fe-doped InP shown in Fig. 6. The first is that the maximum resistivity at each growth temperature increase with the growth temperature. The second is that the critical weight percent of Fe where the resistivity of the layer abruptly increased decreases with the growth temperature.

The first point can be explained by the temperature dependence of the Fe solubility in the growth solution. The Fe solubility in an indium solution at each temperature¹⁶⁾ is shown with an arrow in Fig. 6. Each value agrees well with the weight percent of Fe where the resistivity is saturated. This result shows that the Fe solubility in the growth solution for InP is almost the same as that in an indium solution. Therefore, the temperature dependence of the maximum resistivity is caused by the temperature dependence of the Fe solubility in the solution.

At the critical weight percent of Fe, the background electron concentration in the epitaxial layer is nearly equal to the concentration of Fe deep acceptor. Therefore, the second point is due to the strong positive temperature dependence of Fe distribution coefficient, considering that the background electron concentration is almost independent of the growth temperature as shown in Fig. 3. It is concluded that the temperature dependence of Fe doping characteristics of InP is due to the temperature dependence of Fe solubility and distribution coefficient.

4.1.2 Composition dependence of Fe doping characteristics of the $\text{Ga}_x\text{In}_{1-x}\text{As}_y\text{P}_{1-y}$ system

It is clear from Fig. 7 that SI $\text{Ga}_x\text{In}_{1-x}\text{As}_y\text{P}_{1-y}$ is easier to obtain as the composition varies from InP ($y = 0$) to GaInAs ($y = 1$).

The Fe solubility in an indium solution at 750°C ¹⁶⁾ is shown with an arrow in Fig. 7. This value agrees well with the weight percent of Fe

where the resistivities of GaInAsP ($y = 0.57$) and InP ($y = 0$) became saturated. This means that the Fe solubility in the growth solution for $\text{Ga}_x\text{In}_{1-x}\text{As}_y\text{P}_{1-y}$ is the same as that in an indium solution and independent of the composition.

The background electron concentration decreased gradually from InP ($y = 0$) to GaInAs ($y = 1$) as shown in Fig. 4, and the Fe distribution coefficient increased greatly from InP ($y = 0$) to GaInAs ($y = 1$) as shown in Fig. 12. Therefore, the composition dependence of Fe doping characteristics of the $\text{Ga}_x\text{In}_{1-x}\text{As}_y\text{P}_{1-y}$ system is caused by the composition dependence of background electron concentration and Fe distribution coefficient. In particular, the Fe distribution coefficient is a dominant factor.

4.1.3 Comparison of Fe doping characteristics between $\text{Ga}_x\text{In}_{1-x}\text{As}_y\text{P}_{1-y}$ and $\text{Al}_u\text{Ga}_v\text{In}_{1-u-v}\text{As}$ systems

$\text{Ga}_x\text{In}_{1-x}\text{As}_y\text{P}_{1-y}$ and $\text{Al}_u\text{Ga}_v\text{In}_{1-u-v}\text{As}$ systems lattice matched to InP have almost the same energy gap range. It is significant for application to compare the Fe doping characteristics between these two alloy systems. From Figs. 8 and 9, it is found that SI $\text{Al}_u\text{Ga}_v\text{In}_{1-u-v}\text{As}$ is easier to obtain than SI $\text{Ga}_x\text{In}_{1-x}\text{As}_y\text{P}_{1-y}$.

The Fe solubility in an indium solution at 750°C ¹⁶⁾ is shown with an arrow in Fig. 8. It is the same as that in the growth solution for $\text{Ga}_x\text{In}_{1-x}\text{As}_y\text{P}_{1-y}$, as discussed in Subsec. 4.1.2. SI $\text{Al}_u\text{Ga}_v\text{In}_{1-u-v}\text{As}$ can be obtained at the smaller weight percent of Fe than the Fe solubility in the growth solution for $\text{Ga}_x\text{In}_{1-x}\text{As}_y\text{P}_{1-y}$. Therefore, the Fe solubility in the solution does not cause the difference in the doping characteristics.

The background electron concentration in $\text{Al}_u\text{Ga}_v\text{In}_{1-u-v}\text{As}$ is greater than or equal to that in $\text{Ga}_x\text{In}_{1-x}\text{As}_y\text{P}_{1-y}$, as shown in Figs. 4 and 5. Because of this, the background electron concentration does not cause $\text{Al}_u\text{Ga}_v\text{In}_{1-u-v}\text{As}$ to become semi-insulating more easily than $\text{Ga}_x\text{In}_{1-x}\text{As}_y\text{P}_{1-y}$.

Figure 17 shows the Fe distribution coefficient versus the energy gap of the layer for $\text{Ga}_x\text{In}_{1-x}\text{As}_y\text{P}_{1-y}$ and $\text{Al}_u\text{Ga}_v\text{In}_{1-u-v}\text{As}$. It is clear that the Fe distribution coefficient of

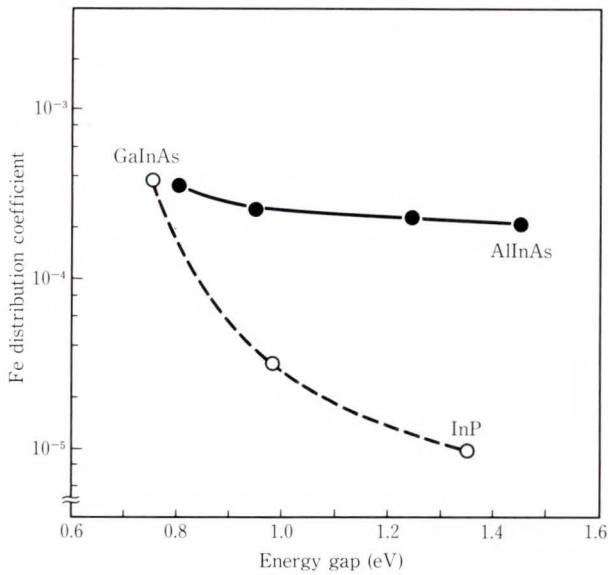


Fig. 17—Fe distribution coefficient versus the energy gap of the layer for $Ga_xIn_{1-x}As_yP_{1-y}$ and $Al_uGa_vIn_{1-u-v}As$.

$Al_uGa_vIn_{1-u-v}As$ is much greater than that of $Ga_xIn_{1-x}As_yP_{1-y}$ at the same energy gap. For example, the Fe distribution coefficient of $AlGaInAs$ ($u = 0.16$) with an energy gap of 0.95 eV is about 3×10^{-4} as shown in Fig. 12, while that of $GaInAsP$ ($y = 0.57$) with the same energy gap is about 4×10^{-5} as shown in Fig. 13. Although the background electron concentration of $AlGaInAs$ ($u = 0.16$) with this energy gap is twice as great as that of $GaInAsP$ ($y = 0.57$) from the results shown in Figs. 4 and 5, the high distribution coefficient of $AlGaInAs$ ($u = 0.16$) can make up for the disadvantage of the background level. As a result, $AlGaInAs$ ($u = 0.16$) can be made semi-insulating for a smaller weight percent of Fe in the growth solution than that for $GaInAsP$ ($y = 0.57$), as shown in Fig. 8. It is concluded that SI $Al_uGa_vIn_{1-u-v}As$ is easier to obtain than SI $Ga_xIn_{1-x}As_yP_{1-y}$, because of the high Fe distribution coefficient.

4.2 Fe acceptor level in $Ga_xIn_{1-x}As_yP_{1-y}$ and $Al_uGa_vIn_{1-u-v}As$ systems

The activation energies of the Fe acceptor level were 0.63 eV in InP ($y = 0$) and 0.37 eV in $GaInAs$ ($y = 1$), from the results of the DLTS measurements in section 3.5.

The activation energies of resistivities

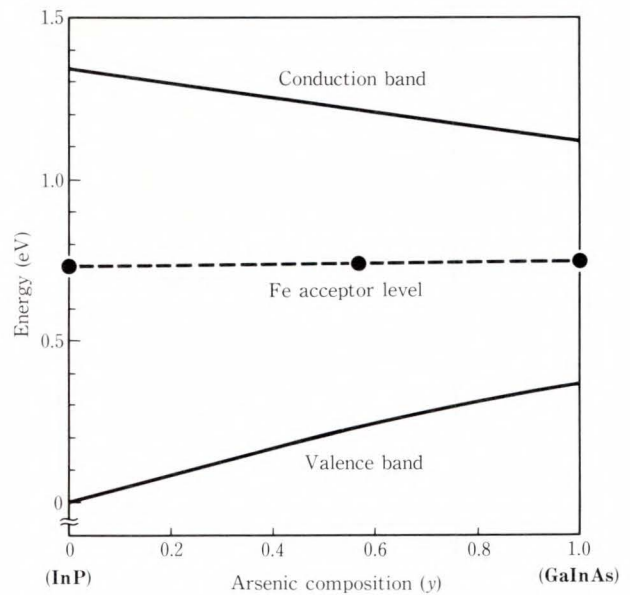


Fig. 18—Activation energy of Fe accepted level in $Ga_xIn_{1-x}As_yP_{1-y}$. The band diagram is described by the results of references 10 and 19.

for Fe-doped SI InP , $Ga_xIn_{1-x}As_yP_{1-y}$, and $Al_uGa_vIn_{1-u-v}As$ were obtained in Sec. 3.3. These activation energies show the locations of the Fermi levels in the forbidden gaps of the materials. Since the temperature dependence of the resistivity was measured for the SI layer whose resistivity was near the maximum resistivity, it is considered that the Fe concentration in the layer was larger than the background electron concentration. Therefore, the Fermi level lies almost at the Fe acceptor level. Namely, the activation energy of the resistivity is almost the same as that of the Fe acceptor level. The activation energy of 0.62 eV for InP obtained from the temperature dependence of resistivity agrees well with the value obtained by DLTS measurement. Figures 18 and 19 show the activation energies of the Fe acceptor level in $Ga_xIn_{1-x}As_yP_{1-y}$ and $Al_uGa_vIn_{1-u-v}As$, respectively. The band diagram of $Ga_xIn_{1-x}As_yP_{1-y}$ shown in Fig. 18 is described by using the composition dependence of energy gap reported by R.E. Nahory et al.¹⁰, and the band-edge discontinuity measured by S.R. Forrest et al.¹⁹. The band diagram of $Al_uGa_vIn_{1-u-v}As$ in Fig. 19 is described by using the results of references 11

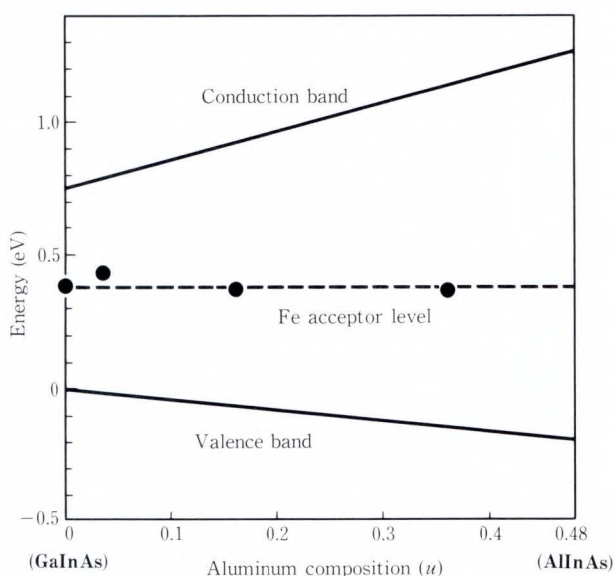


Fig. 19—Activation energy of Fe acceptor level in $Al_uGa_vIn_{1-u-v}As$. The band diagram is described by the results of references 11 and 20.

and 20.

The activation energy of Fe acceptor level in $Ga_xIn_{1-x}As_yP_{1-y}$ decreased as the arsenic content increased and that in $Al_uGa_vIn_{1-u-v}As$ increased as the aluminum content increased. An important point is that, for both systems, the Fe acceptor level is aligned at a constant energy relative to the vacuum level, though the activation energy depends on the composition. This agrees well with the vacuum-referred binding energy (VRBE) model²¹⁾.

5. Conclusion

Fe-doped InP, $Ga_xIn_{1-x}As_yP_{1-y}$, and $Al_uGa_vIn_{1-u-v}As$ grown by liquid phase epitaxy were extensively studied. The temperature, composition, and material dependence of Fe doping characteristics of these materials are well explained by three factors: the Fe solubility in the growth solution, the background electron concentration, and the Fe distribution coefficient. The high resistivities of 8×10^7 ohm·cm, 2×10^5 ohm·cm, and 1×10^9 ohm·cm were obtained for InP grown at 900 °C, $Ga_{0.26}In_{0.74}As_{0.57}P_{0.43}$ and $Al_{0.48}In_{0.52}As$ grown at 750 °C, respectively.

The activation energies of the Fe acceptor

levels in $Ga_xIn_{1-x}As_yP_{1-y}$ and $Al_uGa_vIn_{1-u-v}As$ systems were also studied. It was found that the Fe acceptor level is aligned at a constant energy relative to the vacuum level for both alloy systems.

References

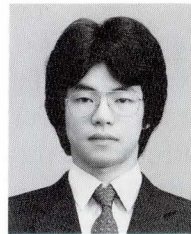
- 1) Dutta, N.K., Zilko, J.L., Cella, T., Ackerman, D.A., Shen, T.M., and Napholz, S.G.: InGaAsP Laser with Semi-Insulating Current-Confining Layers. *Appl. Phys. Lett.*, **48**, 23, pp. 1572-1573 (June, 1986).
- 2) Sanada, T., Nakai, K., Wakao, K., Kuno, M., and Yamakoshi, S.: Planer-Embedded InGaAsP/IrrP Heterostructure Laser with a Semi-Insulating InP Current-Blocking Layer Grown by Metalorganic Chemical Vapor Deposition. *Appl. Phys. Lett.*, **51**, 14, pp. 1054-1056 (Oct., 1987).
- 3) Mizuno, O., and Watanabe, H.: Semi-Insulating Properties of Fe-Doped InP. *Electron Lett.*, **11**, 5, pp. 118-119 (March, 1975).
- 4) Long, L.A., Riggs, V.G., and Johnston, Jr., W.D.: Growth of Fe-Doped Semi-Insulating InP by MOCVD. *J. Cryst. Growth*, **69**, 1, pp. 10-14 (Nov., 1984).
- 5) Hess, K.L., Zehr, S.W., Cheng, W.H., and Perrachione, D.: Semi-Insulating InP Grown by Low Pressure MOCVD. *J. Electron. Mate.*, **16**, 2, pp. 127-131 (March, 1987).
- 6) Nakai, K., Ueda, O., Odagawa, T., Takanohashi, T., and Yamakoshi, S.: Epitaxial Growth and Characteristics of Fe-Doped InP by MOCVD. GaAs and Related Compounds, 1987, Crete.
- 7) Kondo, M., Sugawara, M., Yamaguchi, A., Tanahashi, T., Isozumi, S., and Nakajima, K.: Liquid phase Epitaxial Growth of Fe-Doped Semi-Insulating InP. Extended Abstracts of the 18th Conference on Solid State Devices and Materials, Tokyo, Business Center for Academic Societies Japan, 1986, pp. 627-630.
- 8) Kondo, M., Sugawara, M., Tanahashi, T., Isozumi, S., and Nakajima, K.: LPE Growth of Fe-Doped Semi-Insulating InGaAsP. submitted to *Appl. Phys. Lett.*
- 9) Tanahashi, T., Okuda, S., Kondo, S., Sugawara, M., Isozumi, S., and Nakajima, K.: Liquid Phase Epitaxial Growth of Semi-Insulating AlGaInAs by Fe Doping. Material Research Society 1987 Fall Meeting, Tung, R.T., Dawson, L.R., Gunshor, R.L., ed., Symp. Proc., 102, to be published.
- 10) Nahory, R.E., Pollack, M., A., Johnston Jr., W.D., and Barns, R.L.: Band Gap Versus Composition and

- Demonstration of Vegard's Law for $\text{In}_{1-x}\text{Ga}_x\text{As}_y\text{P}_{1-y}$ Lattice Matched to InP. *Appl. Phys. Lett.*, **33**, 7, pp. 659-661, (Oct., 1978).
- 11) Olego, D., Chang, T.Y., Silberg, E., Caridi, E.A., and Pinczuk, A.: Compositional Dependence of Band-Gap Energy and Conduction-Band Effective Mass of $\text{In}_{1-x-y}\text{Ga}_x\text{Al}_y\text{As}$ Lattice Matched to InP. *Appl. Phys. Lett.*, **41**, 5, pp. 476-478 (Sep., 1982).
 - 12) Tanahashi, T., Nakajima, K., Yamaguchi, A., and Umebu, I.: Electrical Properties of Undoped and Si-Doped $\text{Al}_{0.48}\text{In}_{0.52}\text{As}$ Grown by Liquid Phase Epitaxy, *Appl. Phys. Lett.*, **43**, 11, pp. 1030-1032 (Dec., 1983).
 - 13) Kuphal, E., and Pöcker, A.: LPE Growth of High Purity InP and $\text{In}_{1-x}\text{Ga}_x\text{P}_{1-y}\text{As}_y$. *J. Cryst. Growth*, **58**, 1, pp. 133-142 (June, 1982).
 - 14) Sugawara, M., Aoki, O., Nakai, K., Tanaka, Yamaguchi, A., and Nakajima, K.: I-V Characteristics of Semi-Insulating InP Epitaxial Layers: Application to Buried Heterostructure Lasers. Semi-Insulating III-V Materials, Kukimoto, H. and Miyazawa, S., ed., Tokyo, Ohmsha, 1986, pp. 597-602.
 - 15) Sugawara, M., Kondo, M., Takanohashi, T., and Nakajima, K.: Fe Acceptor Level in $\text{In}_{1-x}\text{Ga}_x\text{As}_y\text{P}_{1-y}$ /InP. *Appl. Phys. Lett.*, **51**, 11, pp. 834-836 (Sep., 1987).
 - 16) Messham, R.L., Majerfeld, A. and Bachmann, K.J.: LPE and Bulk Growth and Electrical Properties of Fe-, Cr-, and Co-Doped InP. Semi-Insulating III-V Materials, Makram-Ebeid, S. and Tuck, B., ed., Evian, Shiva Publishing Ltd., 1982, pp. 75-77.
 - 17) Sugawara, M., Kondo, M., Nakai, K., Yamaguchi, A., and Nakajima, K.: Activation Ratio of Fe in Fe-Doped Semi-Insulating InP Epitaxial Layers Grown by Liquid Phase Epitaxy and Metalorganic Chemical Vapor Deposition. *Appl. Phys. Lett.*, **50**, 20, pp. 1432-1434 (May, 1987).
 - 18) Zeisse, C.R., Antypas, G.A., and Hopkins, S.: Electron and Iron Concentration in Semi-Insulating Indium Phospide. *J. Cryst. Growth*, **64**, 2, pp. 217-221 (Nov., 1983).
 - 19) Forrest, S.R., Schmidt, P.H., Wilson, R.B., and Kaplan, M.L.: Relationship Between the Conduction-Band Discontinuities and Band-Gap Differences of InGaAsP/InP Heterojunctions. *Appl. Phys. Lett.*, **45**, 11, pp. 1199-1201 (Dec., 1984).
 - 20) Sugiyama, Y., Inata, T., Fujii, T., Nakata, Y., Muto, S., and Hiyamizu, S.: Conduction Band Edge Discontinuity of $\text{In}_{0.52}\text{Ga}_{0.48}\text{As}/\text{In}_{0.52}(\text{Ga}_{1-x}\text{Al}_x)_{0.48}\text{As}$ ($0 \leq x \leq 1$) Heterostructures. *Jpn. J. Appl. Phys.*, **25**, 8, pp. L648-L650 (Aug., 1986)
 - 21) Caldas, M.J., Fazzio, A., and Zunger A.: A Universal Trend in the Binding Energies of Deep Impurities in Semiconductors. *Appl. Phys. Lett.*, **45**, 6, pp. 671-673 (Sep., 1984).



Toshiyuki Tanahashi

Optical Semiconductor Devices
Laboratory
FUJITSU LABORATORIES, ATSUGI
Bachelor of Physics
The University of Tokyo 1976
Master of Physics
The University of Tokyo 1978
Specializing in Optical Semiconductor
Devices



Mitsuru Sugawara

Optical Semiconductor Devices
Laboratory
FUJITSU LABORATORIES, ATSUGI
Bachelor of Applied Physics
The University of Tokyo 1982
Master of Physical Eng.
The University of Tokyo 1984
Specializing in Optical Semiconductor
Materials



Makoto Kondo

Optical Semiconductor Devices
Laboratory
FUJITSU LABORATORIES, ATSUGI
Bachelor of Electrical Eng.
Kyoto University 1982
Master of Electrical Eng.
Kyoto University 1984
Specializing in Optical Semiconductor
Materials

Fe-50%Co Sintered Alloy for Magnetic Circuit Yoke

• Wataru Yamagishi • Tsutomu Iikawa

(Manuscript received March 31, 1988)

To produce a soft magnetic Fe-50%Co alloy using powder metallurgy, a study was made on the effects of various starting powders on the sintered density and magnetic properties of this alloy. An Fe-50%Co sintered alloy with a relative density of 95 percent and a magnetization of 2.15 T in a magnetic field of 4 kA/m was obtained using pre-alloyed Fe-20%Co and -400 mesh pure Co powders as the starting powders. This sintered alloy was used in a 24-wire-dot matrix printer. This printer operated at a printing speed of 110 cps (for Japanese character "kanji" printing) due to the higher magnetization afforded by the Fe-50%Co sintered alloy.

1. Introduction

In 1926, Elmen¹⁾ invented the Fe-50%Co (all percentages in this paper are based on mass) "Permendur" alloy. This alloy has the highest saturation magnetization of all ferromagnetic materials. By using this alloy, it was possible to develop higher performance and smaller size electro-magnetic components such as magnetic circuit cores and yokes.

However, the fabrication of Fe-50%Co alloy into various forms was very difficult because of its brittleness. To make this material less brittle, White and Wahl²⁾ introduced the 2%V-49%Fe-Co alloy in 1932. Nearly fifty years have passed since its introduction, and its application is still limited to a few special cases. This may be attributed to the low workability due to the material's inherent brittleness and the high cost of cobalt.

Powder metallurgy is suitable for materials of low workability, such as Fe-50%Co alloy, to produce near-net shape parts. However, very little work has been done in the field of Fe-Co sintered alloys. This is probably due to the difficulty in obtaining a high density sintered alloy using a mixture of pure Fe and Co powders. The reason for this difficulty is that

the difference in Fe and Co diffusion coefficients causes the formation of Kirkendall voids during sintering.

This paper presents the results of our research on the sintering behavior of Fe-50%Co alloy based on our investigation of the sintered density of samples that use pre-alloyed Fe-Co powders of various Co content, and Co or Fe powder of different particle sizes. This paper also describes the magnetic properties and microstructures of the resulting Fe-50%Co sintered alloys, and the application of this sintered alloy for the magnetic circuit yoke of the print head used in a 24-wire-dot matrix printer.

2. Experimental procedure

Table 1 lists the starting powders. Water-

Table 1. Starting powders

Starting powders	Fabrication	Particle size (mesh)
Pre-alloyed Fe-x%Co*	Water-atomized	-325
Fe	Electrolytic	-325, -400
Co	Reduced	-325, -400

* x = 10-90

atomized -325 mesh pre-alloyed Fe- x %Co powders ($x = 10-90$), reduced Co powder (-325 and -400 mesh), and an electrolytic Fe powder (-325 and -400 mesh) were used. These powders were mixed to obtain a composition of Fe-50%Co. For example, when the pre-alloyed Fe-20%Co powder was used, pure Co powder was added to obtain a composition of Fe-50%Co. The mixture of Fe-50%Co composition was compacted into a 45/35 mm by 7 mm thick ring under a compacting pressure of 390 MPa. The samples were then presintered and compacted again. Finally, these samples were sintered for 1 h at 1400 °C in a dry hydrogen atmosphere.

The green density was calculated from the size and weight of the compacted ring samples. The sintered density was measured according to the Archimedes method. The relative density was calculated as the ratio of green and sintered density to the theoretical density³⁾.

Ring sample magnetic properties, such as magnetization (B_{4k}), coercive force (H_c) and maximum permeability (μ_m) were measured using a DC magnetic hysteresis loop tracer in a magnetic field of 4 kA/m.

The microstructures were studied using an optical microscope and an electron probe microanalyzer.

Finally, the sintered alloy was applied to a magnetic circuit yoke of a print head in a 24-wire-dot matrix printer. The printing force and printing speed were then studied.

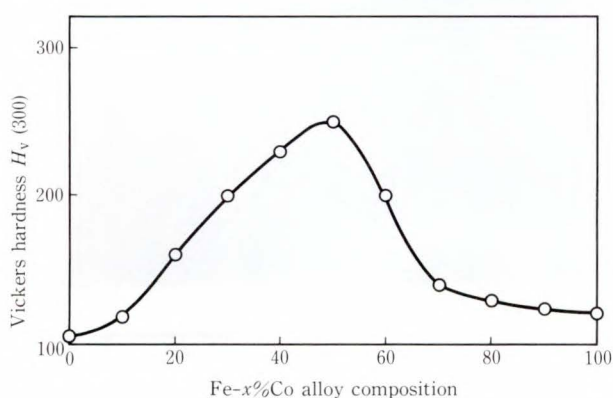


Fig. 1—Hardness of Fe-Co binary alloy.

3. Results and discussion

3.1 Sintering behavior

Figure 1 shows the hardness of the Fe-Co binary alloy. Maximum hardness is obtained with a Co content of 50 percent. This may be due to the ordering in this alloy⁴⁾.

Figure 2 shows the effect of the Co composition (x) of pre-alloyed Fe- x %Co powders on the green densities for the Fe-50%Co compacted samples. In this figure, $x = 0$ is for the sample that uses a mixture of pure Fe and Co powders. The value at $x = 50$ is for the sample that uses pre-alloyed Fe-50%Co powder only. However, this pre-alloyed powder was too hard (as shown in Fig. 1) to be compacted. The green densities increase as the content of pure Fe or Co powders increases. In other words, the green densities are affected by both the hardness of the pre-alloyed Fe-Co powder and the content of pure Fe or Co powder in the mixtures. Conversely, the green densities are also affected by Fe and Co powder particle size. This is probably because finer Fe and Co powders are more suitable for packing with the coarser pre-alloyed Fe- x %Co powders.

Figure 3 shows the effect of the Co composition (x) of pre-alloyed Fe- x %Co powder on the sintered densities for the Fe-50%Co sintered alloy. In this figure, $x = 0$ and $x = 50$ are the

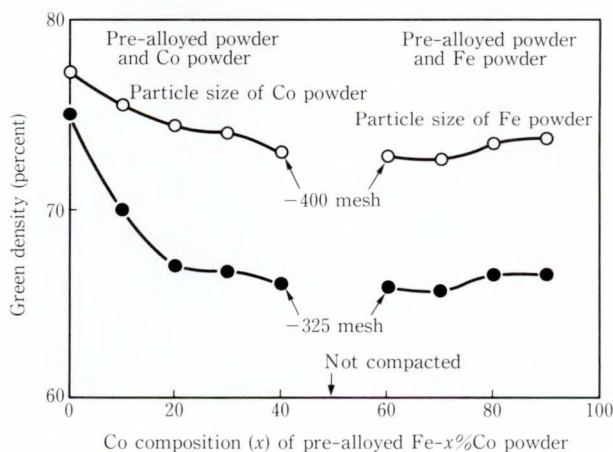


Fig. 2—Effect of Co composition (x) of pre-alloyed Fe- x %Co powder on green densities for Fe-50%Co compacted samples.

same as in Fig. 2. The sintered densities are greatly affected by the Fe and Co powder particle size. This is probably because the finer Fe and Co powder particles are more active during sintering. However, a poor correlation between the green densities in Fig. 2 and sintered densities in Fig. 3 is observed. The reason for this is

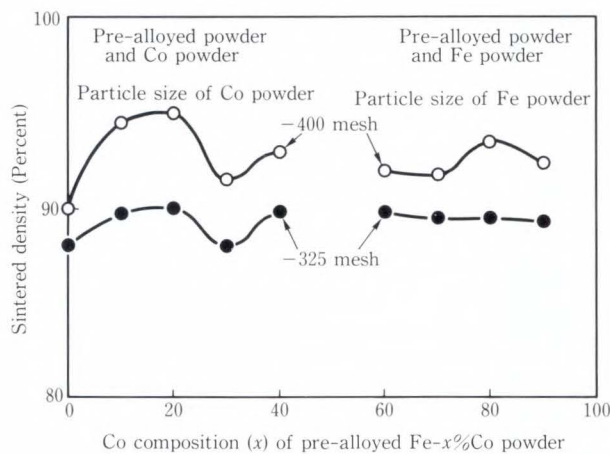


Fig. 3—Effect of Co composition (x) of pre-alloyed Fe- x %Co powder on sintered densities for Fe-50%Co sintered alloy.

assumed to be that the interdiffusion between the pre-alloyed Fe- x %Co and Co powders depends on the crystal structure of pre-alloyed Fe- x %Co powder. In other words, the anomalous behavior (for $x = 30$ and $x = 70$ in Fig. 3) corresponds to the formation of an ordered structure based on the Fe_3Co and $FeCo_3$ composition. It is currently difficult to account for these experimental results. Further detailed experiments on this point should be conducted. The maximum value of the sintered densities is found in the sample that uses the pre-alloyed Fe-20%Co and -400 mesh Co powders. Generally, the magnetic properties of sintered magnetic materials, B_{4k} in particular, depend on the sintered density. Therefore, this discussion focuses on a comparison between the sample that uses pre-alloyed Fe-20%Co and -400 mesh Co powders and the sample that uses -400 mesh pure Fe and Co powders.

Figure 4 shows cross-sectional views of the samples that use:

- a) Pre-alloyed Fe-20%Co and -400 mesh Co powders, and
- b) -400 mesh pure Fe and Co powders.

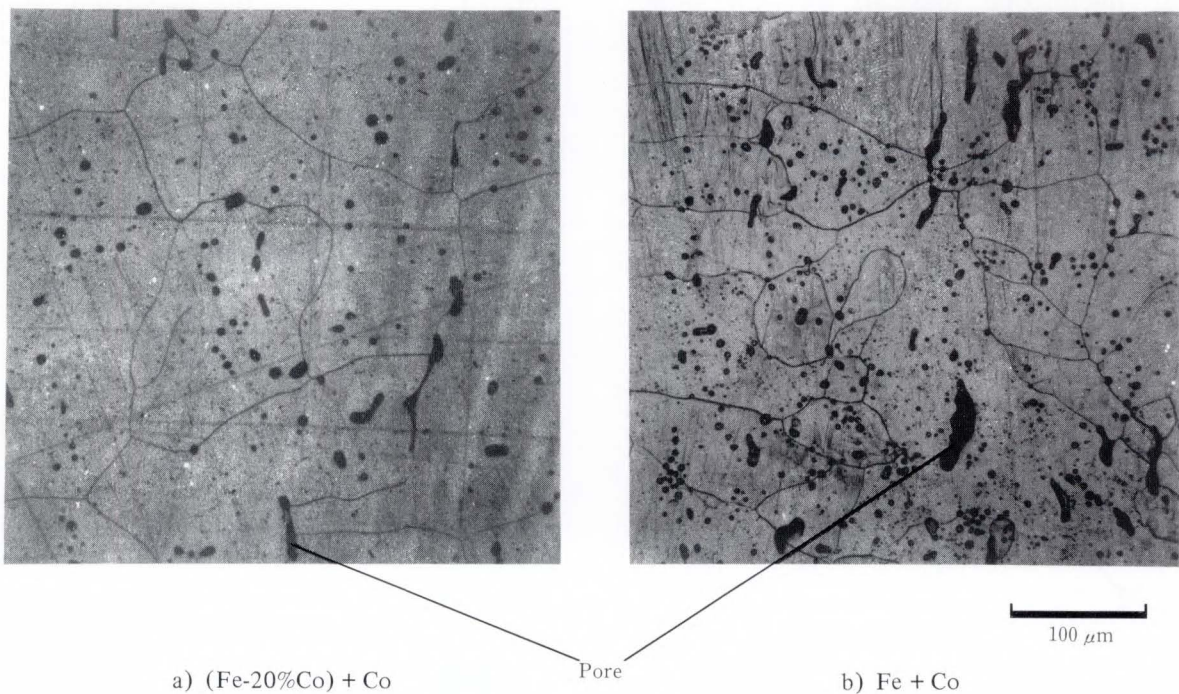


Fig. 4—Microstructures.

The pore size and pore densities in a) are smaller and fewer than those in b). This suggests that the sintering process for each sample is different.

Figure 5 shows the relationship between the sintering temperature and sintered density of the sample that uses a mixture of pre-alloyed Fe-20%Co and -400 mesh Co powders, as compared to that of the sample that uses a mixture of -400 mesh pure Fe and Co powders. In the sample that uses the pre-alloyed powder, the sintered density increases abruptly at temperatures between 400 °C and 600 °C. In comparison, similar behavior is not observed in the sample that uses a mixture of pure Fe

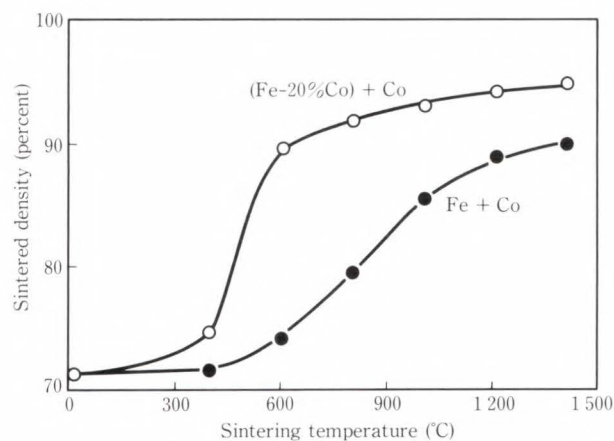
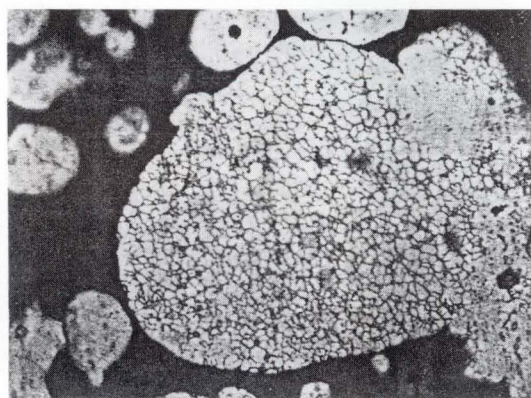
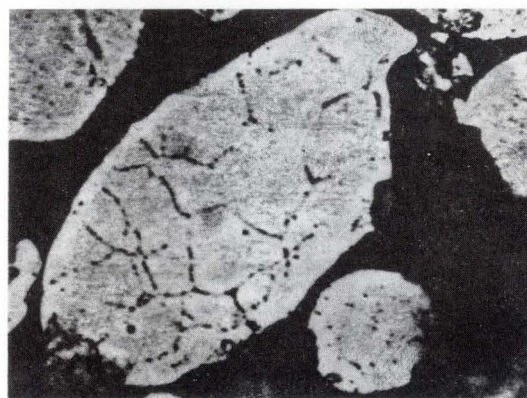


Fig. 5—Relationship between sintering temperature and sintered density.



a) Pre-alloyed Fe-20%Co powder



b) Pure Fe powder

20 μm

Fig. 6—Microstructures of pre-alloyed Fe-20%Co powder and pure Fe powder.

and Co powders.

Figure 6 shows photomicrographs of the grain boundaries of the pre-alloyed Fe-20%Co powder and -400 mesh pure Fe powder. Note that the pre-alloyed Fe-20%Co powder has more grain boundaries than the pure Fe powder. Grain boundaries are generally thought to promote the elimination of pores and Kirkendall voids. This may affect the sintering of the sample that uses a mixture of pre-alloyed Fe-20%Co and -400 mesh Co powders in the early stages at temperatures between 400 °C and 600 °C. Therefore, the sintered density of the sample that uses a mixture of pre-alloyed Fe-20%Co and -400 mesh Co powders is higher than that of the sample that uses -400 mesh pure Fe and Co powders.

3.2 Sintered densities and magnetic properties

Figure 7 shows the effect of the Co composition (x) of the pre-alloyed Fe- x %Co powder on the magnetic properties of the Fe-50%Co sintered alloy that uses a mixture of pre-alloyed Fe-Co powder and -400 mesh Fe or Co powder. In this figure, $x = 0$ and $x = 50$ are the same as in Fig. 2. B_{4k} reaches a maximum of 2.15 T for the sample that uses pre-alloyed Fe-20%Co and -400 mesh Co powders. This corresponds to the behavior of the sintered density shown in Fig. 3. Moreover, this sample has the optimal H_c

and μ_m values of all samples.

Figure 8 shows the relationship between the sintered density and B_{4k} for the sample that uses a mixture of pre-alloyed Fe-20%Co

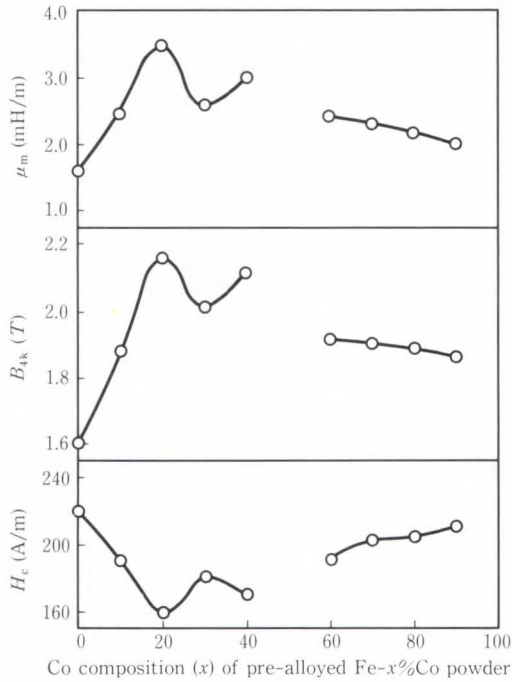


Fig. 7—Effect of Co composition (x) of pre-alloyed Fe- x %Co powder on magnetic properties for Fe-50%Co sintered alloy.

and -400 mesh Co powders, as compared to that of the sample that uses a mixture of -400 mesh pure Fe and Co powders. The sample that uses the pure powders has a B_{4k} of 1.6 T at a sintered density of 90 percent. Theoretically, if the sintered density of this sample were 95 percent, its B_{4k} would be 1.68 T. For comparison, the sample that uses the pre-alloyed powder has a B_{4k} of 2.15 T at a sintered density of 95 percent. This difference suggests that factors other than sintered

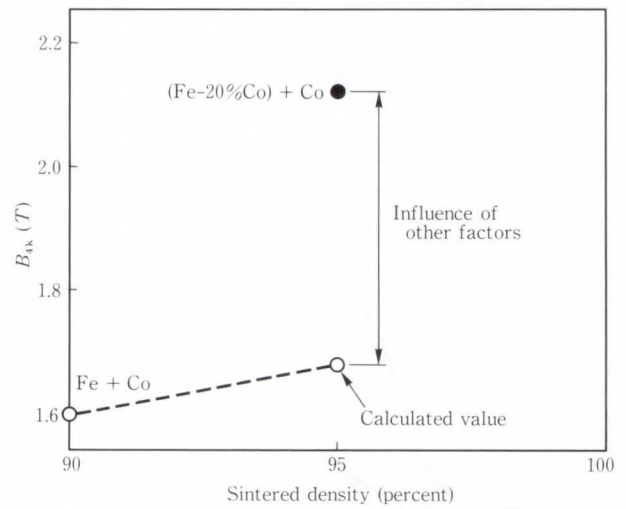
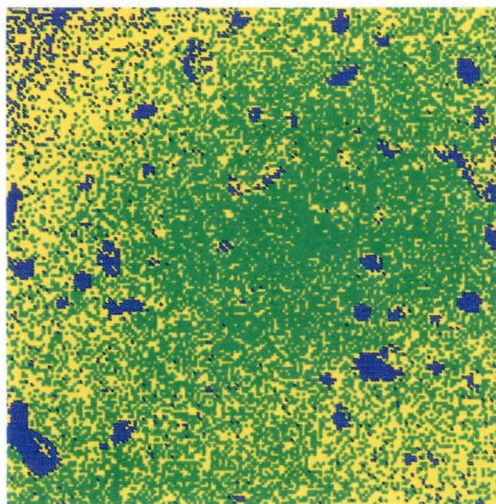
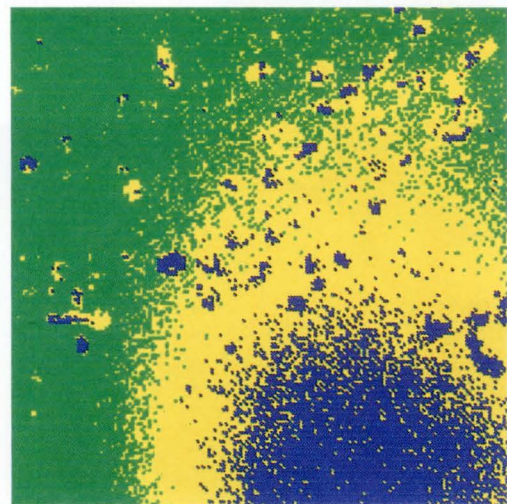


Fig. 8—Relationship between sintered density and B_{4k} .

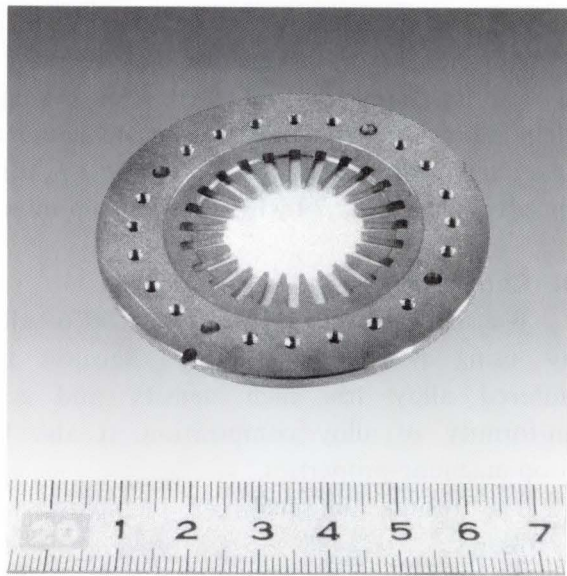


a) (Fe-20%Co) + Co

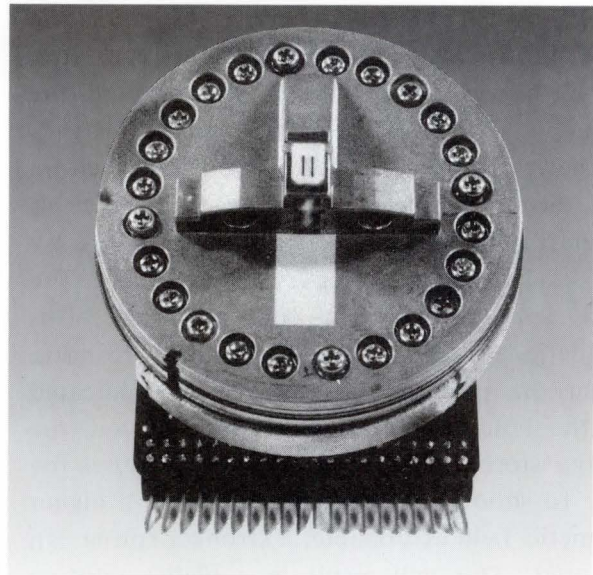


b) Fe + Co

Fig. 9—Concentration maps.



a) Magnetic yoke



b) Print head

Fig. 10—Print head yoke and head.

density affect magnetization. These factors, apart from sintered density, may include the degree of uniform Fe-50%Co alloy composition, order-disorder transformations, and a residual γ phase⁵). Here, we will discuss the uniformity of the alloy composition based on the results of electron microprobe analysis.

Figure 9 shows the concentration maps of the characteristic X-ray of Fe for the samples in Fig. 8. In this figure, the green region corresponds to the composition near Fe-50%Co, the yellow region corresponds to the Fe-rich parts, and the blue region corresponds to the Fe-poor parts and pores. The alloy composition of the sample that uses pre-alloyed powder is much more uniform than that of the sample that uses pure powders. This is the main reason why the sample that uses pre-alloyed Fe-20%Co and -400 mesh Co powder has the highest magnetization of all samples. Consequently, it was found that the pre-alloyed powder technique is an effective means of obtaining good uniformity in alloy composition. However, such good uniformity in alloy composition does not account for all of the high magnetization of this sintered alloy. Further investigation into the order-disorder transformations and

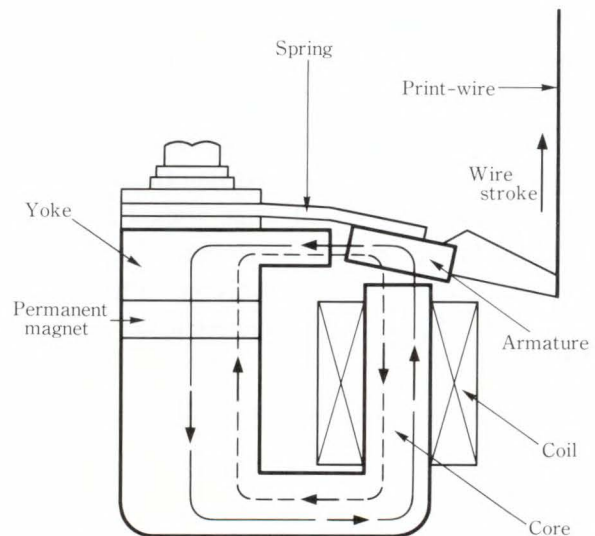


Fig. 11—Print head scheme.

behavior of the γ phase in this sintered alloy should be conducted.

3.3 Application in a print head

This sintered alloy was used in the magnetic circuit yoke of the print head of a 24-wire-dot matrix printer. Figure 10 shows the part that uses the sintered Fe-50%Co alloy, and also shows the print head.

Figure 11 shows the arrangement of the print head of the 24-wire-dot matrix printer. The print-wire is fixed to an armature and the spring system is normally retracted by a magnetic attractive force between the armature and core. This magnetic attractive force is generated by the magnetic field (indicated by the dashed line), of the permanent magnet. The field flows through the core and yoke. This magnetic attractive force holds the wire back. When the opposing magnetic field (indicated by the bold line) is induced by the coil, the energy stored in the retracted spring causes the wire to shoot forward. Accordingly, if a higher magnetic field is possible, a stronger spring can be used. This will result in a higher printing speed.

Figure 12 shows the magnetic attractive force versus the wire stroke of the print head that uses the Fe-50%Co sintered alloy, as compared to that of the Fe-3%Si sintered alloy. The Fe-3%Si alloy is normally used for magnetic circuit yoke and cores. The Fe-3%Si sintered alloy used in this study has a B_{4k} of 1.6 T, H_c of 35 A/m, and μ_m of 22.5 mH/m. For each wire stroke, the magnetic attractive force of the print head that uses Fe-50%Co sintered alloy is larger than that of the print head that uses Fe-3%Si sintered alloy. This is due to the higher magnetization of the

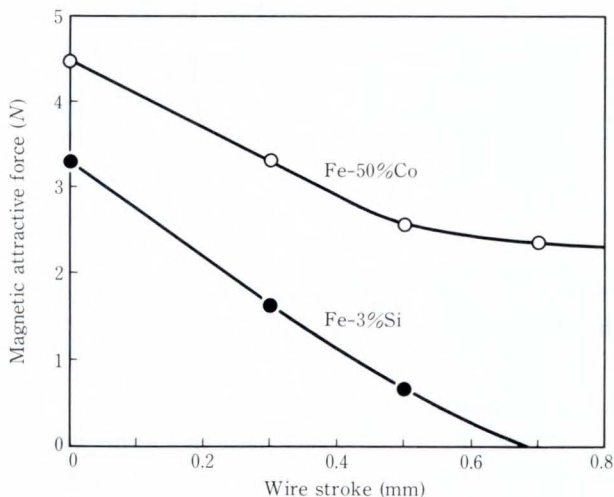


Fig. 12—Magnetic attractive force vs. wire stroke.

Fe-50%Co sintered alloy.

As a result, the printer was able to print at a printing speed of 110 cps for “kanji” character printing, and 330 cps for alphanumeric character printing. These are the fastest printing speeds to date for a 24-wire-dot matrix printer.

4. Conclusion

We have developed an Fe-50%Co alloy by using powder metallurgy. Because this sintered alloy has high density and good uniformity of alloy composition, it also has good magnetic properties.

The results obtained can be summarized as follows:

- 1) A mixture of pre-alloyed Fe-20%Co and fine Co powder is very effective for fabricating Fe-50%Co alloys by powder metallurgy. This is partly due to the lower hardness of Fe-20%Co powder when compared to other Fe-x%Co powders, which makes it suitable for packing; and partly due to the higher grain boundary density of pre-alloyed powder, which accelerates sintering and promotes the elimination of pores and Kirkendall voids. The fine Co powder is also more active during sintering. The pre-alloyed powder technique plays an important role in obtaining good uniformity of alloy composition. This sintered alloy exhibits a relative density of 95 percent and a B_{4k} of 2.15 T, which makes it applicable for development of higher performance and smaller size electro-magnetic components.
- 2) This sintered alloy was used in the magnetic circuit yoke of the print head of a 24-wire-dot matrix printer. The printer operated at a high printing speed of 110 cps for “kanji” character printing due to the high magnetization of the Fe-50%Co sintered alloy.

References

- 1) Elmen, G.W.: Magnetic material and appliance. U.S.P. 1, 739, 752 (1929).
- 2) White, J.H., and Wahl, C.V.: Workable magnetic compositions containing principally iron and cobalt. U.S.P. 1, 862, 559 (1932).

- 3) Bozorth, R.M.: Ferromagnetism, D. Van Nostrand Company INC. Princeton, pp. 190-209 (1951).
- 4) Hansen, M.: Constitution of Binary Alloys. McGraw-Hill, 2nd ed., New York, pp. 471-474 (1958).
- 5) Jesso, E.: Iron-Cobalt-Vanadium Alloys: A Critical Study of the Phase Diagrams in Relation to Magnetic Properties. *IEEE Trans. Magn.*, **MAG-10**, pp. 161-165 (1974).



Wataru Yamagishi

Inorganic Materials Laboratory
FUJITSU LABORATORIES, ATSUGI
Bachelor of Precision Eng.
Hokkaido University 1976
Specializing in Powder Metallurgical
Materials



Tsutomu Iikawa

Inorganic Materials Laboratory
FUJITSU LABORATORIES, ATSUGI
Bachelor of Metallurgical Eng.
Tohoku University 1971
Specializing in Powder Metallurgical
Materials

Overseas Offices

Abu Dhabi Office

8th Floor, A1 Masood Tower,
P.O. Box 322, Abu Dhabi, U.A.E.

Algiers Office

6, Boulevard Colonel,
Amirouche, Alger, Algeria
Telephone: (213)-63-42-55
Telex: 408-67522

Amman Office

P.O. Box 5420, Ammán, Jordan
Telephone: (962-6)-662417

Bangkok Office

Room 405, 4th Floor, Dusit
Thani Bldg., 1-3, Rama IV,
Bangkok, Thailand
Telephone: (66-21)-236-7930
Telex: 86-87956

Beijing Office

Room 1601, Lubao Dasha
Jiangoumen-wai Dajie, Beijing,
People's Republic of China
Telephone: (86-1)-512-3610
Telex: 85-22405

Bogotá Office

Cra. 13 No. 27-50,
Edificio Centro Internacional
Tequendama, Oficina No. 326.
Bogotá, D.E. Colombia
Telephone: (57-1)-296-8258
Telex: 35-45408

Hawaii Branch

6660 Hawaii Kai Drive, Honolulu,
HI 96825, U.S.A.
Telephone: (1-808)-395-2314
Telex: 705-7430204

Indonesia Project Office

16th Floor, Skyline Bldg.,
Jalan M.H. Thamrin No. 9,
Jakarta, Indonesia
Telephone: (62-21)-3105981
Telex: 73-61144

Jakarta Office

16th Floor, Skyline Bldg.,
Jalan M.H. Thamrin No. 9,
Jakarta, Indonesia
Telephone: (62-21)-333245
Telex: 73-61144

Kuala Lumpur Office

Letter Box No. 47, 22nd Floor,
UBN Tower No. 10, Jalan P.
Ramlee, 50250, Kuala Lumpur,
Malaysia
Telephone: (60-3)-238-4870
Telex: 84-31005

London Office

2, Longwalk Road, Stockley Park,
Uxbridge, Middlesex, UB11 1AB,
England
Telephone: (44-1)-573-4444
Telex: 51-263871

Munich Office

c/o D V4 Siemens AG, Otto-
Hahn-Ring 6, D-8000, München
83, F.R. Germany
Telephone: (49-89)-636-3244
Telex: 41-5210935

New Delhi Office

Flat No. 517-B, 5th Floor, World
Trade Centre, Barakhamba Lane,
New Delhi, 110001, India
Telephone: (91-11)-331-1311
Telex: 31-65271

New York Office

680 Fifth Avenue, New York,
N.Y. 10019, U.S.A.
Telephone: (1-212)-265-5360
Telex: 23-234969

Paris Office

Batiment Aristote,
Rue Olof Palme 94006,
Creteil Cedex, France
Telephone: (33-1)-4-399-0897
Telex: 42-262661

Shanghai Office

Room 1504 Ruijin Bldg.,
205 Maoming Road South,
Shanghai, People's Republic
of China
Telephone: (86-21)-336-462
Telex: 30180

Taipei Office

Sunglow Bldg. 66, Sung Chiang
Road, Taipei, Taiwan
Telephone: (886-2)-561-7715
Telex: 785-26773

Overseas Subsidiaries

		Telephone	Telex
FKL Dong-Hwa Ltd.	338-13, Dae Hong-Ri, Sunghwan-Eub, Chunwon-Gun, Chungnam, Republic of Korea	(82-417)-4-3660	-
Fujian Fujitsu Communications Software Ltd.	Wuliting Fuma Road, Fuzhou, Fujian, People's Republic of China	(86-591)-556280	85-92147
Fujitsu America, Inc.	3055 Orchard Drive, San Jose, CA 95134-2017, USA	(1-408)-432-1300	230-176207
Fujitsu Australia Ltd.	475 Victoria Ave., Chatswood, NSW 2067, Australia	(61-2)-410-4555	71-25233
Fujitsu Business Communications of America, Inc.	3190 Mira Loma Ave., Anaheim, CA 92806, USA	(1-714)-630-7721	230-685571
Fujitsu Canada, Inc.	6280 Northwest Drive, Mississauga, Ontario, L4V 1J7 Canada	(1-416)-673-8666	21-6-968132
Fujitsu Component (Malaysia) Sdn. Bhd.	No. 1 Lorong Satu, Kawasan Perindustrian Parit Raja, 86400 Batu Pahat, Johor, Malaysia	(60-7)-481392	84-60577
Fujitsu Component of America, Inc.	3320 Scott Boulevard, Santa Clara, CA 95054-3197, USA	(1-408)-562-1000	25-910-338-0190
Fujitsu Customer Service of America, Inc.	12670 High Bluff Drive, San Diego, CA 92130-2013, USA	(1-619)-481-4004	25-910-337-1127
Fujitsu Deutschland GmbH	Rosenheimer Strasse 145, D-8000, München 80, F.R. Germany	(49-89)-413010	41-17-897106
Fujitsu do Brasil	Rua Manoel da Nóbrega, 1280, 2 ^a Andar, C.E.P. 04001, São Paulo, SP, Brazil	(55-11)-885-7099	38-1121777
Fujitsu Comunicação Eletrônica Máquinas e Serviços Ltda.			
Fujitsu Electronic (Singapore) Pte. Ltd.	7500A Beach Road, #05-301/2 The Plaza, Singapore 0719, Singapore	(65)-296-1818	-
Fujitsu España, S.A.	Edificio Torre Europa 5a, Paseo de la Castellana, 95, 28046 Madrid, Spain	(34-1)-581-8000	52-23887
Fujitsu Europe Ltd.	2, Longwalk Road, Stockley Park, Uxbridge, Middlesex, UB11 1AB, England	(44-1)-573-4444	51-263871
Fujitsu Finance (U.K.) PLC	2, Longwalk Road, Stockley Park, Uxbridge, Middlesex, UB11 1AB, England	(44-1)-573-4444	51-263871
Fujitsu GTE Business Systems, Inc.	2411 West 14th Street, Tempe, AZ 85281, USA	(1-602)-921-5900	-
Fujitsu Hong Kong Ltd.	Room 2521, Sun Hung Kai Centre, 30 Harbour Road, Hong Kong	(852-5)-742917	802-62667
Fujitsu Imaging Systems of America, Inc.	Corporate Drive, Commerce Park, Danbury, CT 06810, USA	(1-203)-796-5400	-
Fujitsu International Finance (Netherlands) B.V.	Officia 1, De Boelelaan 7, 1083 HJ Amsterdam, The Netherlands	-	-
Fujitsu Italia S.p.A.	Via Melchiorre, Gioia No. 8, 20124 Milano, Italy	(39-2)-657-2741	43-350142
Fujitsu Korea Ltd.	9th Floor, Korean Reinsurance Bldg., 80, Susong-Dong, Chongro-Gu, Seoul Special City, Republic of Korea	(82-2)-739-3281	801-24553
Fujitsu Microelectronics Asia Pte. Ltd.	No. 2 Second Chin Bee Road, Jurong Town, Singapore 2261, Singapore	(65)-265-6511	87-22194
Fujitsu Microelectronics Inc.	3545 North First Street, San Jose, CA 95134-1804, USA	(1-408)-922-9000	25-910-671-4915
Fujitsu Microelectronics Ireland Ltd.	Unit D Greenhills Centre, Greenhills Rd., Tallaght, Dublin 24, Ireland	(353-1)-520-744	500-30152
Fujitsu Microelectronics Italia S.r.l.	Centro Direzionale, Milanofiori, Palazzo A2, 1-20090 Assago-Milano, Italy	(39-2)-824-6170	-
Fujitsu Microelectronics Ltd.	Vaughan St., West Gorton, Manchester M12 5DU, England	(44-61)-230-6262	51-667403
Fujitsu Microelectronics (Malaysia) Sdn. Bhd.	8th Floor, MUI Plaza, Jalan P. Ramlee, 50250, Kuala Lumpur, Malaysia	(60-3)-248-8402	-
Fujitsu Microelectronics Pacific Asia Ltd.	8th Floor, Tsim Sha Tsui Centre, 66 Mody Road, Kowloon, Hong Kong	(852-3)-7320100	802-31959
Fujitsu Microsystems of America, Inc.	3025 Orchard Parkway, San Jose, CA 95134-2017, USA	(1-408)-434-1160	230-176207
Fujitsu Mikroelektronik GmbH	Lyoner Strasse 44-48, Arabella Centre 9, OG./A, D-6000 Frankfurt Niederrad 71, F.R. Germany	(49-69)-66320	41-411963
Fujitsu Network Switching of America, Inc.	4403 Bland Road, Somerest Park, Raleigh, N C 27609, USA	(1-919)-790-2211	-
Fujitsu New Zealand Ltd.	6th Floor, National Insurance House, 119-123 Featherston Street, Wellington, New Zealand	(64-4) 733-420	74-30133
Fujitsu Nordic AB	Torggatan 8, S-171 54 Solna, Sweden	(46-8)-764-7690	54-13411
Fujitsu Philippines, Inc.	2nd Floor, United Life Bldg., Pasay Road, Legaspi Village, Makati, Metro Manila, Philippines	(63-2)-85-4951	75-22288
Fujitsu (Singapore) Pte. Ltd.	200, Cantonment Road, #11-01 South Point, Singapore 0208, Singapore	(65)-2240159	87-20138
Fujitsu Systems of America, Inc.	12670 High Bluff Drive, San Diego, CA 92130-2013, USA	(1-619)-481-4004	25-910-337-1127
Fujitsu Vitória Computadores e Serviços Ltda.	Avenida Nossa, Senhora da Penha, 570, 8 ^o Andar, Praia do Canto-Vitória-Espirito Santo, Brazil	(55-27)-225-0355	38-272218
Intellistor, Inc.	2120 Miller Drive, Longmont, CO 80501, USA	(1-303)-678-0697	-
Tatung-Fujitsu Co., Ltd.	5 Floor Tatung Bldg., 225, Nanking East Road 3rd Section, Taipei, Taiwan	(886-2)-713-5396	785-26209

(The information here as of July 31, 1988)

